TÉCNICO LISBOA

An improved aerothermal database for hypervelocity air flows up to 25 km/s

Gabriela Almeida Gomes

Thesis to obtain the Master of Science Degree in

Aerospace Engineering

Supervisor: Prof. Mário António Prazeres Lino da Silva

Examination Committee

Chairperson: Prof. Fernando José Parracho Lau
Supervisor: Prof. Mário António Prazeres Lino da Silva
Member of the Committee: Prof. José Manuel Da Silva Chaves Ribeiro Pereira

July 2022

Declaration

I declare that this document is an original work of my own authorship and that it fulfills all the requirements of the Code of Conduct and Good Practices of the Universidade de Lisboa.

Agradecimentos

Antes de mais, quero agradecer ao meu supervisor, professor Mário Lino da Silva, pelo apoio dado ao longo destes meses, por todas as dúvidas esclarecidas e tempo dedicado, e por me ter ensinado "cenas quânticas". Estendo a minha gratidão ao Bruno Lopez, ao Duarte Gonçalves e ao João Vargas pela ajuda prestada.

Aos meus colegas e amigos de Aeroespacial, muito obrigada por todas as memórias incríveis que levo destes nossos anos, somos realmente uma equipa! À Alice, ao Diogo e à Maria, obrigada por terem ouvido as minhas crises existenciais. Ao Luís, obrigada por todas as noites de trabalho e conversa e por todo o apoio, não teria conseguido sem ti. À Mariana Tavares, obrigada por seres a melhor pessoa que conheço, nunca mais te livras de mim.

Pensar nestes anos de faculdade é sinónimo de pensar no B1. Não sei como é que seria a minha vida sem ter vindo parar ao melhor piso da residência, mas definitivamente não seria tão divertida. A todos os amigos que fiz no B1, obrigada pelas centenas de noites aleatórias, por me ouvirem e aturarem, por rirmos juntos como se ainda fôssemos crianças. Vocês fizeram deste piso o melhor lar que poderia ter imaginado. Um obrigada especial ao Bernardo, o meu inimigo que me apoia e ajuda sempre; à Mariana Brejo, por cuidar tão bem de nós e por saber sempre quando preciso de abraços; ao Magalhães, pelas loucas aventuras; ao Leite, por me fazer rir e por todo o companheirismo. Ao Augusto, nunca conseguirei agradecer o suficiente por tudo ao longo destes anos, mas que venham muitos mais.

Finalmente, nada disto seria possível sem a minha caótica família. A todos vocês, muito obrigada, sou tão sortuda por vos ter. Aos meus pais e ao meu irmão, obrigada por acreditarem sempre em mim e por me apoiarem em tudo o que faço. Amo-vos.

Aos leitores desta tese, muito obrigada pelo interesse, espero que gostem!

Resumo

Em escoamentos com velocidades acima de 10 km/s, ondas de choque convertem a energia coerente do escoamento em energia térmica de agitação interna. A maior parte desta energia é depois transferida para os modos internos das espécies ou consumida em processos endotérmicos. Simular altas velocidades contribui para a compreensão de escoamentos hipersónicos a altas temperaturas e para que estas possam ser consideradas em missões espaciais. Este trabalho pretende simular velocidades extremas usando o SPARK CFD, incluindo para isso melhorias necessárias à sua base de dados aerotermodinâmica. Para uma pressão de arrasto de 0.1 MPa, simulações não ultrapassavam velocidades de 14 km/s, já que as propriedades termodinâmicas usadas tinham sido ajustadas só até 20 000 K. Assim, a sua atualização foi necessária, estendendo até 100 000 K. Dados espetroscópicos para espécies atómicas e moleculares foram compilados e usados para reconstruir curvas de potencial e determinar os níveis rovibracionais correspondentes. Funções de partição foram calculadas, sendo as propriedades termodinâmicas obtidas comparadas à literatura, validando a implementação. Avaliou-se o impacto de adicionar dupla e tripla ionização de átomos. Para velocidades superiores a 18 km/s, a ionização simples está saturada e dupla é necessária, sendo um importante termo de perda energética e diminuindo as temperaturas na camada de choque. Simularam-se velocidades até 25 km/s, em que a tripla ionização ainda não impacta significativamente o escoamento, já que a dupla ainda não está saturada. Mesmo assim, a sua inclusão é recomendada, aumentando a fidelidade das simulações e podendo ser necessária para velocidades mais elevadas.

Palavras-chave: Hipersónico, Aerotermodinâmica, Cinética, Propriedades do Ar, Meteoróides

Abstract

For hypervelocity flows above 10 km/s, the strong bow-shock wave converts the flow coherent energy into thermal agitation energy. Most of this energy is then transferred into the gas species internal modes or consumed through endothermic processes. Simulating higher velocities contributes to the understanding of hypersonic high-temperature flows and paves the way for these velocities to be considered for Space missions. This work aims to simulate extreme velocities using the SPARK CFD code, by including the necessary enhancements to its aerothermal database. For a ram pressure of 0.1 MPa, the simulations were typically limited to velocities lower than 14 km/s, as the thermodynamic properties used were fitted only up to 20 000 K. Accordingly, these have been updated, extending their validity to 100 000 K. Atomic and molecular species internal levels spectroscopic data was compiled, with reconstruction of molecular potential curves and determination of the corresponding rovibronic levels. Partition functions were calculated and the determined thermodynamic properties were compared to other databases, validating the implementation. The impact of adding double and triple ionization for atoms was evaluated. For velocities higher than 18 km/s, single ionization is capped and double is required, as it becomes an important energy loss term, significantly decreasing the temperatures at the shock layer. Velocities up to 25 km/s were simulated, with triple ionization found to not impact the flowfield significantly, as double ionization is not yet capped. Nevertheless, its inclusion is recommended, as it increases the simulations' fidelity and might become necessary for higher velocities.

Keywords: Hypersonic, Aerothermodynamics, Kinetics, Air Properties, Meteoroids

Contents

List of Tables

List of Figures

Chapter 1

Introduction

1.1 Motivation

Human curiosity has always lingered on the concept of limit: in what would happen at 0 K temperature, in what occurred in the beginnings of time and what might occur in the end or on the physics of black holes. Pushing boundaries is in our nature and the very idea of boundaries interests us. While picturing a body entering Earth's atmosphere, as fast as possible, many questions arise: What happens to it? To the flow around it? Are any of its properties limited by a maximum? Can human spacecrafts ever reach those velocities? One can wish upon a star to know the answers of these questions; or try to answer them with shooting stars - with meteors.

Hypersonic high-temperature flows entail a variety of phenomena that need to be carefully studied and modeled - with reasonable computational costs -, encapsulating many areas of knowledge that interact with one another. Typical studies in this field are applied to spacecraft re-entry velocities; besides the usual phenomena studied in those cases, additional processes have to be considered when studying even higher velocity flows.

The fastest bodies that enter the Earth's atmosphere are meteoroids: fragments of larger space bodies such as asteroids and comets, with diameters ranging from millimeters to several meters. When these space rocks enter a planet's atmosphere at high speeds, they burn up, being called a meteor, or, more commonly, a shooting star. When meteoroids survive the trip through the atmosphere and reach the planet's ground, they are in turn referred as meteorites.

Meteoroids enter the Earth's atmosphere with velocities that in theory may vary from 11 to 72 km/s [1]. The lower limit is defined by the Earth's escape velocity, as a body travelling with a velocity lower than 11km/s, at an altitude of 100 km, will orbit around the Earth. As for the upper limit, this is determined by the Solar System's escape velocity: at 1 au, objects with a velocity higher than 42 km/s relative to the Sun will exit the Solar System; the Earth's velocity around the Sun is of 30 km/s, therefore a meteoroid on a head-on collision trajectory with the Earth will have a maximum relative velocity of 72 km/s. The mean velocity values of the observed meteoroids are between 25 and 30 km/s, from radar observations, and 20.6 km/s for Near-Earth Objects (NEO), an estimation from modeling [2].

Typical Earth re-entry velocities of spacecrafts range from 8 km/s (orbital speed) to 14 km/s for Mars return missions, which explains how hypersonic flows with these velocities are the subject of more studies, with the understanding of the associated phenomena being essential for the planning of Space missions. Nevertheless, future missions to Mars or to nearby asteroids will require re-entry velocities between 13 and 16 km/s [3] and missions to outer planets and their respective moons may even require velocities above 16 km/s, therefore broadening the knowledge of hypersonic high-temperature flows to higher velocities is also useful from a mission planning standpoint.

1.2 Atmospheric Entry Hypersonic Flows

Hypersonic flows are generally characterized by the presence of compressibility effects leading to the formation of strong and high temperature shock waves. Tipically, freestream flows with a Mach number higher than 5 are said to be in the hypersonic regime; however for the velocities here considered, the flow is chemically reacting and the definition of Mach number loses some significance and it is more common to think in terms of velocities [4].

The dynamics associated with this flight regime are very different from those considered in subsonic or even supersonic flows. Picturing a spherical meteoroid in the hypersonic regime, it creates a detached bow shock wave. In the shock layer the flow is quickly decelerated until the stagnation point through the transfer of kinetic to thermal energy. As a result, extreme temperatures are reached - in the $10^4 - 10^5$ K range - and the so-called high-temperatures effects become important and have to be considered in the equations describing the flow. These physical-chemical phenomena include dissociation and ionization (simple, double, ...) of chemical species - forming a plasma -, non-equilibrium thermochemistry[1] and radiative absorption and/or emission, as a result of excitation and de-excitation of the species internal degrees of freedom.

Tackling this from a microscopic perspective, the very high temperatures excite the internal energy modes of the gas' particles, which act as reservoirs to store thermal energy. This excitation is a result of collisions between particles, relaxing the translational energy mode (whose measurement gives the conventional temperature) and exciting the internal energy modes. If the inter-nuclear bonds in a molecule are overcome by this storage of vibrational energy, then the molecule dissociates into atomic species. Similarly, through sufficiently energetic particle collisions, a bound electron may get away from the respective nucleus's attraction and ionization occurs. These reactions are endothermic, meaning they absorb heat from its zone environment.

The flow characteristic time in these regimes is typically comparable to the characteristic times of the chemical reaction and the collisions processes. This means that the time for the flow to adapt to the extremely different post-shock conditions may be greater than the time a particle spends in a specific region of space, therefore relaxation occurs as the particles move through the flow. This leads to a chemically reacting flow and to the internal energy states being populated according to non-Boltzmann distributions, and the flow is considered to be in thermal and chemical non-equilibrium, adding more

[1] owing to the high temperatures and the rarefied freestream flow

non-equilibrium conditions to be modeled.

Laminar flow is typically assumed in the forebody region, due to the small Reynolds number in the stagnation region and to the strong favorable pressure conditions that will delay the transition to turbulent flow. For the altitudes of interest of this work (45 km to 65 km), the atmospheric density conditions are those of continuous flow so it may be modeled by finite volume methods and the Navier-Stokes equations.

In conclusion, the simulation of an atmospheric entry with computational fluid dynamics should consider all the phenomena described above. Although the interdependence between them is strong, the extremely high computational costs of simulations will compel the assumption of some decoupling between areas of study and even the neglecting of some effects, such as thermal non-equilibrium, in some cases.

1.2.1 Meteoroids

While the principles studied in the following chapters and the reached conclusions are mostly theoretical, these may be applied to various cases of hypersonic high-temperature flows. The example of meteoroids entering Earth's atmosphere will accompany us for the entirety of the thesis. The application to the meteoroids case is timely due to many reasons, such as:

- they represent, nowadays, the objects that enter our atmosphere at higher velocities, allowing for future comparisons with experimental data and use of information previously collected in the ranges of variables addressed by this work;
- each meteoroid has its unique properties and shape and that will impact the flowfield around them, however, since they tumble during their flight through the atmosphere, one generally adopts the simple shape of the sphere, as done in the literature [2]. This simplifies grid adaptation and flowfield convergence stability [5];
- the spherical shape assumed for the meteoroid creates a detached bow shock, similar to what happens with blunt-body spacecrafts, that are shaped like this to keep a stand-off distance to the shock and allowing for temperature decrease up to its wall - if it weren't for this effect and the heat shielding materials, the spacecraft would not survive the high temperatures reached in the decelaration process. As a result of the similar detached shocks created by the spherical meteoroids here considered, some conclusions will also be applicable to future superorbital entry spacecrafts;
- Earth's atmosphere has up to date data, with higher degree of accuracy than other planets; on the other hand, the application to our planet's example in the elaboration of databases, thermodynamic models and kinetic models is particularly relevant;
- the modelling of flow around objects entering our atmosphere at higher velocities is essential for risk assessment of meteoroid's events and for planetary defense, as these may cause material damage and threat lives.

1.3 State of the Art

Meteoroid science is a highly complex and polyvalent field, entailing problems from various areas of knowledge. Although some of its sub-disciplines are already well comprehended by scientists, with the oldest meteor phenomena study being traced to more than two centuries ago and overall interest in these strange bodies going back many centuries before [6], shock waves in meteoroids are still a largely unknown phenomenon, with many questions remaining unanswered.

The work of Silber et al. [2] resumes the main accomplishments in the area of meteor generated shock waves so far, balancing them with a review of the related hypersonic gas dynamics topics, as well as the questions scientists are still focusing on.

Aerothermodynamic modelling of the flow around a body is essential to this work. Depending on the flow regime encountered - described by the Knudsen number - different modelling methods must be employed. For bodies in the transitional and free molecular regimes, it is necessary to implement the Boltzmann equation of kinetic energy; Direct Simulation Monte Carlo (DSMC) [7] is the most commonly used method (although still very computationally expensive), answering the need for particle-simulation methods to deal with the fact that linear transport terms for mass, viscosity, diffusion, and thermal conductivity in the Navier-Stokes are no longer valid. Works such as [8, 9] apply this method to meteoroids of 1mm - 1cm diameter in altitudes of 90 km or higher and a large range of velocities. Our work does not deal with rarefied regime or such small meteoroids, operating in the continuum regime.

Fragmentation and ablation are two important phenomena that have had many studies performed on them, as they impact meteoroid's trajectory and behaviour, fluid composition and the consequences on Earth. Body fragmentation - a process that happens repeatedly during the flight - and the fragments' interactions with each other's shock waves are necessary to take into account for a thorough analysis of a meteoroid's event, and increases complexity of an already complicated theme. The different methods usually considered to model fragmentation are presented in works like [2, 10, 11]. Ablation is the process by which the meteoroid, at lower altitudes, experiences mass loss by interaction with the atmosphere, when it encounters increased atmospheric densities and experiences rapid heating. Since ablation only happens at high enough temperatures and micrometeoroids usually have rapid heat loss by thermal radiation, this process is more important in larger meteoroids - with larger ones penetrating deeper in the atmosphere, while smaller ones deposit their material at 80 km to 120 km. Meteoroid ablation is pointed as a source of organic material in the atmosphere. Popova [12] studied ablation and the models to simulate it. This thesis will focus on the theory and simulation of hypersonic high-temperature flow around a single non-ablating body, so fragmentation and ablation will not be covered but are important to keep in mind for future applications to real meteoroid's events, in which these processes will be of great importance.

As previously stated, entry shock wave studies are more prevalent in the area of reentry vehicles, where simulations and experiments have been made throughout the years for the planning of space missions. The considered velocities are significantly lower than those that meteoroids may reach, with little cross disciplinary work having been made among meteoroid and shock wave investigators, mainly

for velocities higher than 15km/s.

However, the work of Johnston and Brandis [3], in 2015, is a relevant exception: this work, applied to reentry vehicles, pushes the aerothermodynamic modelling capabilities forward, allowing for simulation of velocities of 16 km/s and up to 22 km/s, while remaining in the continuum regime and using Navier-Stokes equations, unlocking the possibility of higher Earth entry velocities in future missions. This work focuses on enhancements required to treat temperatures higher than 20 000K, resultant from velocities greater than 16 km/s, such as thermodynamic properties suited to higher temperatures for atomic species, ionization potential lowering, addition of N^{++} and O^{++} and non-Boltzmann radiation modelling of N^{+}. The enhancements are applied to the LAURA/HARA coupled flowfield and radiation solver and a tabulated heating model is created. The influence of coupled radiation and ablation in the simulations is also studied and the performed enhancements remove assumptions regarding their impact and allow for less uncertainty in trajectories with these range of velocities. This work will often be used to draw comparisons to the work developed on this thesis, regarding some of the employed enhancements.

As for the determination of thermodynamic properties, level energies have to be determined and for diatomic molecules that may be done through the reconstruction of potential curves. Examples of works that make use of such methods are [13–16].

Following [3], two other works by Johnston applied these developments to meteoroids. Johnston et al. [17], in 2018, used chemically reacting computational fluid dynamics, coupled with radiation transport and surface ablation, allowing the assessment of the heat transfer coefficient, commonly assumed as 0.1. The effects of coupled radiation and ablation in the reduction of radiative heating are studied for altitudes below 50 km - an important range for potentially hazardous events. They conclude that for a meteoroid with a velocity of 20 km/s, coupled radiation reduces the stagnation point radiative heating by over 60% and coupled ablation (with coupled radiation) reduces radiative heating by at least 70%. To simulate this, 26 additional species were accounted for and the large reduction seen in radiative heating is partially due to the low ionization energies of the ablation products in comparison to air species. Regarding the impact of coupled radiation, in comparison to uncoupled, it is shown to decrease the shock layer temperatures, resulting in a decreased shock standoff distance (as a result of a necessary increase in density to accommodate decreased temperatures while pressure remains constant) and decreased radiative flux. This is the result of energy radiating out of the shock layer, which leads to a decrease of the total enthalpy within the shock layer.

Fernandes [18] and Coelho [19] developed works that study radiation in hypersonic high-temperature flows, using the SPARK Line-by-Line code [20] - radiative solver that computes the spectrally-dependent emission and absorption coefficients of a gas mixture in non-equilibrium and relies on results from the SPARK CFD solver. Loosely-coupled radiation simulation is yet to be implemented in the SPARK CFD code, as well as coupled radiation that would lead to more physically accurate simulation results and is something to strive for in the future of SPARK simulations. This work will not cover the effects of radiation in the shock layer.

Finally, Johnston and Stern [5], in 2019, developed a model for simulating the radiative flux reaching the ground originating from a meteor shock-layer and wake, applying the methods developed in [3, 17]

and using the Tunguska event as a test case - the largest meteor airburst event on Earth's recorded history, that occurred in Russia on June 30, 1908. Potential Tunguska trajectories were used to simulate ground heating footprints and compare them with the measured radiant burn area to assess entry parameters such as optimal initial radii, which was estimated here to be between 30 and 45 m.

1.4 Objectives

Considering only the aerodynamic behaviour of the shock wave, as the speed of a body entering a planet's atmosphere increases, so does the post-shock temperature; however, as already stated, further increases in velocity will activate increasingly important energy loss terms such as the endothermic chemistry reactions and radiation losses.

For example, at low temperatures, second ionization will have an impact that can be easily neglected, happening at negligible rates. For higher temperatures, this endothermic process will have an impact in temperature, acting as a considerable energy loss term, and its consideration in simulations will cause the temperature to decrease, hence increasing simulation fidelity; the exclusion of double ions in this second case would lead to unrealistically higher temperatures.

A question then arises: will there be, in practice, a ceiling of temperature reached in the shock layer? If one considers the additional processes that higher and higher velocities entail, will there be a certain temperature that is never exceeded in the shock layer, with any extra energy from increasing entry velocities being dissipated through chemical reactions and radiation from the entry plasmas?

The purpose of this work is to simulate entry velocities previously not reached with the SPARK CFD code, with the necessary additional processes modeled and implemented. For resulting temperatures lower than 20 000 K, the processes to be considered have already been studied. However, extending simulations to higher temperatures will require the inclusion of further phenomena to get closer to reality.

This work aims to tackle a very polyvalent area, as full description of these flows entails topics such as fluid dynamics, thermodynamics, chemistry, quantum mechanics, statistical physics, electromagnetism, radiation and ablation, to name a few. Here, the focus will be in some of the processes that require updates to enforce accurate modeling of velocities higher than 14 km/s and study their influence in simulations. The consequences of simulating flow conditions without including the necessary enhancements will also be studied, as it is expected that this will lead to incorrect higher temperatures and behaviours that do not represent physical reality.

More specifically, to simulate entry at the Earth's atmosphere at high velocities, the following enhancements will be made: thermodynamic properties curve fits for all the species will be extended beyond 20 000 K, and up until 100 000 K, creating an updated thermodynamic database. This will be done through an accurate reconstruction of all the possible internal quantum levels of the species; double and triple ionized species, N^{++}, O^{++}, N^{+++}, O^{+++}, will also be included in the simulations.

Along the way, we will also compile a detailed and updated spectroscopic database for N_2, N_2^+, O_2, O_2^+, NO, NO^+, creating a helpful source of information for several applications; the potential curves for those molecules will also be plotted, with remarks on the physical phenomena behind their perturbations.

Considering these implemented enhancements, we will simulate conditions of velocities, temperatures and ionization degrees never previously reached for Earth's atmospheric entries using the SPARK code and analyse the effect these new databases and models have on the hypersonic flow, namely in the stagnation line's temperature and chemical species mole fractions.

We will model hypersonic high-temperature flows for a gas mixture of 15 species (N_2, O_2, NO, N_2^+, O_2^+, NO^+, N, O, N^+, O^+, N^{++}, O^{++}, N^{+++}, O^{+++}, e^-), in the continuum regime, around spherical meteoroids with 0.3 m radius, subject to ram pressures of 0.1 MPa, for velocities in the 8 - 25 km/s range, furthering the knowledge of the behaviour for velocities higher than those previously studied, paving the way for these to be considered for future missions and for a better understanding of meteoroids conditions in Earth's atmosphere.

Simulating extreme conditions accurately also has advantages beyond the understanding of meteoroid science and the sating of scientific curiosity. The confirmation of the hypothesis of a temperature ceiling may be helpful for the design of spacecrafts, knowing there is a maximum temperature that any spacecraft entering Earth would have to be shielded from. Otherwise, for increasingly high velocities there would be the need for thermal protective shields that would endure increasingly high temperatures.

In conclusion, although this work does not answer the question of the existence of a temperature ceiling, it is our hope that it gets us one step closer to answering the question of what happens in these limiting regimes.

1.5 Thesis Outline

This document is divided in five main chapters.

Chapter 2 explores the physical models and mathematical formulations behind hypersonic flows. Besides the classical thermodynamic, kinetic and transport properties calculations presented, a special emphasis is given to the process of calculating thermodynamic properties from quantum energy levels.

Chapter 3 discusses the numerical implementation of the models necessary for the simulations. Special focus is given to the enhancements which were brought, such as the addition of species and the update of thermodynamic properties, a process that also entails the compilation of diatomic molecules' spectroscopic data, the reconstruction of potential curves and the determination of quantum energy levels. The obtained results' verification and comparisons with other data are also discussed in this chapter. Simulation strategies adopted are explored as well.

In Chapter 4 the simulation's results are presented and compared, and the obtained improvements reported.

Chapter 5 summarizes the main achievements and conclusions of this thesis. It also presents reflections on important future work.

Chapter 2

Governing Equations

Fluid Dynamics of Hypersonic Flows

This chapter presents the theoretical background for understanding fluid dynamics of multi-species hypersonic reactive flows at high temperatures.

The governing equations for the computation of such flows, neglecting intermolecular forces (assuming perfect gas) and assuming a continuum medium, are the Navier-Stokes equations and are presented in section 2.1.

The solution of the Navier-Stokes equations requires the modeling of several thermodynamic properties of the gas mixture. The determination of these properties is one of the main focuses of this work and is introduced in 2.2. Thermal non-equilibrium is also briefly referred, for cases when microscopic collision times are larger than the characteristic flow time. Statistical thermodynamics allows for the understanding of how the determination of energy levels leads to the calculation of thermodynamic properties, something studied on section 2.3. Additionally, different models for computing energy levels are discussed, namely potential curve reconstruction methods.

Furthermore, chemical non-equilibrium is discussed in 2.4. This is a result of the high temperatures achieved in such high velocity flows, with the energy involved in particle collisions being sufficient to break chemical bonds and induce chemical reactions. In section 2.5 the transport properties that need to be computed for the Navier-Stokes' equations are presented as well as the models used for their approximated calculation.

2.1 Conservation Equations

The governing equations for hypersonic flows are the compressible Navier-Stokes equations [4], that describe the conservation of quantities of the flow, assuming a continuum flow regime ($Kn < 0.01$). Classically the conserved quantities are the mass, momentum and energy for a mixture where thermochemical equilibrium is assumed. But for the planetary entry conditions here considered one may need to include chemical and thermal non-equilibrium effects to the equations. For chemical non-equilibrium,

this is done by considering one mass conservation equation for each chemical species. For thermal non-equilibrium, on the other hand, each independent thermal mode's energy must be conserved, so an additional energy conservation equation for each non-equilibrium thermal mode must be included and solved.

The governing equations for hypersonic radiating shock layers are as follows:

- Mass of species s:

$$\frac{\partial(\rho c_s)}{\partial t} + \boldsymbol{\nabla} \cdot (\rho c_s \boldsymbol{V}) = \boldsymbol{\nabla} \cdot \boldsymbol{J_s} + \dot{w}_s \tag{2.1}$$

- Momentum :

$$\frac{\partial(\rho \boldsymbol{V})}{\partial t} + \boldsymbol{\nabla} \cdot (\rho \boldsymbol{V} \otimes \boldsymbol{V}) = \boldsymbol{\nabla} \cdot [\boldsymbol{\tau}] - \boldsymbol{\nabla} p \tag{2.2}$$

- Total energy :

$$\frac{\partial(\rho e)}{\partial t} + \boldsymbol{\nabla} \cdot (\rho \boldsymbol{V} e) = \boldsymbol{\nabla} \cdot (\boldsymbol{V} \cdot [\boldsymbol{\tau}]) - \boldsymbol{\nabla} \cdot (p \boldsymbol{V}) - \boldsymbol{\nabla} \cdot \boldsymbol{q} \tag{2.3}$$

- Thermal non-equilibrium energy k:

$$\frac{\partial(\rho e_k)}{\partial t} + \boldsymbol{\nabla} \cdot (\rho \boldsymbol{V} h_k) = \boldsymbol{\nabla} \cdot \left(-\kappa_k \boldsymbol{\nabla} T_k + \sum_s \boldsymbol{J_s} h_{s,k} \right) + \dot{\Omega}_k \tag{2.4}$$

The heat flux vector $\boldsymbol{q}$ is the sum of convective heat, diffusive heat and, in cases where radiation is considered, radiative heat:

$$\begin{aligned} \boldsymbol{q} &= \boldsymbol{q}_D + \boldsymbol{q}_C + \boldsymbol{q}_R \\ &= \sum_s \boldsymbol{J_s} h_s - \sum_k \kappa_k \boldsymbol{\nabla} T_k + \boldsymbol{q}_R \end{aligned} \tag{2.5}$$

In equations 2.1 - 2.5, ρ is the density, c_s is the species mass fraction, $\boldsymbol{V}$ is the flow velocity vector, $\boldsymbol{J_s}$ is the mass diffusion flux vector and $\dot{w}_s$ is the source term for production/destruction of species s; $[\boldsymbol{\tau}]$ is the viscous stress tensor, p is pressure, e is the specific internal energy of the mixture; e_k and $\dot{\Omega}_k$ stand for the internal energy and the energy exchange source term associated with the thermal energy k; k_k and T_k stand for thermal conductivity and temperature associated with each thermal energy mode k, h_s is the species enthalpy and $\boldsymbol{q}_R$ is the radiative heat flux vector, while $\boldsymbol{q}_D$ and $\boldsymbol{q}_C$ represent the diffusive and convective heat flux vectors, respectively.

2.2 Thermodynamic Properties

The determination of thermodynamic properties, such as entropy, enthalpy and internal energy, is key for the solving of the Navier-Stokes equations at high temperatures. In other words, to understand the thermodynamic tendencies of a high-temperature non-equilibrium reactive gas, a model that considers the species' internal structure is required - a quantum perspective of the problem is in order.

To do so, statistical thermodynamics is used - this theory views a gas as a collection of particles where each carries energy while moving through the flow. This energy is separated into the following energy modes: translational, rotational, vibrational and electronic - the latter three also being called internal modes. These energy modes for a given particle's energy level are represented in figure 2.1. The species type determines the available modes: monoatomic particles only have translational and electronic energy; free electrons only have translational energy; molecules may have all energy modes.

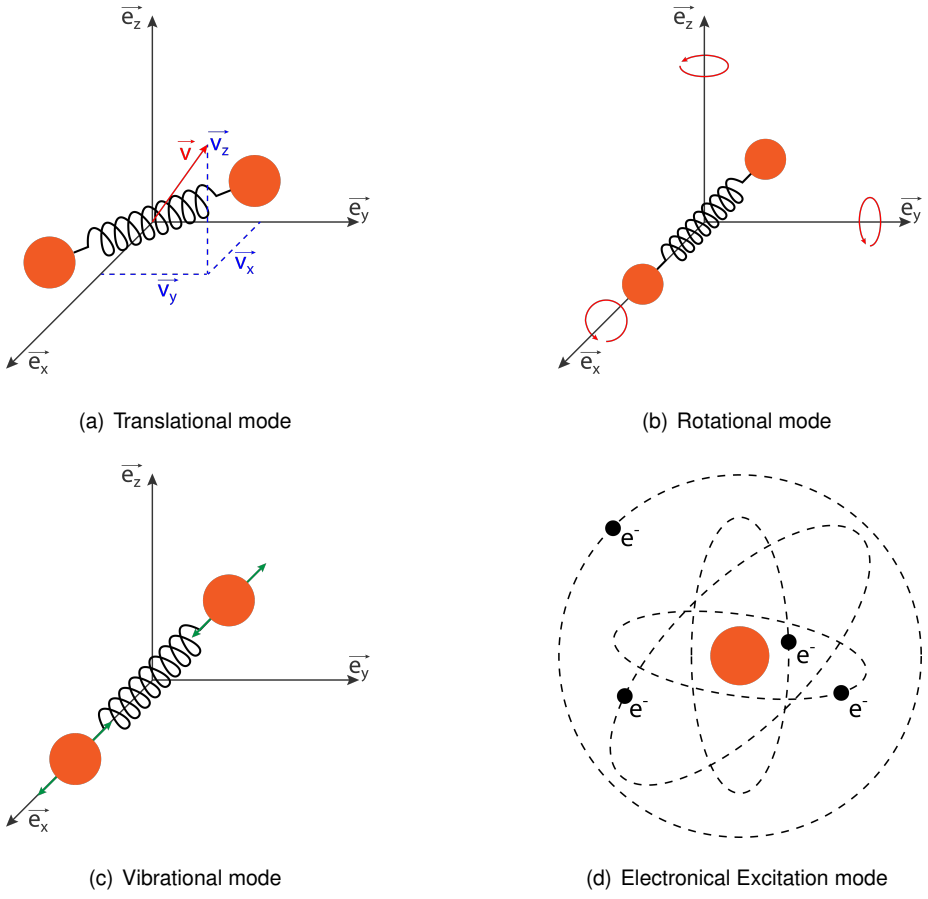

(a) Translational mode

(b) Rotational mode

(c) Vibrational mode

(d) Electronical Excitation mode

Figure 2.1: Different energy modes (diatomic molecules case).

The energy mode's degrees of freedom also depend on the kind of particle. Naturally, since a particle's center of mass moves through space, the translational kinetic energy depends on velocity, having three degrees of freedom. Energy stored as rotational energy depends on the species' moments of inertia about the corresponding axis - that being said, while polyatomic molecules may have three or more degrees of freedom, diatomic molecules will only have two, since the moment of inertia about the axis that connects its nuclei can be neglected. Vibrational energy degrees of freedom also depend on

the type of molecule, with diatomic molecules adding one degree of freedom to the system.

By the Born-Oppenheimer approximation [21] - an important concept in the formal description of molecular quantum mechanics that allows the separation of different energy modes under simple circumstances - the total energy of a particle may be approximated as:

$$\varepsilon_{tot} = \varepsilon_{tr} + \varepsilon_{rot} + \varepsilon_{vib} + \varepsilon_{exc} + \varepsilon_0 \tag{2.6}$$

with ε_k being the energy of each thermal mode and ε_0 being the zero-point energy of the species.

For a mixture of different chemical species, each species' energy level is populated with a certain number of particles, according to a given distribution. The Boltzmann distribution N_j^* is the population distribution across all energy levels associated with an equilibrium mixture that maximizes the entropy of the system. We note that different microscopic arrangements may result in the same energy level, being called degenerate states - the number of states that coexist within a given energy level is called the degeneracy of that level.

To obtain the total internal energy of a single-species equilibrium system, from a macroscopic perspective, one needs to add the contribution of all energy levels over the population distribution:

$$E = \sum_j \varepsilon_j N_j^*(\varepsilon_j) \tag{2.7}$$

Each of these energy modes is quantized, and the theory of statistical thermodynamics provides an explicit way to determine each energy mode ε_k. However, the population distribution N_j^* depends on the energy levels ε_j, therefore equation 2.7 is not easy to evaluate.

Either way, and since the contribution of different energy modes can be separated, the total internal energy of a single species per unit of mass (total specific internal energy) may be calculated with:

$$e_{tot,s} = e_{tr,s} + e_{rot,s} + e_{vib,s} + e_{exc,s} + e_{0,s} \tag{2.8}$$

The internal energy of a mixture of perfect gases is calculated from the internal energy of each of its species, e_s and the corresponding mass fractions, c_s:

$$e = \sum_s c_s e_s \tag{2.9}$$

Classical thermodynamics have no explicit expression to calculate the contribution of each energy mode e_k of equation 2.8. Therefore statistical thermodynamics and its microscopic description of a gas are needed. Considering a collection of quantum states in equilibrium, the internal energy of a gas may be calculated by:

$$e = RT^2 \left(\frac{\partial \ln Q}{\partial T} \right)_V \tag{2.10}$$

where R is the specific gas constant and Q represents a very important concept in statistical thermodynamics - the partition function:

$$Q = \sum_j g_j e^{\frac{-\varepsilon_j}{k_B T}} \tag{2.11}$$

where T is the temperature of the gas, k_B is the Boltzmann constant , g_j is the number of degenerate states of energy level j and ε_j is the total energy of the system in that level.

The partition function describes the statistical properties of a system in thermodynamic equilibrium [4]. They are of particular importance since most thermodynamic properties of a system can be expressed using the partition function or its derivatives.

Additional information on how the decomposition of modes can be useful for the calculation of partition functions and subsequent calculation of thermodynamic properties can be found in appendix A.1.

Here, the well-known relations between said properties will be recalled, so that the usefulness of obtaining the partition functions is clear: it allows for the calculation of internal energy through equation 2.10 and then that property is used to calculate enthalpy using the relation in 2.12; additionally equations 2.13 define specific heats; finally, entropy relates to C_p through equation 2.14.

$$h = \sum_s c_s h_s \quad \text{, with} \quad h_s = e_s + \frac{p_s}{\rho_s} = e_s + R_s T \tag{2.12}$$

$$C_v = \left(\frac{\partial e}{\partial T} \right)_v \quad \text{and} \quad C_p = \left(\frac{\partial h}{\partial T} \right)_p \tag{2.13}$$

$$C_p = T \left(\frac{\partial s}{\partial T} \right)_p \tag{2.14}$$

To summarize, one needs these thermodynamic properties for the solving of Navier-Stokes equations. The partition function concept allows for their calculation. In turn, to calculate Q one needs the energy of all the levels for each species. This process will be explained in section 2.3

2.2.1 Thermal Non-equilibrium

When the internal energy of each species in a mixture is distributed over its energy levels according to a Boltzmann distribution, the gas is said to be in thermal equilibrium, with all its thermal energy modes

associated to a single temperature $T_k = T$. In these cases, equation 2.4 is not considered.

However, in hypersonic flows, with the large associated gradients, thermal equilibrium may not model the flow accurately. For a reacting flow, the equilibrium state is not achieved instantly, with microscopic collisions and radiative energy exchange processes having to occur in order for the equilibrium to be reached. This takes place over a time τ_e, the characteristic time for energy exchanges. Comparing it to the flow characteristic time τ_f, if $\tau_f << \tau_e$ then the flow region is said to be in non-equilibrium, since the flow crossing the domain has not enough time to perform the required energy exchanges to achieve equilibrium. This is what generally happens in high-temperature hypersonic flows, in the shock layer region.

For these cases, each species may have its own set of internal temperatures $T_{k,s}$ and dealing with this requires that different temperatures for each mode to be considered in a so-called multi-temperature approach.

In this approach, the gas mixture is characterized by multiple temperatures T_k, with each one having a thermal non-equilibrium equation (2.4) associated. For each mode, the thermal energy ε_k and the enthalpy h_k will be a function of T_k, and $\dot{\Omega}_k$ is the source term defining energy exchanges between different modes.

There are many different multi-temperature models, depending on the assumptions made of which energy modes may be in equilibrium for each particle. Some of the most common are presented in table 2.1, as well as the single temperature (1T) model for thermal equilibrium.

Table 2.1: Most common multi-temperature models.

Model	Energy mode (Particle Type)				
	Translational		Rotational	Vibrational	Electronic Excitation
	(e^-)	(heavy)	(molecule)	(molecule)	(heavy)
1T (Equilibrium)	T	T	T	T	T
2T	$T_{vib-exc}$	$T_{tra-rot}$	$T_{tra-rot}$	$T_{vib-exc}$	$T_{vib-exc}$
3T	T_e	$T_{tra-rot}$	$T_{tra-rot}$	$T_{vib-exc}$	$T_{vib-exc}$
	T_e	$T_{tra-rot}$	$T_{tra-rot}$	T_{vib}	T_e

More details about these models may be found in works such as [18]. Their disadvantages are that they do not only require additional computational effort but also more data to describe the relaxation models.

Another approach is to use state-to-state models, that consider each internal energy level as if it was an individual species, allowing for the specification of non-Boltzmann distributions for each thermal energy mode. The application of this method is out of the scope of this work, but more details on it can be seen in [22, 23].

The 1T model will be the one applied throughout this work. For the simulated flight regimes, the post-shock pressure will be high, leading to a fast equilibrium of the different temperatures shortly after the shock. Considering 1T models allows to better pinpoint the effects of our updated chemical and

thermodynamic models. Furthermore, the multi-temperatures models would need to be extended for the high-temperature and strong ionization regimes of this work, which is beyond the scope of this thesis.

2.3 Energy Levels Calculation

The determination of important thermodynamic properties requires the calculation of energy levels. For atomic species, accurate level energy databases are available online [24] and one simply makes use of those energies. For diatomic species, experimental data is used to carry out the reconstruction of potential energy curves. This allows a better accuracy than any *ab initio* quantum method for the determination of the potential. The theory and governing equations behind it are explained in the following sections.

2.3.1 Approach based on Polynomial Expansions

The calculation of level energies in diatomic molecules entails the complexity of additional degrees of freedom from molecular vibration and rotation, instead of only electronic energy considered for atomic species. So, for each electronic state of the molecule, there is a corresponding set of vibrational and rotational levels. The translational energy mode will be ignored for a while since the potential energy is the focus here. A simplification of this very complex problem is arranged by applying the Born-Oppenheimer approximation, considering electronic, vibrational and rotational modes separately. The total internal wave function of the molecule may then be decoupled in three wave functions:

$$\psi = \psi_{el} \times \psi_{vib} \times \psi_{rot} \tag{2.15}$$

The total energy of a specific energy level can be split into these terms (with $E_{el} \gg E_{vib} \gg E_{rot}$):

$$E = E_{el} + E_{vib} + E_{rot} \tag{2.16}$$

These level energies correspond to the solutions of the Schrödinger equation for an anharmonic oscillator and a distorted rotator and are represented by a series of polynomial expansions:

$$\begin{aligned} E_{e,v,J} &= T(e) + G(v) + F_v(J) = \\ &= T(e) + c_e + \omega_e(v+\frac{1}{2}) - \omega_e x_e(v+\frac{1}{2})^2 + \omega_e y_e(v+\frac{1}{2})^3 + \cdots + \\ &+ B_v(J(J+1)) - D_v(J(J+1))^2 + H_v(J(J+1))^3 + \dots \end{aligned} \tag{2.17}$$

So E_{el} can also be written as $T(e)$ or V_{eq}, being the minimum value of the potential $V(r)$, at the equilibrium distance; additionally, one may say that $E_{vib} = G(v)$ and $E_{rot} = F_v(J)$. c_e, ω_e, $\omega_e x_e$, ...

represent the spectroscopic constants.

Neglecting fine structure and considering an electronic state e, the vibrational and rotational energy levels may also be described by a Dunham expansion [25, 26]:

$$E_{v,J} = hc \sum_{i=0,j=0} Y_{ij}(v+\frac{1}{2})^i J^j (J+1)^j \tag{2.18}$$

where v and J are the vibrational and rotational quantum numbers, respectively, h is the Planck constant and c is the velocity of light in vacuum (used here as its convenient to represent the energy in terms of wave numbers). The Dunham coefficients Y_{ij} relate to the traditional spectroscopic constants as follows:

$$\sum_{i=0} Y_{i0}(v+\frac{1}{2})^i \approx G(v) = c_e + \omega_e(v+\frac{1}{2}) - \omega_e x_e(v+\frac{1}{2})^2 + \omega_e y_e(v+\frac{1}{2})^3 + ... \tag{2.19}$$

$$\sum_{i=0} Y_{i1}(v+\frac{1}{2})^i \approx B_v = B_e - \alpha_e(v+\frac{1}{2}) + \gamma_e(v+\frac{1}{2})^2 + ... \tag{2.20}$$

Terms involving higher-order rotational energy terms as D_v and H_v ($j > 1$) are usually considered negligible in the RKR (Rydberg-Klein-Rees) calculations, that will be the method used in this work for obtaining energy levels.

This correspondence can also be represented in a more intuitive way through table 2.2.

Table 2.2: Correspondence between the first Dunham coefficients and traditional spectroscopic constants.

	Y_{ij}	0	1	2	3	4	5	6	7
G(v)	0	c_e	ω_e	$-\omega_e x_e$	$\omega_e y_e$	$\omega_e z_e$	$\omega_e a_e$	$\omega_e b_e$	$\omega_e c_e$
B_v	1	B_e	$-\alpha_e$	γ_e	δ_e[1]	η_e	x	x	x
-D_v	2	-D_e	$-\beta_e$	δ_e	x	x	x	x	x
H_v	3	H_e	αH	x	x	x	x	x	x

Traditionally the Dunham expansion and its extrapolation is widely used for calculating energy levels and is useful in the absence of more detailed methods; it allows for a simple calculation of the number of vibrational levels for a specific electronic state and the respective energy of each vibrational level. Likewise, rotational levels may also be considered with the Dunham expansion.

Although this expansion is an extremely helpful tool, it is necessary to point out that its accuracy is strongly associated with the validity of the Dunham constants (or spectroscopic constants) - obtained by fitting a specific set of measured rovibrational levels with equation 2.18. That being said, and if, as an example, a certain state of a diatomic molecule had its first 10 purely vibrational levels (v from 0

[1] Some authors use the variable δ_e in the polynomial expansion for D_v instead of B_v. This work uses it in the expansion for B_v

to 9; $v_{max}^{valid} = 9$) measured experimentally and fitted with the Dunham expansion, then, rigorously, that expansion may only be accurate at describing these exact boundaries [14]. However, many compilations of spectroscopic data do not specify the range of rotational and vibrational quantum numbers over which the interpolation was done (an issue encountered frequently during the development of the spectroscopic database in section 3.3.3), therefore the validity range of these data is unknown and problems may arise by unknowingly using them beyond it. This is specially critical when considering the risks of extrapolating high-order polynomials.

That being said, this inaccuracy of higher-lying levels extrapolations is related to the anharmonicity of the real potential energy curve. Also, and since the expansion made use of the Born-Oppenheimer approximation, it is important to note that this model is inadequate close to the dissociation limit as the Born-Oppenheimer approximation fails for higher vibrational levels where vibration-rotation interactions need to be accounted for. Therefore, other methods need to be considered and this will be discussed in the next section.

2.3.2 Approaches based on the Reconstruction of the State Potential Curve

The traditional approach of using popular polynomial expansions such as Dunham's to determine the number of vibrational levels as described above and calculating their energies with the expression 2.18 is, as already discussed, questionable when extrapolating the Dunham expression beyond their validity range, so there is a need to employ different methods.

For levels with non-negligible anharmonicities, which is the case for most, it is more accurate to resort to numerical methods that reconstruct the state potential curve up to the dissociation limit and then determine the corresponding levels by solving the radial Schrödinger equation (see appendix A.2).

One may approach the problem by applying *ab initio* methods (derived from theoretical principles and with no empirical parameters), that use quantum chemistry knowledge based on the clamped nuclei approximation to calculate the potential energy curve [27]. *Ab initio* methods, however, are very computationally demanding and the calculated energies' accuracy is usually lower than by using spectroscopy constants measured experimentally, so they will not be considered in this work. It is, nevertheless, useful to keep these methods in mind as an alternative for higher-lying electronic states whose levels measured to get spectroscopic constants are very few and thus not allowing for a correct extrapolation.

One of the methods used in alternative is called the Rydberg-Klein-Rees (RKR) method (with its origin in the works [28–30] and explored in works such as [14]) and is the most commonly applied throughout this work, being more accurate than the ones previously mentioned.

This quasi-classical method uses experimental spectroscopic constants to start the reconstruction of the equilibrium region of the potential curve of a diatomic molecule electronic state - up to the validity range of the constants used. The RKR method is a first-order, semiclassical inversion procedure that proves to be more accurate than other common methods (such as *ab initio*), provided it is used inside its validity domain. Outside of this range, as it was the case for the Dunham expansion method, the result may be inaccurate; on the other hand, extrapolation by *ab initio* methods yields more accurate results.

The issue of validity ranges of spectroscopic constants not being stated in their sources and how this was dealt with will be explained in section 3.3.3, as well as the assessment of the associated risks.

In conclusion, the RKR method is useful for the determination of the lower part of the energy curves and further extrapolations are needed for the remainder of the curve.

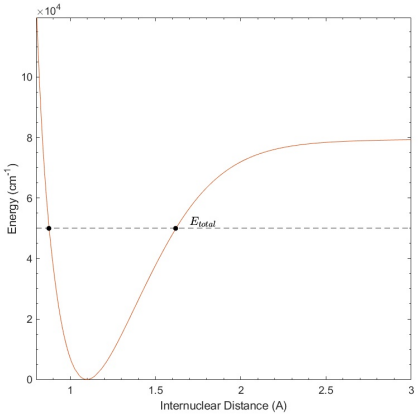

Figure 2.2: Representation of a potential curve with its turning points (points r_1 and r_2 from left to right) for a total energy.

The RKR method begins with a first-order JWKB quantization [31]:

$$(v+\frac{1}{2}) = \frac{1}{\pi}\sqrt{\frac{2\mu}{\hbar^2}}\int_{r_1}^{r_2}[E-V(r)]^{1/2}\,dr \tag{2.21}$$

with E being the total energy, $V(r)$ being the potential energy function, μ the reduced mass of the molecule, $\hbar$ is the reduced Planck constant ($h/(2\pi)$) and r_1 and r_2 being the inner and outer classical turning points, in figure 2.2, (points where potential energy V is approximately equal to the total energy, E, and the kinetic energy is zero; for a specific total energy, a molecule is confined to have internuclear distance, r, bigger than r_1 and smaller than r_2), respectively. Assuming there is a well-behaved single minimum potential around the equilibrium distance and also that the vibrational and rotational energies are smooth functions of v, the derivation of the RKR (which can be seen in detail in works such as [13, 32, 33]) yields two expressions:

$$r_2(v)-r_1(v) = 2\sqrt{\frac{\hbar^2}{2\mu}}\int_{v_{min}}^{v}[E(v)-E(v')]^{-1/2}\,dv' = 2f \tag{2.22}$$

$$\frac{1}{r_2(v)}-\frac{1}{r_1(v)} = 2\sqrt{\frac{2\mu}{\hbar^2}}\int_{v_{min}}^{v}B_v\,[E(v)-E(v')]^{-1/2}\,dv' = 2g \tag{2.23}$$

with $v_{min} = v(E=0)$, B_v being the rotation constant in $B_v(J(J+1))$ (see equation 2.17) and $E(v)$ being calculated with the expression for $G(v)$ (2.19). Equation 2.22 is obtained for non-rotating molecules (be-

ing known as the ”vibrational RKR equation”) and 2.23 for rotating molecules (”rotational RKR equation”). Their rearrangement results in:

$$r_1(v) = \sqrt{f^2 + \frac{f}{g}} - f \tag{2.24}$$

$$r_2(v) = \sqrt{f^2 + \frac{f}{g}} + f \tag{2.25}$$

It is also important to note that the integrals f and g are not defined in the upper limits, so a Gauss quadrature method has to be used to determine the f and g near the upper limit. As for the convergent part, the trapezoid rule was employed to solve the integral. The result is calculated by summing both parts.

Furthermore, it is important to state that the quantization of energy levels entails the definition of the values of v as integer numbers; however, the RKR method treats v as a continuous variable. This does not raise issues, as later, when obtaining the energy levels, the integer nature of v will be considered - contrarily, at this point, the treatment of v as a continuous variable allows for a more precise determination of the potential energy, as a larger number of points is obtained and used.

The near-equilibrium part of the potential curve is determined, so the extrapolation to the dissociation limit is now in order.

Different methods are available in the bibliography. The choice here fell on the extrapolation of the potential by a repulsive potential (equation 2.26) at shorter internuclear distances (the left side of the potential curve) and by a Hulburt and Hirschfelder potential (equation 2.27) [34] for longer ones (the right side) - a potential that consists in a two-parameter correction term to the usual Morse potential.

The expressions for the repulsive potential and the Hulburt and Hirschfelder potential are, respectively:

$$V_{rep}(r) = \frac{A}{r^p} \tag{2.26}$$

$$V_{HH}(r) = D_e \left\{ \left[1 - e^{-\alpha(r-r_e)}\right]^2 + \beta\alpha^3(r-r_e)^3 e^{-2\alpha(r-r_e)} \left[1 + \alpha\gamma(r-r_e)\right] \right\} \tag{2.27}$$

with r_e being the equilibrium internuclear distance and D_e the dissociation energy. A, p, α, β and γ are fitting parameters that have to be adjusted so continuity is guaranteed with the RKR part of the curve.

In some cases the use of Hulburt-Hirschfelder potential may lead to ”quasi-bound” portions of the curve (parts of the curve where quasi-bound states are allowed) before the potential decreases again to the dissociation limit - and this behaviour might not always have a physical meaning. In those cases, one may use an Extended Rydberg potential which avoids this behaviour and has the following expression:

$$V_{ERy}(r) = D_e \left\{ 1 - \left[1 + \alpha(r - r_e) + \beta(r - r_e)^2 + \gamma(r - r_e)^3 \right] e^{-\alpha(r - r_e)} \right\} \tag{2.28}$$

Details of cases where it was necessary to assess the existence of physical quasi-bound states and choose the adequate extrapolation method will be discussed later in section 3.3.

This entire process reconstructs the potential curve. Considering firstly a rotationless state case, the vibrational level energies may be determined by solving the radial Schrödinger equation for this potential curve - using the method proposed by Balint-Kurti et al. [35] and the typographical correction indicated in [13].

Naturally, for the part of the potential curve obtained with the RKR method, the energies calculated will be equal to those used as input (from the spectroscopic data), up to the numerical accuracy of the considered grid. The difference - and the value of this method - lies on the predicted vibrational levels of the remaining parts of the curve; these are now calculated from a smoothly extrapolated potential curve and the upper levels' energy values should be more accurate than by extrapolating polynomial expansions such as the Dunham expansion.

With respect to rotation, the potential for an arbitrary rotational number J may on a first approach be obtained by adding the centrifugal potential due to molecular rotation [15, 32, 36] :

$$V_J(r) = V_{J=0}(r) + \frac{\hbar^2 J(J+1)}{2\mu r^2} \tag{2.29}$$

The rovibrational levels energies may then be obtained by solving the radial Schrödinger equation (see appendix A.2) and the maximum J is found when the molecular potential is entirely repulsive (not allowing local minimums).

Another popular technique for the extrapolation of the potential curve, after obtaining the near-equilibrium part, is the so-called direct-potential-fit (DPF) analysis [36, 37] which was considered whenever the necessary data was available with great accuracy. This technique fits a chosen theoretical potential (such as Morse or Lennard-Jones potentials) to the reconstructed RKR potential, guaranteeing that it has a satisfactory behaviour as it approaches the dissociation limit. This method usually gives very accurate curves and is not as computationally expensive as the *ab initio* ones but presents some disadvantages: the choice of the theoretical potential for the fit leads to differences in the potential curve obtained by different authors, which makes it difficult for the generalization of the method; it requires extensive analysis and fitting of the experimental data.

2.4 Chemical Kinetics

Considering a gas in chemical equilibrium means its composition may only change in space because of temperature gradients, as the equilibrium composition is temperature-dependent. One may use this approximation at low temperatures, as although shocks may occur, the temperature gradients are not very abrupt and forward and backward chemical reactions cancel out, and the chemical composition

remains constant. This allows for chemical composition to be described by only two thermodynamic properties (for example, density and pressure or pressure and temperature).

However, as the flow velocity increases, more abrupt changes in the pressure or temperature fields occur - such as those verified in shock layers of hypersonic flows here considered - and the chemical equilibrium composition changes, as chemical reactions lead to a new equilibrium through molecular collisions. Since hypersonic flows have low characteristic flow times $\tau_f << \tau_e$, chemical equilibrium in the flow may only be reached long after the flow has crossed the body obstacle. The flow, accordingly, needs to be considered as chemically reacting and a finite chemistry model has to be accounted for in the governing equations.

One then needs to consider mass conservation for each species of the mixture, which was already included as additional equations in section 2.1. The source term in the mass conservation equation for each species (see 2.1) needs to be determined and to do so the chemical reactions have to be correctly modeled. A general chemical reaction r is described by:

$$\sum_s \nu'_{s,r} X'_{s,r} \underset{k_{b,r}}{\overset{k_{f,r}}{\rightleftharpoons}} \sum_s \nu''_{s,r} X''_{s,r} \tag{2.30}$$

where $\nu'_{s,r}$ and $\nu''_{s,r}$ are the stoichiometric coefficients of the reactants $(X'_{s,r})$ and reaction products $(X''_{s,r})$ respectively and $k_{f,r}$ and $k_{b,r}$ represent the rate constant for the forward and backward process respectively.

The net rate of formation of a species s involved in the reaction r can be written as:

$$\left\{\frac{d\left[X_s\right]}{dt}\right\}_r = \left(\nu''_{s,r} - \nu'_{s,r}\right)\left\{k_{f,r}\prod_s [X_s]^{\nu'_{s,r}} - k_{b,r}\prod_s [X_s]^{\nu''_{s,r}}\right\} \tag{2.31}$$

where $[X_s]$ is the concentration of species s and represents the number of moles of species s per unit of volume of the mixture. This equation expresses the net rate of formation of the species s through reaction r as a balance of the forward and backward reactions. These chemical rate constants are usually estimated from experimental data correlated through an Arrhenius equation such as:

$$k_{f,r} = A T_{f,c}^n \exp\left(-\frac{\theta_R}{T_{f,c}}\right) \tag{2.32}$$

where A, n and θ_R are experimentally determined model constants and $T_{f,c}$ is the rate-controlling temperature of forward reaction.

The backward rate constant $k_{b,r}$ may be calculated with $K_{eq,r}$, the equilibrium constant for concentrations for the reaction r, which can be calculated from statistical thermodynamics. The backward rate constant is then given by:

$$\frac{k_{f,r}}{k_{b,r}} = K_{eq,r} \tag{2.33}$$

Considering equation 2.31 and summing that over all elementary reactions r that involve the species s, the net rate of formation of said species is:

$$\frac{d\left[X_s\right]}{dt} = \sum_r \left\{ \frac{d\left[X_s\right]}{dt} \right\}_r \tag{2.34}$$

and the mass source term of equation 2.1 is then given by:

$$\dot{w}_s = \mathcal{M}_s \frac{d\left[X_s\right]}{dt} \tag{2.35}$$

where $\mathcal{M}_s$ is the molar mass of the species s.

More details on chemical kinetics of hypersonic flows can be found on Anderson Jr. [4].

The additional consideration of thermal non-equilibrium means that the determination of the forward and backward chemical reaction rates must take into consideration which thermal modes contribute to that reaction energy. That is usually done through modifying the $T_{f,c}$ of equation 2.32 to a rate-controlling temperature more adequate for the energy mode that kind of reaction makes use of. Works such as [38] consider this impact of thermal non-equilibrium in more detail and present the rate-controlling temperature for each reaction considered. As an reminder, we are not considering thermal non-equilibrium in this work, for the sake of simplicity.

2.5 Transport Properties

The Navier-Stokes equations in section 2.1 all present dissipative terms that have to be computed: those are explicitly present on equations 2.1 - 2.4 through the mass diffusion flux vector $\boldsymbol{J_s}$, the viscous stress tensor $[\boldsymbol{\tau}]$ and the conduction heat flux associated with each non-equilibrium thermal mode $\boldsymbol{q_{c,k}} = \kappa_k \nabla T_k$. The dissipative terms will model the natural transport of mass, momentum and energy by the chaotically random movement and collision of the gas mixture particles, in a microscopic perspective. These fluxes are essential for modeling the mass, momentum, and energy fluxes due to concentration, velocity, and temperature gradients, respectively.

The model used to determine these dissipative fluxes, their mathematical definition, the transport coefficient they entail, and the gradient responsible for each dissipative flux are summarized in table 2.3. The transport coefficients define how the gas responds to different gradients, being specially relevant where large gradients occur, such as at the shock layer region. D_s is the mass diffusion coefficient of species s, μ is the dynamic viscosity coefficient and κ_k stands for the thermal conductivity associated with thermal mode k .

Table 2.3: Transport properties.

Dissipative Flux	Symbol	SI Units	Expression	Transport Coefficient	Gradient	Model
Mass Diffusion	$\boldsymbol{J_s}$	m^2s^{-1}	$\boldsymbol{J_s} = \rho\mathcal{D}\nabla c_s$	$\mathcal{D}$	∇c_s	Fick's Law
Moment Diffusion	$[\boldsymbol{\tau}]$	kg $m^{-1}s^{-1}$	$[\boldsymbol{\tau}] = \mu\left(\nabla\boldsymbol{V} + (\nabla\boldsymbol{V})^T\right)$ $-3/2 \cdot \mu(\nabla\boldsymbol{V})[I]$	μ	$\nabla\boldsymbol{V}$	Newtonian Fluid
Heat Conduction	$\boldsymbol{q_{c,k}}$	J $m^{-1}s^{-1}K^{-1}$	$\boldsymbol{q_{c,k}} = \kappa_k\nabla T_k$	κ_k	∇T_k	Fourier's Law

A typical approach to determine the transport coefficients is to use the classical Chapman-Enskog solution of the Boltzmann equation [39]. This means solving a system of linear equations that is quite computationally expensive so this strategy is usually not followed; instead one may opt for the more effective approach of using approximate mixing rules that allow to obtain the effective transport properties of the gas mixture at specific composition, relying on simplifications to the Chapman-Enskog solution. Two models based on mixing rules will be presented next.

2.5.1 Transport Models

Wilke/Blottner/Eucken Model

This model [40] consists on the application of kinetic theory to the first order Chapman-Enskog relation. It assumes that all binary interactions have the same cross-section (with a hard-sphere geometry) and ignores inter-species interactions [41].

The global viscosity μ and the thermal conductivity κ_k for each mode's temperature is given by Wilke's mixing rule as a weighted sum on the individual species μ_s and $\kappa_{k,s}$:

$$\mu = \sum_s \frac{x_s\mu_s}{\phi_s} \quad \text{and} \quad \kappa_k = \sum_s \frac{x_s\kappa_{k,s}}{\phi_s} \tag{2.36}$$

where x_s is the species molar fraction and ϕ_s is a coefficient dependent on all possible interactions between species s and l and their molar masses $\mathcal{M}$:

$$\phi_s = \sum_l x_l \left[1 + \left(\frac{\mu_s}{\mu_l}\right)^{1/2}\left(\frac{\mathcal{M}_l}{\mathcal{M}_s}\right)^{1/4}\right]^2 \left[8\left(1 + \frac{\mathcal{M}_s}{\mathcal{M}_l}\right)\right]^{-1/2} \tag{2.37}$$

The individual species viscosities are computed using Blottner's [42] model:

$$\mu_s(T) = 0.1\exp\left((A_s\ln T + B_s)\ln T + C_s\right) \tag{2.38}$$

where T is the translational temperature of that species and A_s, B_s and C_s are curve fitted coefficients, determined for each species.

On the other hand, the species' thermal conductivity for each energy mode is determined using the generalized Eucken's relation [43], assuming a unit Schmidt number:

$$\kappa_{tra,s} = \frac{5}{2}\mu_s C_v^{tra,s} \tag{2.39}$$

$$\kappa_{rot,s=\mathrm{m}} = \mu_s C_v^{rot,s} \tag{2.40}$$

$$\kappa_{vib,s=\mathrm{m}} = \mu_s C_v^{vib,s} \tag{2.41}$$

$$\kappa_{exc,s\neq \mathrm{e^-}} = \mu_s C_v^{exc,s} \tag{2.42}$$

where $C_v^{k,s}$ is the specific heat at constant volume of the species s in each energy mode, and m represents molecular species while $\mathrm{e^-}$ represents electrons. In cases of thermal non-equilibrium, the different contributions of each species should be taken into the mixing rule of equation 2.37, accordingly to the multi-temperature model chosen.

Last but not least, the mass diffusion coefficient for each species is given by a single binary coefficient $\mathcal{D}$, assuming a constant Lewis number (defined as the ratio of thermal diffusivity to mass diffusivity and that may also be expressed in terms of the Prandtl number and the Schmidt number), $Le = 1.2$, for air:

$$\mathcal{D}_s = \mathcal{D} = \frac{Le\kappa}{\rho C_p} \tag{2.43}$$

where ρ stands for the mixture's global density, C_p is the mixture total specific heat at constant pressure, and κ is the total thermal conductivity.

Although simpler and less computationally expensive than other alternatives, this model's results are only reliable for relatively low velocities, with a maximum temperature of 10 000 K and a weakly ionized gas. Since the purpose of this work is to study high velocity and high temperature flows with high degrees of ionization, the Wilke model is inadequate in modeling such conditions' transport properties [44, 45].

Gupta-Yos Model

The Gupta-Yos model was first formulated and implemented by Gupta et al. [46], it relies on a simplification of the Chapman-Enskog solution and provides the transport properties using an approximate mixing rule. This simplification consists on an averaging of the interactions between particles of different species; this takes into account the cross-section for each collision in the multi-component gas mixture, making the Gupta-Yos model more physically accurate than Wilke's model, as the latter considers this cross-section to be constant for all interactions. Comparatively, although more computationally expensive, the Gupta-Yos model is more accurate for higher temperature flows, where ionization is already significant.

The transport coefficients appear as function of the collision terms $\Delta_{ij}^{(1)}$ and $\Delta_{ij}^{(2)}$, that give the strength of the interaction between each pair of species (s, l) as a function of the controlling temperature T_c and are defined by:

$$\Delta_{sl}^{(1)} = \frac{8}{3}\left[\frac{2\mathcal{M}_s\mathcal{M}_l}{\pi RT_c(\mathcal{M}_s+\mathcal{M}_l)}\right]^{\frac{1}{2}}\pi\overline{\Omega}_{sl}^{(1,1)}(T_c) \tag{2.44}$$

$$\Delta_{sl}^{(2)} = \frac{16}{5}\left[\frac{2\mathcal{M}_s\mathcal{M}_l}{\pi RT_c(\mathcal{M}_s+\mathcal{M}_l)}\right]^{\frac{1}{2}}\pi\overline{\Omega}_{sl}^{(2,2)}(T_c) \tag{2.45}$$

where R is the universal gas constant and $\pi\overline{\Omega}_{sl}^{(1,1)}$ and $\pi\overline{\Omega}_{sl}^{(2,2)}$ represent the average collision cross-sections, in m^2, computed using Gupta's curve fits [46]. The controlling temperature T_c will be the electrons' translational temperature T_e if the interaction involves an electron, otherwise T_c will be taken as the heavy species' translational temperature T_{tra}.

The mixture viscosity is then:

$$\mu = \sum_s \frac{x_s m_s}{\sum_l x_l \Delta_{sl}^{(2)}} \tag{2.46}$$

where m_s is the particle mass of the species s and x_s is its molar fraction.

The translational contribution of the heavy species and electron's thermal conductivities, κ_{tr} and κ_{e^-}, respectively, are computed as:

$$\kappa_{tra} = \frac{15}{4}k_B \sum_{s\neq\mathsf{e}^-} \frac{x_s}{\sum_l \alpha_{sl} x_l \Delta_{sl}^{(2)}} \tag{2.47}$$

$$\kappa_{\mathsf{e}^-} = \frac{15}{4}k_B \frac{x_{\mathsf{e}^-}}{\sum_l \alpha_{l\mathsf{e}^-} x_l \Delta_{l\mathsf{e}^-}^{(2)}} \tag{2.48}$$

in which k_B is the Boltzmann constant and α_{sl} is a coefficient function of the species molar masses:

$$\alpha_{sl} = 1 + \frac{\left(1-\frac{\mathcal{M}_s}{\mathcal{M}_l}\right)\left[0.45 - 2.54\frac{\mathcal{M}_s}{\mathcal{M}_l}\right]}{\left(1+\frac{\mathcal{M}_s}{\mathcal{M}_l}\right)^2} \tag{2.49}$$

The computation of internal contributions to the thermal conductivity are as follows:

$$\kappa_{rot} = \sum_{s=\mathsf{m}} \frac{x_s m_s {C_v}^{rot,s}}{\sum_s x_s \Delta_{sl}^{(1)}} \tag{2.50}$$

$$\kappa_{vib} = \sum_{s=\mathsf{m}} \frac{x_s m_s {C_v}^{vib,s}}{\sum_s x_s \Delta_{sl}^{(1)}} \tag{2.51}$$

$$\kappa_{exc} = \sum_{s\neq \mathsf{e}^-} \frac{x_s m_s {C_v}^{exc,s}}{\sum_s x_s \Delta_{sl}^{(1)}} \tag{2.52}$$

The total thermal conductivity in thermal equilibrium is:

$$\kappa = \kappa_{tra} + \kappa_{\mathsf{e}^-} + \kappa_{rot} + \kappa_{vib} + \kappa_{exc} \tag{2.53}$$

When the gas is in thermal non-equilibrium, each component κ_k is obtained from every species' individual contributions in the equations above.

The gas mixture diffusion coefficient is given by:

$$\mathcal{D}_s = \frac{1 - x_s}{\sum_{l\neq s} \frac{x_l}{D_{sl}}} \tag{2.54}$$

where $\mathcal{D}_{sl}$ is the binary diffusion coefficient involving two particles, which gives the diffusion velocity of each species relative to other species and is defined as:

$$\mathcal{D}_{sl} = \frac{k_B T_c}{p \Delta_{sl}^{(1)}} \tag{2.55}$$

with p being the total pressure of the gas.

Finally, the viscosity coefficient for a single individual species is:

$$\mu_s = \frac{5}{16} \frac{\sqrt{\pi m_s k_B T_c}}{\pi \overline{\Omega}_{ss}^{(2,2)}} \tag{2.56}$$

and each thermal conductivity for a single individual species is given by:

$$\kappa_{ktra,s} = \frac{75}{64} k_B \frac{\sqrt{\pi k_B T_c / m_s}}{\pi \overline{\Omega}_{ss}^{(2,2)}} \tag{2.57}$$

$$\kappa_{krot,s=\mathsf{m}} = \frac{8}{3} k_B \, c_{vrot,s} \frac{\sqrt{\pi k_B T_c m_s}}{\pi \overline{\Omega}_{ss}^{(1,1)}} \tag{2.58}$$

$$\kappa_{kvib,s=\mathsf{m}} = \frac{8}{3} k_B \, c_{vvib,s} \frac{\sqrt{\pi k_B T_c m_s}}{\pi \overline{\Omega}_{ss}^{(1,1)}} \tag{2.59}$$

$$\kappa_{kexc,s\neq \mathsf{e}^-} = \frac{8}{3} k_B \, c_{vexc,s} \frac{\sqrt{\pi k_B T_c m_s}}{\pi \overline{\Omega}_{s}^{(1,1)}} \tag{2.60}$$

with their sum giving the total thermal conductivity associated to a given species s:

$$\kappa_s = \kappa_{tra,s} + \kappa_{rot,s} + \kappa_{vib,s} + \kappa_{exc,s} \tag{2.61}$$

It is noteworthy that the Gupta-Yos model starts to diverge from the real solution at higher temperatures as a result of higher ionization degrees [44]. However, more accurate models, that considered fewer approximations, would be much more computationally expensive.

Ambipolar Diffusion

Another phenomenon to account for is that of the influence of the electric field present in plasmas, that contributes to the mass diffusion fluxes. In an ionized gas, charged species will create a local electric field and other charged species will interact with it - this will contribute to the diffusion of ions, since these particles will be pulled by the more mobile electrons; on the other hand, these interactions with heavier species will slow down the electrons, making both ions and electrons reach similar velocities, which will be mainly established by the species with more mass. This is the ambipolar diffusion effect and it enforces a quasi-neutral diffusion flux:

$$\sum_s q_s \boldsymbol{J}_s = 0 \tag{2.62}$$

where q_s is the charge per unit of mass of species s. As these electrostatic forces were not accounted for up to now, a correction should be applied to the diffusion mass fluxes of ions; this will be the ambipolar diffusion correction, that was proposed by Chen [47] for ions and is written as:

$$\mathcal{D}^a_{ion} = \left(1 + \frac{T_{e^-}}{T_{ion}}\right) \mathcal{D}_{ion} \tag{2.63}$$

where $\mathcal{D}^a_{ion}$ and $\mathcal{D}_{ion}$ are the corrected and non-corrected diffusion flux of the ion, and T_{e^-} and T_{ion} are the translational temperatures of the electrons and ions, respectively. If the gas is considered to be in thermal equilibrium, then $T_{e^-} = T_{ion}$ and $\mathcal{D}^a_{ion} = 2\mathcal{D}_{ion}$.

For electrons, another correction was proposed by Lee [48]:

$$\mathcal{D}^a_{e^-} = \mathcal{M}_{e^-} \frac{\sum_{s=\text{ion}} \mathcal{D}^a_s x_s}{\sum_{s=\text{ion}} \mathcal{M}_s x_s} \tag{2.64}$$

which results in $\mathcal{D}^a_{e^-} = \mathcal{D}^a_{ion}$ when there is only one species present.

Chapter 3

Model Updates and Implementation

This chapter provides a description of the implementation processes used for the simulations performed. It includes a description of the CFD code as well as the mesh generation process and discussions of the trajectory points studied and simulation strategy adopted.

The implementation of the physical and chemical models presented in Chapter 2 is also explored along with the input data utilized. Since one of the main goals of this work is the update of the thermodynamic properties database, special attention is given to the strategy, problems and solutions regarding the determination of energy levels, as well as analysis of the results.

3.1 SPARK CFD Solver

SPARK (Software Package for Aerothermodynamics, Radiation and Kinetics) is the CFD code used throughout this work. Developed by Lopez and Lino da Silva [49] and maintained at IPFN (Instituto de Plasmas e Fusão Nuclear) from Instituto Superior Técnico, this code simulates high-entropy hypersonic non-equilibrium flow. It was written in Fortran 03/08 under the object-oriented programming (OOP) paradigm, making it specially useful for its flexibility and extendability as it allows for the implementation of updated physical models, new numerical solvers, databases and mesh routines, thanks to their separation in different modules.

SPARK is capable of performing simulations in 0D (temporal relaxation), 1D (post-shock relaxation) or 2D (plane or axisymmetric flow) simulations. Euler or Navier-Stokes governing equations may be used, perfect and frozen gas assumptions may be selected, multi-temperature models customized and different kinetic models employed for chemically reacting mixtures. Furthermore, the code also allows the deployment of state-to-state models.

As for the numerical solvers, cell-centered time-dependent finite volume formulation is employed, where conservation equations are expressed in integral form over arbitrary quadrilateral cell. Regarding convective fluxes discretization, this is done with the second-order Harten-Yee scheme and a min-mod flux limiter, to avoid numerical oscillations. Regarding temporal discretization, implicit and explicit second-order schemes are available.

The SPARK code is in continuous development, with the possibility of updating the different modules and inclusion of new ones to add new phenomena to the simulations.

3.2 Trajectory Points of Interest

In this section, the requisites for the choice of conditions to be studied are presented.

For the Navier-Stokes equations to be validly employed, we first need to confirm the assumption of continuum flow. This will further ensure one may use the no-slip condition at the wall. To evaluate the regime flow, the dimensionless Knudsen number K_n is used, which compares the molecular mean free path length to a representative characteristic of the reentry body, l. If the ratio K_n is near or greater than unit, then the mean free path of its particles is comparable to the length scale of the problem and statistical methods, like Direct Simulation Monte Carlo, should be used instead of Navier-Stokes equations. The Knudsen number may be described as [7]:

$$K_n = \frac{\lambda}{l} = \frac{k_B T_\infty}{p_\infty \sqrt{2}\sigma l} \tag{3.1}$$

where k_B is the Boltzmann's constant, T_∞ and p_∞ are the temperature and pressure at the freestream, σ is the effective collision cross section (which in the hard-spheres approximations may be written as πd^2, where d is the mean collision diameter) and l is the characteristic dimension of the body, in this case the diameter of the meteoroid.

The body geometry, as well as the pressure, density and temperature of the free flow at the altitude the body is, will define the flowfield regime. To guarantee continuum regime, one makes sure that for all the simulations performed, the Knudsen number is smaller than 0.001.

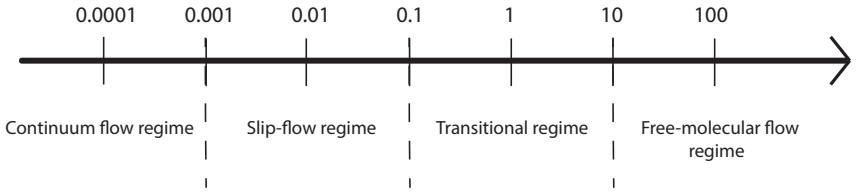

Figure 3.1: Knudsen number ranges and corresponding regimes.

As previously stated, although the work developed here focuses in higher velocity hypersonic flowfield simulations and the resulting abstract exploration of general conclusions, the application to meteoroid examples is still useful and timely, even for visualization's sake. Thus the choice of trajectory points of interest also takes inspiration on experimental data retrieved from meteoroid events.

Since one is interested in studying extreme conditions, and considering the behaviour of a meteoroid entering the Earth's atmosphere, the point in the trajectory to be simulated should correspond to the moment where the meteoroid is experiencing its maximum ram pressure; that maximum corresponds to the point where ram pressure ($p_{ram} = \rho V^2$) is equal to the meteoroid's bulk strength and fragmentation occurs.

Accordingly, one would want to determine usual meteoroid bulk strenghts and, from there, retrieve pairs of velocities and densities (or altitude, using the Earth atmosphere properties [50]) of interest for the simulations. However, the calculation of meteoroid bulk strenghts requires much more information about them than one may initially assume. Popova et al. [51] assembles data on 13 cases of meteorite falls with accurate tracking data on atmospheric passage (with data collected during its flight and from recovered fragments), infers their bulk strengths from velocities and altitudes at which first and main fragmentation occurred and compares them to strengths determined in laboratories for similar materials. It is concluded that the bulk strength during the flight seems to be significantly lower than the ones calculated in labs, and this supports the theory that the strength needed to cause a meteoroid's fragmentation is heavily dependent on its history before entering the atmosphere, its previous interactions and collisions throughout the universe. Thus, a direct relation between properties - such as size and material density - and ram pressure needed for fragmentation should not be made.

Instead, first fragmentation points found in literature for meteoroids will be used to determine typical ranges for bulk strengths and those will be used as the ram pressures for the simulations. The work of Popova et al. [51] represents a valuable source for this kind of information. The work also presents a comparison to other fireballs, from which fewer fragments were recovered, verifying that these 13 events were representative. Additionally, they concluded that for first breakup points in the atmosphere, typical bulk strengths vary between 0.1 and 1 MPa, much weaker than that of recovered meteoroid, which indicates very fractured parent bodies, much less coherent than the fragments that reach the ground. Meteoroids with enough mass to reach dense atmospheric layers while still having large velocities will tipically require ram pressure of 5 to 10 MPa to suffer further severe breakups and only in exceptional cases meteoroids survive 20 MPa of ram pressure.

From Popova et al. [51], first fragmentation was used as the reference point for this work as afterwards the fragments will interact with each other and the interest of this thesis is to study a stand alone body. It is recognized that ablation would occur between atmospheric entry and first fragmentation, but since its effects are not the subject of this study, low ablation between these two points is assumed and the inferred initial diameter may be used. The 13 meteoroids' first fragmentation points are represented in figure 3.2, which plots constant ram pressure curves in an altitude *vs* velocity graph. Two of the most well known meteor air burst events are also included in the figure, both having been the subject of plenty studies but still encapsulating significant uncertainties and questions: the Chelyabinsk event [52, 53], with a inferred diameter of 19 m, and the Tunguska event [5, 54], with 60 m. The data on the graph was used as a starting point for simulations and then higher velocities were also considered.

We focused on the typical range of ram pressure between 0.1 and 1 MPa. This work keeps a constant ram pressure and studies the effect of varying the velocity (and the corresponding atmospheric density to keep a constant p_{ram}). This will be done for a ram pressure of 0.1 MPa, as this is closest to the ram pressures usually felt by spacecrafts - using then a value of interest to meteoroids but also to spacecrafts, in opposition to a ram pressure of 1 MPa that a spacecraft could not strive to survive. To study the effect of the change in velocity, the diameter has to be remain constant as well, and a 60 cm diameter was chosen for the simulations as it landed on the range of the meteoroids presented here and

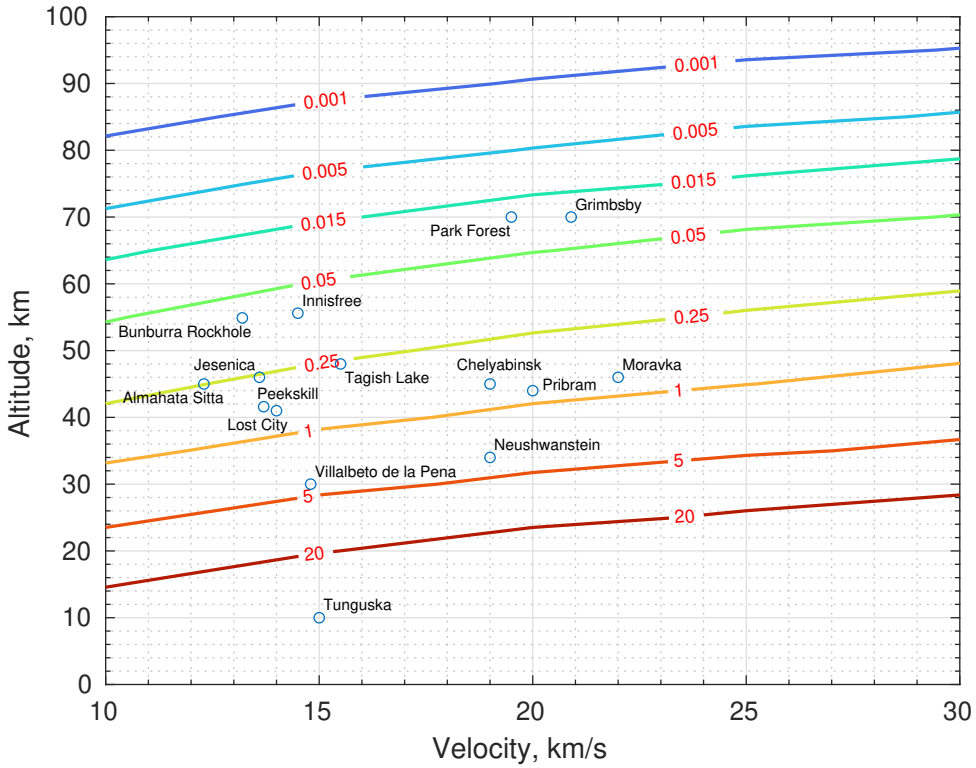

Figure 3.2: Meteoroids' points of fragmentation, with constant ram pressure curves plotted.

is an example of these smaller meteoroids.

The upstream conditions, as well as the specifications regarding the considered models are presented in Chapter 4 and include simulations with small increments in velocity (1 or 2 km/s) for two main reasons: to see the evolution in a more continuous way and to facilitate convergence of solutions, with the converged simulation of a certain velocity being used as a starting point for a new, higher velocity point.

In regards to Earth's atmospheric composition in the points of interest, the usual composition of 79% N_2 and 21% O_2 for the upstream flow was considered for all simulations. The chemical models considered, depending on the simulation, include the first 11, 13 or all the 15 of the following species: N_2, O_2, NO, N_2^+, O_2^+, NO^+, N, O, N^+, O^+, e^-, N^{++}, O^{++}, N^{+++}, O^{+++}.

3.3 Update of Thermodynamic Properties

As stated previously, phenomena such as dissociation and ionization are of the most importance in the cases studied here. To simulate this, a determination of rotation and vibration levels with high accuracy for the different states of the air species is in order, so the thermodynamic influence of higher-lying quantum levels may be properly accounted for at high-temperature conditions.

The determination of said rovibrational levels and the corresponding partition functions leads to the computation of thermodynamic properties such as enthalpy, entropy, internal energy and specific heat, through thermodynamic curve fits. Here a problem arises: the thermodynamic properties usually applied to aerothermodynamic simulations have an upper temperature limit (where they are valid) of 20 000 K,

as it was the case for the properties used as default in the SPARK code. These properties were derived from the polynomial curves described in NASA9 database, compiled by Gordon and McBride [55] and updated in [56], by the same authors. The validity temperature range is inadequate for the studies here performed, as the post-shock temperatures reached will surpass the 20 000 K mark, therefore an upper boundary of 100 000 K is considered in this work and is carried out through the determination of rovibrational levels and subsequent calculation of partition functions.

An updated and thorough compilation of vibrational and rotational energies of the various neutral and ionized air species is therefore necessary to study hypersonic flows at high temperatures and represents one of the main accomplishments of this work.

Regarding monoatomic species, the energy levels are already well documented in the NIST databases [24]. Therefore, dealing with these species is a simple task, just involving the fitting of thermodynamic properties polynomials to these energy values. The work necessary to determine the energy values of different states of diatomic molecules is more complicated and will be explained in the following subsections.

After obtaining the level energies and calculating the corresponding partition functions, the updated thermodynamic properties are fitted by polynomials that the SPARK CFD code will make use of. It is important to note that the computation of thermodynamic properties may be done analytically, through the explicit evaluation of equations 2.10 to 2.14 at each timestep. However, this method considers fewer spectroscopic constants and a harmonic oscillator approximation to determine level energies, allowing for less detail in the rovibrational contributions and less accuracy in determining energies when compared to the solving of Schrödinger equation. Also, as these calculations entail the sum of a significant number of exponentials, they are computationally expensive and, for higher velocities, very complicated to reach convergence. Therefore, the polynomial model will be used in this work instead, with curve-fits expressing the thermodynamic properties, with an advantage in accuracy and time consumed. The disadvantage of this method is that, due to a unresolved bug in the SPARK CFD code, it is not possible, at the moment, to employ a multi-temperature model with the polynomial thermodynamic model.

3.3.1 Rovibrational Energy Levels Determination for Diatomic Molecules

The calculation of the energy levels for air species is key for the update of the thermodynamic properties for conditions up to 100 000 K. The 15 species used throughout this work were updated (or even included for the first time, in the case of double and triple ionized species): N_2, O_2, NO, N_2^+, O_2^+, NO^+, N, O, N^+, O^+, N^{++}, O^{++}, N^{+++}, O^{+++}, e^-. The case of the electron particle will not be discussed as it has only two quantum levels (owing it to the direction of its spin vector). We will primarily focus here on the diatomic species and respective ions, as they require more extensive work. Nevertheless, the importance of the monoatomic species due to their prevalence is not overlooked and these will be updated as well.

Johnston and Brandis [3] have also tackled this necessity of extending the validity of the thermodynamic properties, while studying high temperature hypersonic reentry conditions and have compiled new

fits that widen the temperature range where they are valid up to 50 000 K. That update deals only with atomic species and their respective ions as they are the dominant species downstream of the shock.

For air's monoatomic species, one simply makes use of the set of electronic energy levels documented by NIST ([24]), calculates the partition functions from there, then calculates the thermodynamic properties for various temperatures and fits those values to polynomials expressions 3.2, 3.3, 3.4. It was decided to update molecules as well, since this will yield an up-to-date general thermodynamic database suitable for any arbitrary application, ranging from room temperature gases and plasmas up to very high temperature plasmas. One may also note that dissociation is not instantaneous after the shock wave, so there are a few cells where high temperatures coexist with molecular species prior to their dissociation.

The RKR method and subsequent extrapolations described in section 2.3.2 were carried out in a Matlab routine [14], that also solves the Schrödinger equation. Due to the uncertainty of the validity range of the considered spectroscopic constants, this process entailed many trials and iterations, with constant verification of possible nonphysical solutions and conservation of smoothness between different potential methods and a conservative approach to validity domains. Possible errors being made by using incorrect ranges were assessed through the calculation of partition functions.

The process of updating the spectroscopic database, mitigating the issues encountered, obtaining the potential curves and energy levels and subsequently obtaining the thermodynamic polynomials and properties, using the theory already explained, will be described in the following sections.

3.3.2 Thermodynamic Database Legacy

As previously stated, the default database used in the SPARK CFD code is the Gordon and McBride (NASA9) database.

The coefficients stored in the thermodynamic databases reproduce the data of those properties' values for each temperature (those being calculated using the concept of partition function and equations 2.11 to 2.14) through the following expressions, in their dimensionless form:

$$C_p^0(T)/R = a_1 T^{-2} + a_2 T^{-1} + a_3 + a_4 T + a_5 T^2 + a_6 T^3 + a_7 T^4 \tag{3.2}$$

$$H^0(T)/RT = -a_1 T^{-2} + a_2 \frac{\ln T}{T} + a_3 + a_4 \frac{T}{2} + a_5 \frac{T^2}{3} + a_6 \frac{T^3}{4} + a_7 \frac{T^4}{5} + \frac{b_1}{T} \tag{3.3}$$

$$S^0(T)/R = -a_1 \frac{T^{-2}}{2} - a_2 T^{-1} + a_3 \ln T + a_4 T + a_5 \frac{T^2}{2} + a_6 \frac{T^3}{3} + a_7 \frac{T^4}{4} + b_2 \tag{3.4}$$

Enthalpy and entropy are obtained by integrating $C_p^0(T)$ and $C_p^0(T)/T$ respectively, in respect to T; b_1 and b_2 are integration constants.

The NASA9 database does not contain information of N^{++}, O^{++}, N^{+++} and O^{+++}; these ions also had to be included. Naturally, there was no need to include double ionization of the molecular species, as

those would have negligible life times and the molecules will dissociate completely before the formation of said ions.

3.3.3 Update of the Spectroscopic Database

The update of the spectroscopic database to be used for the RKR part of the potential curve reconstruction presented itself as a laborious and essential task.

The compilation of this updated database was a ”labor of love” and required a thorough research of previous work and attention to detail, as small typos in data may lead to nonphysical solutions - or, something worse and very typical in the field of aerodynamics: results that appear correct, yet are not.

The data is collected from various authors that are referenced in the table 3.1 and those in appendix B.1. Special care was taken to confirm with multiple sources whenever it was possible and this allowed for the correction of some typos. Nevertheless, this was not possible for some states, as some have not been thoroughly studied yet, with theoretical and experimental data not always matching, and others, specially high lying states, having large uncertainties associated with them, being difficult to determine with accuracy for the energies involved in these high energy transitions. To deal with these concerns, experimental data, obtained from observations of energy transitions, was prioritized whenever available; for some high lying levels the reconstruction of the potential energy curve and energy levels determination was limited to the levels already experimentally observed, with no extrapolation; additionally, although some authors only focus on the determination of vibrational constants and others on rotational constants, it was given preference to authors that studied both, as the two types of constants are related and mixing data from different authors sometimes led to inconsistencies and impossible solutions.

The collected data has been carefully and critically curated. It was, unfortunately, not possible to also present the error limits associated, due to the lack of information for several states and inconsistent error presentations throughout the other states that would have meant a large increase in time just to uniformize them.

The bibliography used here is vast in the number of references and in the span of years it covers. Some of the ”bibles” such as Huber and Herzberg’s volumes [26, 57] - that compiled the constants of every electronic state known to that date for diatomic molecules - and the works of Lofthus [58] and Krupenie [59] - that focused on diatomic nitrogen and diatomic oxygen - remain important nowadays, with the more recent works built from these first ones or at the very least including comparisons and remarks on improvements obtained. In fact, many of these values remain valid today, with various different experiments confirming them. In regards to the lower energy states, most have been observed and are listed in the earlier bibliography here referenced. However, in recent years, experiments have been developed that allow for a more accurate observation of transitions: the Doppler effect affects the observed transitions in a molecule as it moves, broadening the energy center and creating a gaussian shape; to avoid this phenomenon, experiments are performed at low temperatures, so the molecules move less and the transition energy has a Dirac shape instead of a gaussian, benefiting the accuracy and allowing for more precise energy values calculation and better fittings to those values. This is useful

for the more fundamental states, but the same procedure cannot be applied to the higher lying states as, for the low temperatures necessary, those states are not populated (according to the Boltzmann distribution). As such, these higher lying electronic states were observed and included in works published after the "bibles", but did not have major updates in the last years, as these more recent techniques cannot be applied to these states or to transitions involving higher vibrational levels.

As stated, experimental data was preferred whenever possible. The experiments where they come from are of a wide variety, with the most important ones being electronic spectra in emission or absorption from the infrared to the ultraviolet, rotation-vibration spectra in the near infrared and rotation spectra in the infrared and microwave regions. Other experiments, involving molecular beam electric, magnetic resonance and electron spin resonance spectra have also provided useful information. Polynomials are then created that fit the experimental data and these give the spectroscopic constants of the tables below, that will describe the data within their validity ranges. Theoretical data is used to fill gaps and complement the experimental data.

Higher-order terms of said expression 2.17 are considered negligible in RKR calculations, so the approximations used in the routines neglect those terms; however, these were included in the updated database, when available, to make it more flexible for future methods that might include them.

Extending this air database was an important work, which usefulness is expected to translate to other areas that make use of spectroscopy, beyond the modelling of hypersonic high temperature flows, and to last for a long time, with future updates being made from this. In fact, and when compared to models and codes, databases' usefulness usually prevails in time. It is our hope that this work can be helpful for studies to come.

Table 3.1 presents the spectroscopic constants compiled for the O_2 molecule. 9 electronic states are listed with their vibrational (ω_e, -$\omega_e x_e$, $\omega_e y_e$, $\omega_e z_e$, $\omega_e a_e$) and rotational constants (B_e, α_e, γ_e, δ_e). $T(e)$ is defined as the minimum potential energy of each electronic state, corresponding to the point of the internuclear distance of equilibrium; this minimum has a vibrational quantum number of $v = -\frac{1}{2}$ and its energy is calculated in relation to the minimum potential of the species ground level. $T(e)$ of the ground state ($X^3\Sigma_g^-$ for the O_2 molecule) is 0 and represents the origin point ($E = 0$) to which all other energies are calculated from, for that molecule. Some works use different origins and definitions of $T(e)$, something to keep in mind while compiling these kind of data. For example, the points where $v = 0$ for the ground state are sometimes used as having $E = 0$. Here, the origin is always the $T(e)$ of the ground state of the species and the $T(e)$ of each state is always the minimum of the potential curve. One might note that there are some vanishingly small constant terms (Y_{00} in the Dunham expansion) associated to this minimum, but these won't be discussed here. One may refer to [60] for more details. In this work, the energy of an excited state relative to the $v = 0$, $J = 0$ level of the corresponding ground state will be referred to T_0, and the difference between T_0 and $T(e)$ is known as zero-point energy.

The same happens with the definition of dissociation limit energy, with different bibliography using different values according to the coordinate system preferred. Here, the value presented for D_e (dissociation energy) of a state is the energy of the dissociation limit of said state relative to $T(e)$ of the ground state. This means that states who dissociate to the same atomic species will have the same

D_e, while if one were to use the value in relation to the state's own $T(e)$, it would not be as intuitive to see if various states had the same dissociation products. D_e values were also compiled from literature, having been calculated through various experiments. The dissociation energy of the ground state of the N_2 molecule [37], for example, was determined from an analysis of excited-state predissociation data, by Roncin et al. [61]. Recently, other studies corroborated this finding, such as measurements using pulsed field-ionization photoelectron-photoion coincidence methods by Tang et al. [62]. Tables in appendix B.1 present the correspondence between dissociation products and dissociation energy for the states considered in this work.

The spectroscopic constants and other useful data concerning the O_2 molecule is presented in table 3.1, with its electronic states indicated in the first column and organized in a way that the bottom line has the ground state and the top line has the state with higher $T(e)$. The corresponding tables for O_2^+, N_2, N_2^+, NO, NO^+ can be found in appendix B.1.

Table 3.1: Updated spectroscopic database and other relevant data for reconstruction of O_2 potential curves. The values tagged with (*) were estimated in this work.

State	T(e) (cm^{-1})		ω_e	$-\omega_e x_e$	$\omega_e y_e$	$\omega_e z_e$	B_e	α_e	γ_e	δ_e	v_{max}^{valid}	Dis. Prod.	Extrap.	Ref.
		Y_{00}	Y_{10}	Y_{20}	Y_{30}	Y_{40}	Y_{01}	Y_{11}	Y_{21}	Y_{31}				
O_2														
$d^1\Pi_g$	69180		1626.4	-163.67			0.819	-0.0389			1*	-	-	[57, 63]
$C^3\Pi_g$	65530		696.71	-13.604	1.7698		0.9637	-0.023527			2*	-	-	[57, 64]
$B^3\Sigma_u^-$	49793		709.5	-10.92	-0.0176	-0.018	0.81878	-0.012695	-1.3919e-04	-3.947e-05	19	$O(^3P) + O(^1D)$	HH	[57, 65–67]
$A^3\Sigma_u^+$	35397.8		799.07	-12.16	-0.550		0.9106	-0.01416	-0.00097		4*	$O(^3P) + O(^3P)$	ER	[57, 59]
$A'^3\Delta_u$	34690		850	-20			0.96	-0.0262			5*	$O(^3P) + O(^3P)$	HH	[57, 59]
$c^1\Sigma_u^-$	33057.3		794.29	-12.736	-0.2444		0.9155	-0.01391	-0.00074		5*	$O(^3P) + O(^3P)$	ER	[57, 64]
$b^1\Sigma_g^+$	13195.1		1432.77	-14.00			1.40037	-0.01820	-4.20e-05		3	$O(^3P) + O(^3P)$	HH	[57, 59]
$a^1\Delta_g$	7918.1		1483.5	-12.90			1.42640	-0.0171			5*	$O(^3P) + O(^3P)$	HH	[57, 59]
$X^3\Sigma_g^-$	0	0.275	1580.1932	-11.9808	0.047475	-0.00127	1.445622	-0.01593	6.4065e-05	-2.846e-06	21	$O(^3P) + O(^3P)$	ER	[65, 67, 68]

After collecting the data for a given state, its potential curve was reconstructed, with the RKR method and subsequent extrapolation described in sections 2.3.2 and carried out in a Matlab routine. This allowed for troubleshooting where some errors in the data were found as the resulting curves did not represent physical realities. It was also important for choosing the best extrapolation potential that conserved the smoothness between the RKR and extrapolated sections of the curves as well as assessing if the existence of some quasi-bound states that appeared by using the Hulburt and Hirschfelder (HH) potential was a real feature or a product of the numerical method, by comparing it to other works. In cases where there was no information to assess this, the more conservative route was taken and the Extended Rydberg (ER) potential was used instead. Other extrapolations methods were employed when the required information was available and the results were deemed more accurate - as was the case for the ground state of the N_2, in which a direct-potential-fit was used. The extrapolation potential used for each state is also indicated in the tables with the spectroscopic data. For some higher lying states, with few information available or small number of vibrational levels fitted, a plausible extrapolation was not always possible. In those cases and to avoid errors, the reconstruction of the curve was limited to the near equilibrium RKR part. This is also indicated in the tables, using (-), as is the case for $d^1\Pi_g$ and $C^3\Pi_g$ of O_2.

As discussed in 2.3.2 , the validity domain of the spectroscopic constants is an important information that is often not available. Studies are made and spectroscopic constants calculated without disclosing the number of vibrational levels fitted to obtain them. Thus, there is a risk of using those constants for levels where they are not valid, obtaining incorrect potential curves. That being said, whenever the information was available, the vibrational level limit of validity was used to define the point until which the RKR method would be used and for higher levels an extrapolation was employed. For the cases where the validity range of the spectroscopic constants used is unknown, a process of trial and error was carried out, by experimenting possible limits and constantly checking for possible nonphysical solutions and conservation of smoothness between potentials. A conservative approach was used, by avoiding large v_{max}^{valid}, as one would rather use the RKR method in fewer levels, than use it outside the validity domain. Furthermore, being the majority of these states higher lying ones, the conservative approach is in agreement with the smaller number of vibrational levels that is expected to have been observed under these conditions.

The impact of choosing a validity range empirically was explored through the calculation of partition functions (2.11) of the state and by concluding that the difference from a case with a conservative number of vibrational levels and another with an approximate number (for example v_{max}^{valid} being 5 or 7) would generally be in the 5% range, even for higher temperatures, only presenting greater differences in some cases for temperatures close to 100 000 K. For example, for the $a^1\Delta_g$ electronic state of O_2, the difference in its partition function using v_{max}^{valid} of 5 and 7 was assessed, with the first resulting in 41 vibrational levels and the second in 40; the difference in the partition functions was of 2% for 100 000 K and even less for lower temperatures. Considering the higher-lying $c^1\Sigma_u^-$ state, the same analysis was performed, with both v_{max}^{valid} of 5 and 7 resulting in 21 vibrational levels and a maximum difference between their partition functions of 0.5%. This is an expected behaviour, as one can see from analyzing the partition function expression that the inclusion of said energetic levels in the sum will not impact the Q value greatly. Larger differences were encountered when using higher v_{max}^{valid}, which pointed out that the number of levels fitted from would likely be smaller, so the conservative approach was indeed preferable.

The values for the domain limit, v_{max}^{valid}, are indicated in the tables, for each state, either when taken from the bibliography or when used here from empirical analysis (these values are tagged with (*)).

Finally, something else to keep in mind is that these states should not only be analyzed standalone, but also plotted all together. This gives an important overview of possible interactions that could be incorrectly represented. Some examples of this will be presented afterwards. These interactions were considered and led to further iterations of extrapolation methods and v_{max}^{valid} used to more accurately model the physical reality.

3.3.4 Potential Curves Reconstruction

Using the spectroscopic constants reported above and the extrapolations methods deemed appropriate, the O_2 potential curves (PC) were reconstructed. They are presented next, in figure 3.3, as well

as the PC for the NO molecule in figure 3.4. Some of their vibrational levels (for $J = 0$) are also marked in the figures and the dissociation products indicated. In the neutral species plot, it was included the ground state of the respective ion. The potential curves for N_2, N_2^+, O_2^+ and NO^+ are presented in appendix B.2.

Analyzing the potential curves, one of the first conclusions drawn is that most states are in overall agreement with other bibliography that represent them. These are, for example, Gilmore [33] and Krupenie [59]. Nevertheless, other states are different since we considered more up to date data or better reconstruction models - as was the case for the ground state of O_2 that uses more recent spectroscopic data than [33] and [59] and for the ground state of N_2, that uses a DPF (direct-potential-fit) extrapolation developed more recently. Besides, for some states, such as $L'^2\Phi$ of NO, no representation was found in the literature. However, a conservative approach of its representation leaves little chance to error.

There are quite a few interesting conclusions and remarks regarding these PC's. Starting with the NO plots, one may observe that there are two curves for the $C^2\Pi_r$ and $B^2\Pi_r$ electronic states, one for each. In [33], these states are "joined" into a single $^2\Pi_r$ double minimum curve. To explain this and our choice of representing as two cut curves, perturbations and avoided crossing must be first mentioned.

Although smooth curves are the ideal situation, reality is not always straightforward. Occasionally, perturbations, interactions and deviations exist and make our job harder - but more interesting. These perturbations happen when a vibrational level of one electronic state falls close to a vibrational level of another state that has the same symmetry and multiplicity. In these cases, there are two ways of calculating potential curves: through adiabatic or diabatic processes. The adiabatic theorem [69] states that a physical system remains in its instantaneous eigenstate if a given perturbation is acting on it slowly enough and if there is a gap between the eigenvalue and the rest of the Hamiltonian's spectrum.

The diabatic process occurs when rapidly changing external conditions prevent the system from adapting its configuration during the process, so spatial probability density remains unchanged. Mathematically, this generally translate to no eigenstate of the final Hamiltonian having the same functional form as the initial state and the system ends in a linear combination of states that sum to reproduce the initial probability density. On the other hand, the adiabatic process consists on gradually changing conditions that allow the system to adapt its configuration, so the spatial probability density is changed by the process. This allows for a system that starts in an eigenstate of the initial Hamiltonian to end in the corresponding eigenstate of the final Hamiltonian. These processes, their distinction and the interactions explained next involve heavy mathematical formulation, that can be explored in detail in [70].

The behaviour of the potential curves will depend on the process. When two electronic states change their energy order (as molecular geometry is changed with the internuclear distance), their energies may become equal at a point (the curves are said to cross, diabatic surfaces in 3.5 (a)) or only come close and deviate (adiabatic surfaces in 3.5 (a)) - the crossing is avoided. This latter behaviour is displayed in adiabatic processes involving states with the same symmetry and is called avoided crossing [71]. For example, in the $C^2\Pi_r$ and $B^2\Pi_r$ of NO in [33], the $v = 3$ level of the first and the $v = 13$ level of the second may belong together, forming a combined state, due to an avoided crossing. It happens when PC's would potentially cross but due to the process happening slowly, it allows for adaption: the

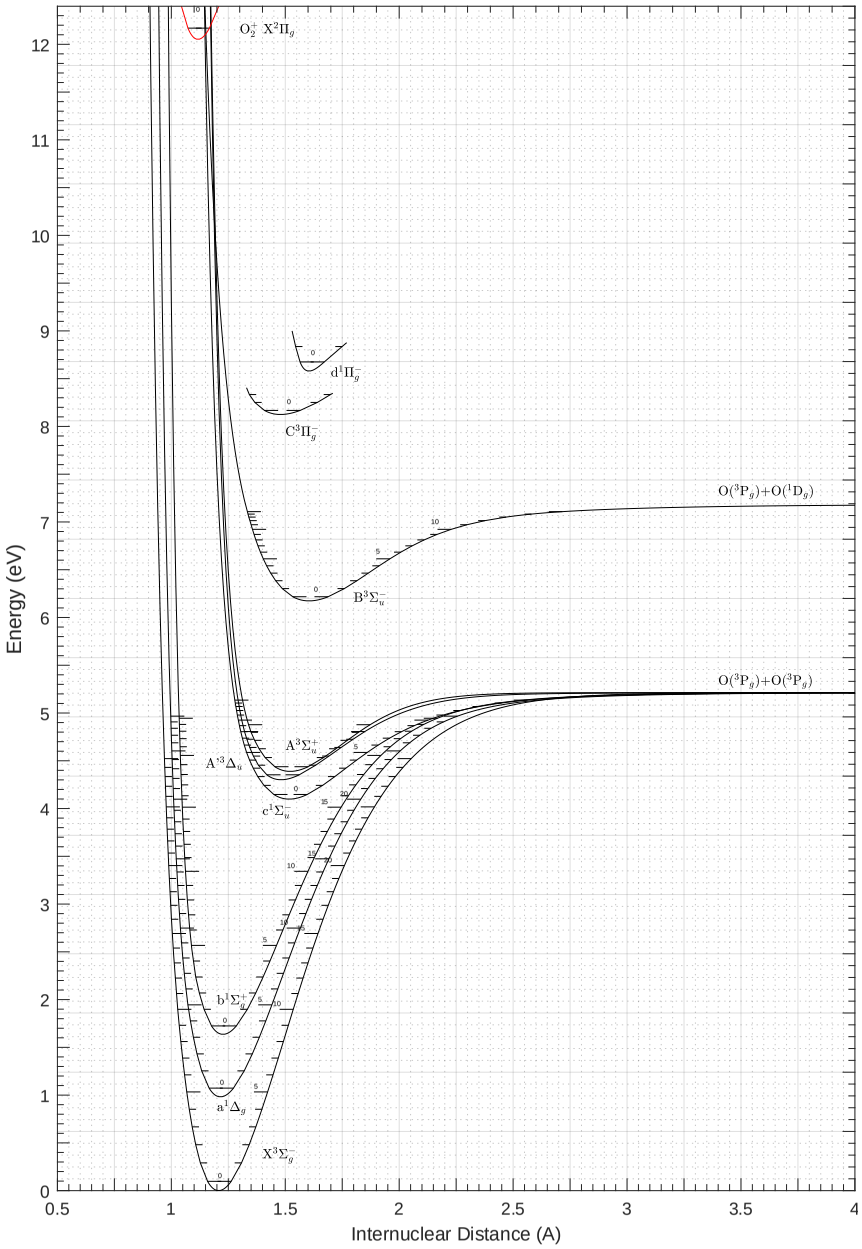

Figure 3.3: Potential curves for O_2 states.

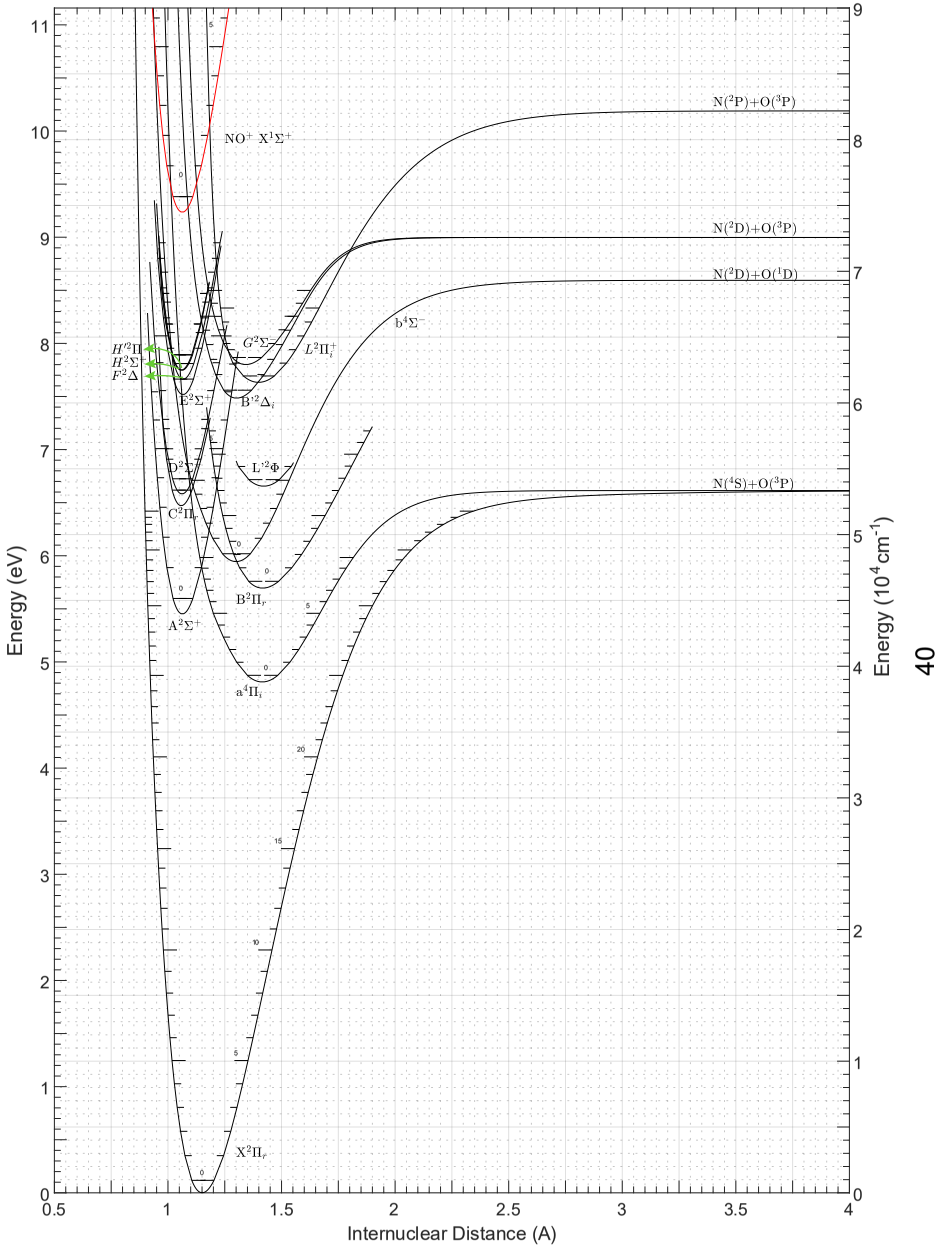

Figure 3.4: Potential curves for NO states.

electromagnetic potentials interact and repulse each other.

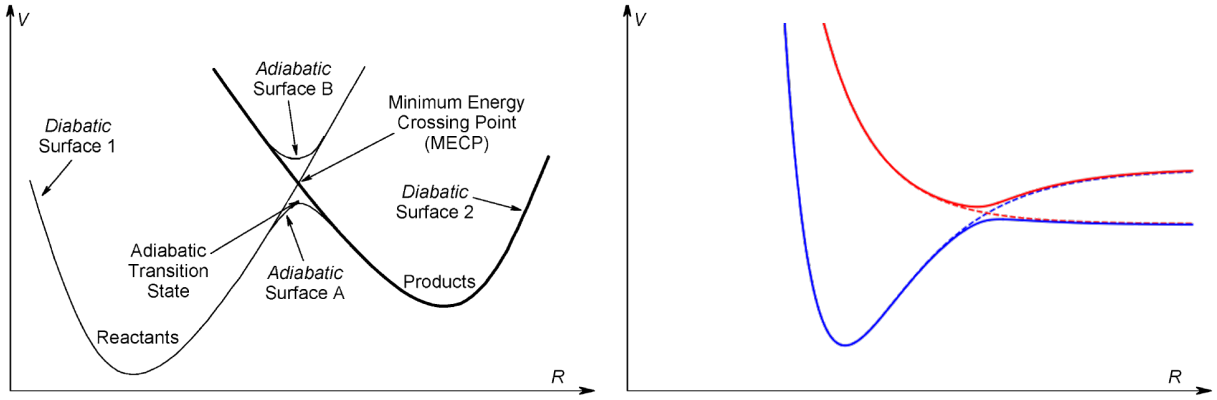

(a) Avoided crossing between two electronic states, adapted from [72].

(b) Avoided crossing between potential curve with bounded states (blue dotted line) and potential curve of a repulsive state (red dotted line), adapted from [73].

Figure 3.5: Avoided crossing.

However, it is not possible to represent this accurately through the RKR method. An alternative is to calculate the curves as if they were unperturbed (diabatic), but this might be difficult to do, as, for example, for the $C^2\Pi_r$ its dissociation limits are not known. Besides, it does not represent the physical reality of the interaction between two states with the same symmetry of a diatomic molecule.

Instead, one can opt to do what is represented in the figure 3.4: to limit the determination of the curve to the unperturbed levels known experimentally and not extrapolating it beyond where the interaction would occur. This was the method chosen to deal with these kind of perturbations for the $C^2\Pi_r$ and $B^2\Pi_r$ electronic states of the NO molecule as well as other states where the avoided crossing would happen (another example is the $C^3\Pi_u$ and $C'^3\Pi_u$ states of the N_2 molecule, whose plots can also be compared to [33]). Since these states are higher lying ones, the omission of some upper vibrational levels will have little impact in the partition functions.

Additionally, one may observe that in the figure 3.4 the following NO potential curves have only their RKR part represented: $A^2\Sigma^+$, $D^2\Sigma^+$, $E^2\Sigma^+$ and $H^2\Sigma^+$. This is also due to avoided crossings that would occur between those states and ones that exist but are not represented in the picture: repulsive states. When one excites a molecule from a state to another, the electronic wave may reach a configuration that is unstable and corresponds to a repulsive state. This is an electronic state that has no potential energy minimum. Therefore it is unbounded, and since systems tend to their minimum energy point, it converges to the dissociation energy while always decreasing its potential energy; the atoms repel each other, the internuclear distance increases to infinity and the molecule dissociates - the equilibrium of repulsive states is dissociation. Because it has no contained well, this kind of states has no discrete vibrational energy levels, forming instead a continuum. A representation of a repulsive state can be seen in 3.5 (b), with the red dotted curve.

In plasma studies, this is frequently explored, by colliding electrons with a molecule, one may excite the latter to an unstable repulsive state that dissociates spontaneously, helping determining electronic

impact dissociation rates. Spectroscopy detects these states easily as they appear as a strong and continuous feature in the absorption or emission spectrum.

Some repulsive states, namely the $^2\Sigma^+$ can be seen in [33] and would cross the $A^2\Sigma^+$, $D^2\Sigma^+$, $E^2\Sigma^+$ and $H^2\Sigma^+$ curves of the NO molecule. Following the avoided crossing rule, electronic interactions between them will prevent the crossing and it was chosen to not extrapolate the curves beyond their validity range for RKR, calculating only the fitted vibrational levels.

Additionally, there is another reason why these states' levels should only be calculated for the near equilibrium: the perturbations they would have with one another. Rydberg states are electronically excited states that follow the Rydberg formula while converging to an ionic state, with their energies converging on the energy of the ion. Following the theory of discrete levels' energies, they become closer and closer together as we go up the principal quantum number ladder, with an infinite number of orbitals piling up together before ionization. This study (and the Rydberg formula to describe energy levels) was first developed for the classical example of a hydrogen atom alone in the universe versus two atoms, and how the concepts of infinity and ionization energy are adapted, but it is expandable to molecules as well. These convergence of Rydberg states is easily observed in the NO plot of potential curves, with the $A^2\Sigma^+$, $D^2\Sigma^+$, $E^2\Sigma^+$, $F^2\Delta$, $H^2\Sigma^+$, $H'^2\Pi$ states piling up and converging to the ground state of the NO^+ ion. Being so close together, it is impossible to not have electronic interactions and perturbations; so, it was opted once again to only determine the levels used for the fitting of spectroscopic constants. The same happened regarding the N_2 molecule, in appendix B.1.

Other examples of states that were not plotted in their entirety are those for which there is little information regarding the spectroscopic constants; in these instances, only the first couple vibrational levels were usually observed and fitted, so extrapolating is not advised. $L'^2\Phi$ of NO, $C^3\Pi_g^-$ and $d^1\Pi_g^-$ of O_2 are examples of said states. The shape of $d^1\Pi_g^-$ also points to possible perturbations.

Finally, most electronic states represented in the figures, with $J = 0$, only allow for the system to occupy bounded states - quantum states in which a particle is subject to a potential such that the particle remains confined in one or more regions of space (here, the potential well), taking on energy values always lower than the potential at the infinities.

However, the calculation of quasi-bound states is allowed - mostly for higher J values, but sometimes for $J = 0$ states as well. An example of an electronic rotationless state that entails quasi-bound states is $C^2\Sigma_u^+$ of N_2^+ in B.2, where the potential curve tendency of increasing and then decreasing while it converges to dissociation allows for the existence of states with higher energy than the potential at the dissociation.

Quasi-bound states can then be defined as having closed boundary conditions at one side and open boundary conditions at the other side (picturing it in just one dimension), with their wave function decaying to zero only at the closed side. Their existence is due to perturbations (variations of some physical parameter) of true bounded states, and their unstable nature was recognized by Oppenheimer [74], who also estimated their small lifetimes. The mathematical formulation of these states is expanded in detail in [75].

These quasi-bound states may spontaneously dissociate through quantum tunneling, with the wave

function being able to propagate through a potential barrier. This means that system occupying a bounded state represented in figure 3.6 (a) would have its particles confined between points a and b, with its wave function being zero outside of that region. In the quasi-bound state, tunnel effects allow for a crossing between points d and e.

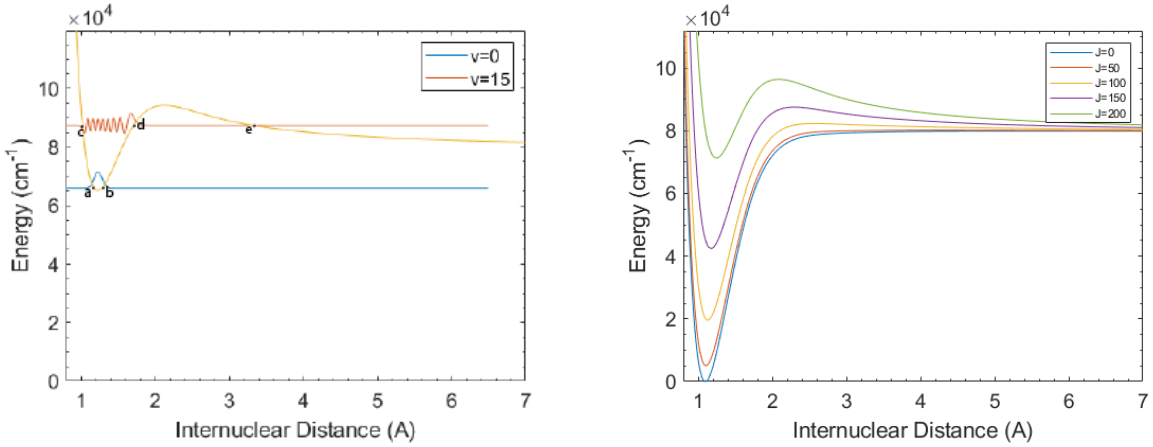

(a) Potential curve for J = 190 showing the wavefunctions for the vibrational level v = 0 and v = 15 with the corresponding a, b, c, d and e points.

(b) Potential curves for J = 0, 50, 100, 150 and 200 of N_2 ($X^1\Sigma$).

Figure 3.6: Quasi-bound states.

Lino da Silva et al. [15] studied the influence of these states on overall partition functions, concluding that even for temperatures as high as 100 000 K, the difference due to inclusion of quasi-bound states is limited to 10%, for the electronic ground state of N_2. For higher-lying electronic states, due to their higher energy values and reduced lifetimes, quasi-bounds will have less influence.

Sometimes, the appearance of quasi-bound states is strictly a consequence of the numerical extrapolation method used and they do not represent a physical reality. This was the case of, for example, $a^4\Pi_i$ and $G^2\Sigma^-$ rotationless states of NO and $L^2\Pi$ of the same molecule. For the first two, Gilmore [33] represents their curves without quasi-bound states and, since no other literature points to the physical existence of said states, it was decided to extrapolate said curves with an Extended Rydberg potential. For $L^2\Pi$, since there was no evidence in literature that this represented reality, the conservative route was taken and the Extended Rydberg potential was used instead, obtaining bounded states for the J=0 potential curve of the electronic state.

For most electronic states, for some $J > 0$ values, quasi-bound states are encountered and classically allowed, being accounted for in this work, as they were in works such as [15]. Figure 3.6 (b) represents potential curves for a variety of J quantum numbers for the ground state of the N_2 molecule. One may see that for J=0 only bounded states exit, while for J=200 there will be both bounded and quasi-bound states.

It is, however, noteworthy that if a rotational potential curve had its local minimum higher than the dissociation energy, the states associated to them would not be accounted for in this work, as they are highly unstable, and hence short-lived. They may therefore be safely ignored.

3.3.5 Determination of Rovibrational Levels

The following step was the determination of the rovibrational levels. To do this, equation 2.29 is used to determine the potential for each rotational number and then the radial Schrödinger equation A.20 has to be solved, giving as eigenvalues the observables of energies and each of its eigenstates defining the corresponding wavefunction. The obtained energy for each rovibrational level, together with its electronic, vibrational and rotational quantum numbers and its degeneracy [1] ($g_e * g_J = g_e * (2J + 1)$) are calculated and recorded.

The maximum vibrational and rotational quantum numbers reached by each electronic state are reported in table 3.2 for the O_2 molecule ($C^3\Pi_g$ and $d^1\Pi_g$ only have vibrational numbers of $v = 0-2$ and $v = 0 - 1$, respectively, since only the RKR part is being considered). The corresponding tables for the other diatomic species are in appendix B.3.

Table 3.2: Maximum vibrational and rotational quantum numbers found for each state of the O_2 molecule and number of rovibracional levels of each.

O_2	$X^3\Sigma_g^-$	$a^1\Delta_g$	$b^1\Sigma_g^+$	$c^1\Sigma_u^-$	$A'^3\Delta_u 4$	$A^3\Sigma_u^+$	$B^3\Sigma_u^-$	$C^3\Pi_g$	$d^1\Pi_g$
v_{max}	43	40	35	20	14	12	22	2	1
J_{max}	184	166	153	103	90	88	103	54	69
No of rovibrational levels	5918	4657	3774	1530	994	861	1558	165	140

In this work, the maximum vibrational quantum number of the ground state of O_2 is 43, which means that for $J = 0$ there are 44 vibrational levels. This differs from the 47 vibrational levels obtained by Lino da Silva et al. [76], because in that work the $X^3\Sigma_g^-$ is calculated standalone, without accounting for other states. While developing this work and plotting the different curves, a crossing between $X^3\Sigma_g^-$ and $a^1\Delta_g$ was observed. Krupenie [59] and Gilmore [33] do not show said crossing. By changing the extrapolation method of the ground level to Extended Rydberg, the curves do not cross, so we chose to keep this extrapolation. This is the reason behind the difference between the two values, since both works use the same updated spectroscopic values from [68]. Either way, the difference is small and both methods present similar results.

Other comparison can be made, this time for the maximum vibrational and rotational quantum numbers of the ground state of N_2. The table of values for the states of this molecule is in appendix B.3 but we recover the values for $X^{\Sigma+}_g$: $v_{max} = 61$, $J_{max} = 217$ (below the dissociation limit) and the number of total rovibrational levels is 9008. Lino da Silva et al. [14] and [15] present different values for this state: $v_{max} = 60$ and $J_{max} = 213$. The difference lays in the fact that those works make use of the Hulburt and Hirschfelder extrapolation method while here it is used the direct potential fit developed by Le Roy et al. [37].

Overall, these values are within the ranges usually observed and the energies levels values together with the plot of potential curves give us confidence in these results.

[1] Degeneracy of a electronic state is $g_e = (2 - \delta_{0,\Lambda})(2S - 1)$, in which S is the total spin quantum number and Λ is the orbital angular momentum projection quantum number, with its value 0, 1, 2, 3, ... corresponding to Σ, Π, Δ, Φ, ... molecular states; meaning that $\delta_{0,\Lambda}$ will be 1 if it is a Σ state and 0 otherwise. $(2s + 1)$ is 1, 2, 3, ... for singlet, doublet, triplet ... states, respectively.

3.3.6 Updated Thermodynamic Properties

Finally, with all the calculated energy levels, the thermodynamic properties may be obtained, through the determination of the partition functions - equations 2.10 to 2.14. This process is repeated for multiple temperature values and the properties are then fitted using the expressions 3.2, 3.3, 3.4 of Gordon and McBride [56]. The coefficients for those equations yield the updated thermodynamic database and the values for each of the 15 species, valid up until 100 000 K, are reported in appendix B.4. These updated thermodynamic databases will be used by the polynomial thermodynamic model of SPARK, to more easily calculate the thermodynamic properties. The alternative would be to use the analytical model, but it is very time consuming and convergence is more difficult to reach, as previously explained.

To compare and validate the results obtained, enthalpy as a function of temperature ($H-H(0)(J/mol)$ vs $T(K)$) was plotted using both the thermodynamic fits developed here and the ones by Gordon and McBride. These last ones are extrapolated for temperatures higher than 20 000 K, by assuming a fixed slope. Additionally, a comparison was drawn with the thermodynamic properties determined by Capitelli et al. [77] [78] (up to 50 000 K), for which the spectroscopic data of [57] was used in simplified versions of equation 2.17 and assumed valid until dissociation.

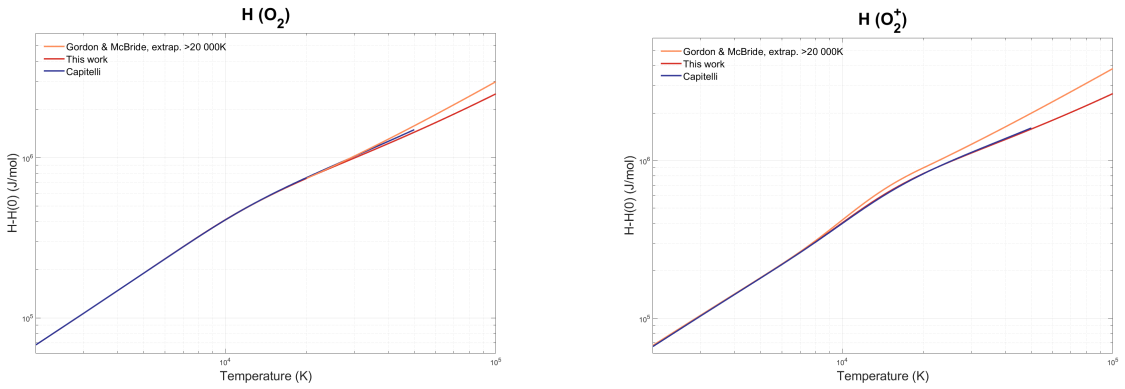

(a) Enthalpy of O_2.

(b) Enthalpy of $O_2{}^+$.

Figure 3.7: Enthalpy vs temperature graphs for O_2 and $O_2{}^+$.

Figures 3.7 (a) and (b) present the results for O_2 and $O_2{}^+$. One may observe that for low temperatures (up to 20 000 K for O_2 and 10 000 K for $O_2{}^+$) the curves for this work and Gordon and McBride are coincident, a good sign that the updated values are correct, as for low temperatures the lower lying energy levels will be the most populated ones and the Gordon and McBride coefficients already considered these energies. For the higher temperatures, the curves diverge, showing the importance of updating the energies, as the simple extrapolations of the default values would lead to different results, overestimating them. The Gordon and McBride values were fitted for fewer energy levels, specially higher lying ones, hence this work's inclusion of more electronic states and better reconstruction of potential curves lead to a better calculation of thermodynamic properties at higher temperatures. These higher lying states will be more populated at those temperatures hence their determination is of great importance.

The curves for $O_2{}^+$ by our work and Gordon and McBride diverge at lower temperatures than for O_2.

This is a result of how, for diatomic ionic species, even for not so high temperatures, the corresponding energy levels have been significantly updated in the last years, compared to those used by Gordon and McBride.

Comparison between the curves of this work and the ones by Capitelli [77] shows similarities in the high-temperature trends, which vindicates the implementation of our new database. The differences in the values for both curves are a result of the different considered states (with this work presenting a more up to date set of states) and the fact that Capitelli uses spectroscopic constants beyond their validity limits.

Figures 3.8 (a) and (b) present the graphs of C_p of the O_2 and O_2^+ species. For the remaining molecular species (N_2, N_2^+, NO, NO^+), their enthalpies and specific heats are presented in appendix B.5.

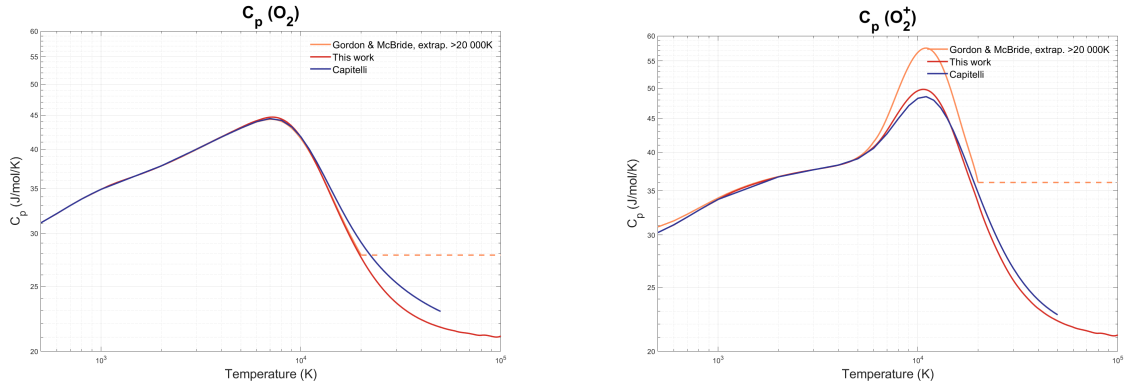

(a) Specific heat of O_2.

(b) Specific heat of O_2^+.

Figure 3.8: C_p vs temperature graphs for O_2 and O_2^+.

For the atoms and their respective ions, the same comparison was made, however other data was additionally included since it was available from the literature: the curves using the coefficients determined by Johnston and Brandis [3] were also plotted. Their work updated the thermodynamic fits for temperatures up to 50 000 K.

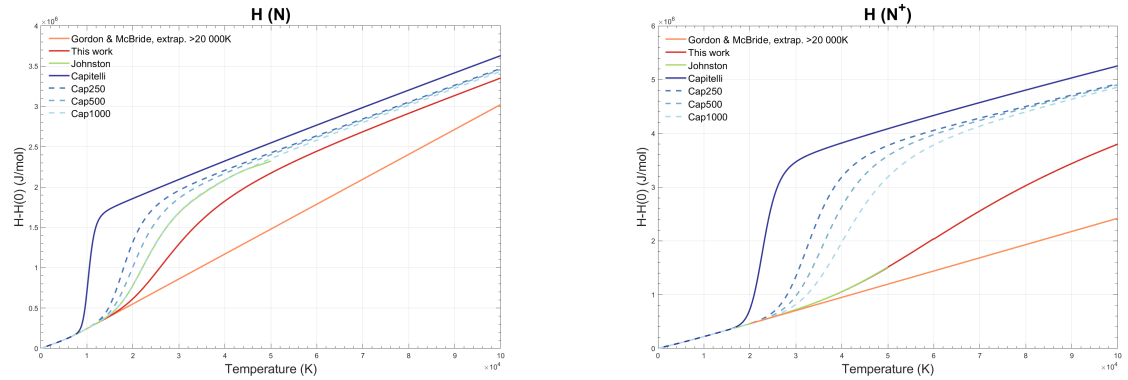

(a) Enthalpy of N.

(b) Enthalpy of N^+.

Figure 3.9: Enthalpy vs temperature graphs for N and N^+.

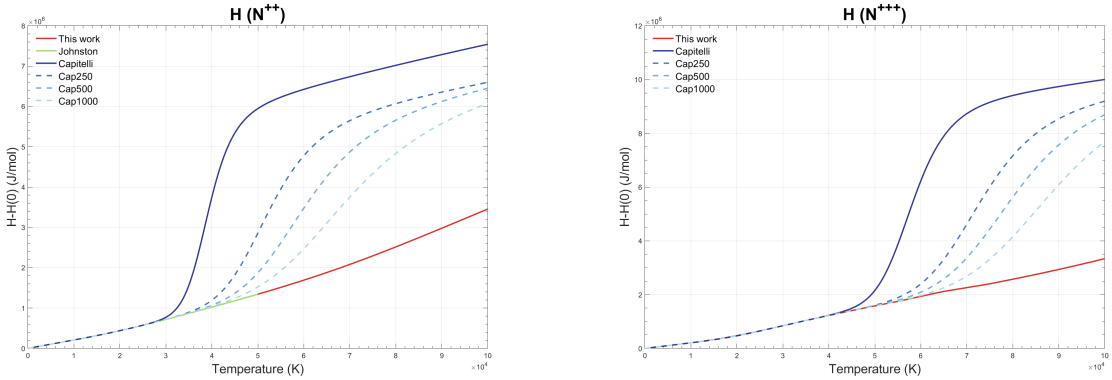

(a) Enthalpy of N^{++}.

(b) Enthalpy of N^{+++}.

Figure 3.10: Enthalpy vs temperature graphs for N^{++} and N^{+++}.

Figures 3.9 and 3.10 show, for N, N^{+}, N^{++} and N^{+++}, the enthalpies calculated in this work (using the energy values compiled in the NIST database), those from Gordon and McBride, those from Johnston and those from Capitelli. For the double ionic species there is no data from Gordon and McBride, while for triple ions only comparisons with Capitelli's values may be drawn. Linear scales are used here to present the results, as atoms will be predominant in the mixture for higher temperatures, so it is our interest to observe those ranges with more detail.

As it was the case for molecules, there is also good agreement between all the curves at lower temperatures. Likewise, for higher temperatures the updated curve differs from the extrapolated old one, for the reasons expounded above.

For the N^{+} and N^{++} ions, our curves are very close to the ones obtained by Johnston. For the double ion, this is an expected result as both works used the same set of NIST energy levels. For N, the energy values by Johnston are different at higher temperatures. This occurs as we only consider the levels from NIST database, whereas Johnston accounts for additional higher-lying levels in his work [79]. Interestingly, for N, the curve by Johnston agrees closely with the curve from Capitelli with ionization potential lowering of 1000 cm^{-1}, where additional Rydberg states are also accounted for.

As for the O curves (see B.5), one may also observe that for higher temperatures, Johnston's plot differs from ours, as it happens for N. Once again, this is due to the different set of levels considered. In this case, it does not agree with any curve of Capitelli. For the O ions, the differences between this work's plots and Johnston's are less marked.

Furthermore, for the sake of compactness, we neglect fine-structure in our treatment of the NIST energy levels, whereas Johnston does not, yielding a different set of energy levels considered. In general, the effect of ignoring the fine-structure of atomic levels is negligible since spin-splitting effects (which cause the fine-structure) lead to very minor shifts in energy. However, in some specific situations, this may lead to some differences at low temperatures; for example the O atom's ground level used in this work, with degeneracy 9, is spin-split into 3 levels in the fine-structure considered by Johnston, with degeneracies of 5, 3 and 1. This leads to considerable differences in the partition function of O at low temperatures and consequently in the thermodynamic properties (see B.5). However, since these low

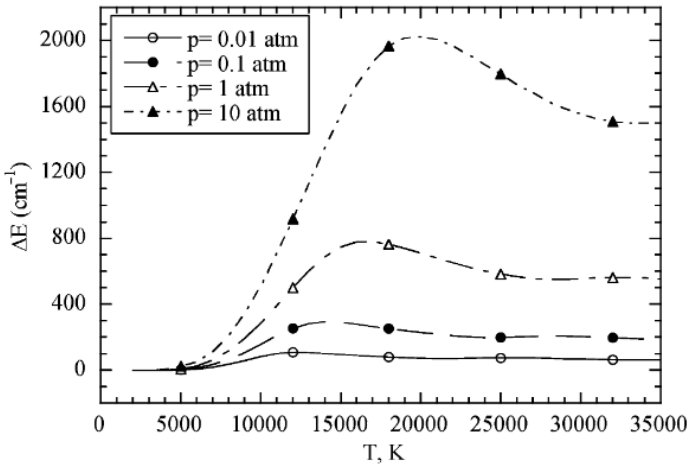

Figure 3.11: Lowering of the ionization potential in air plasmas as a function of temperature at different pressures [78].

temperatures are of no interest in our case of post-shock flows with temperatures higher than 10 000 K, this is not a crucial issue. Future updates of our thermodynamic database may nevertheless account for spin-splitting, in an effort to make it even more widely useful. We may also note that the minor shifts in energy may be significant in radiation studies, thus fine-structure must be considered when studying the effects of radiation.

Additionally, comparisons between our curves and the ones from Capitelli et al. [77] are also carried out in the same figures. Capitelli's polynomial fits differ from those developed in this work in the set of levels inserted in the partition functions, with Capitelli considering many more levels. This was done in an effort to complete the observed levels reported by NIST, for example, with semi-empirical methods to obtain theoretically predicted levels that were not being observed. This is performed using Rydberg and Ritz extrapolation laws and may even add levels above the ionization potential. Although in isolation the addition of these higher lying levels would not impact the partition function, the sum of so many additional resultant levels (and their increasing degeneracies) may lead to nonphysically high and diverging partition function values, also impacting the thermodynamic properties. To solve this problem, the sum 2.11 should be adequately truncated. This was done by considering the hypothesis of ionization potential lowering, in which the levels considered go up to the last energy level that respects $E_n \leq E_i - \Delta E_i$, with E_i being the ionization energy and ΔE_i the ionization potential lowering parameter, determined according to the conditions considered. Therefore, the curves derived from Capitelli's energy levels data and considering potential lowering of 250, 500 and 1000 cm^{-1} are also plotted for comparison. These curves still overestimate the enthalpy values when compared to the fits calculated in this work. Hence, for future updates of the database here developed, some additional Rydberg states may also be accounted for, providing that the adequate ionization potential lowering is chosen. Figure 3.11 presents the lowering of ionization potential one may assume for equilibrium air plasmas, considering different pressure and temperature conditions, that determine the density of charged particles in the gas. For the high temperature considered in this work, as well as ram pressure of 0.1 MPa, the ionization potential lowering should be in the vicinity of 400 cm^{-1} to 800 cm^{-1}.

Figures 3.12 and 3.13 present the graphs of C_p for the N, N^+, N^{++} and N^{+++} species. For the remaining atomic species (O, O^+, O^{++}, O^{+++}), their enthalpies and specific heats are plotted in appendix B.5 .

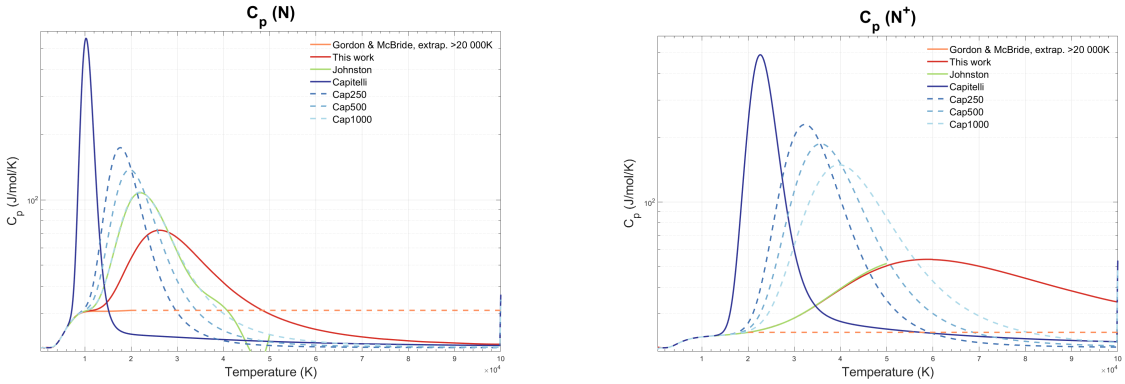

(a) Specific heat of N. (b) Specific heat of N^+.

Figure 3.12: C_p vs temperature graphs for N and N^+.

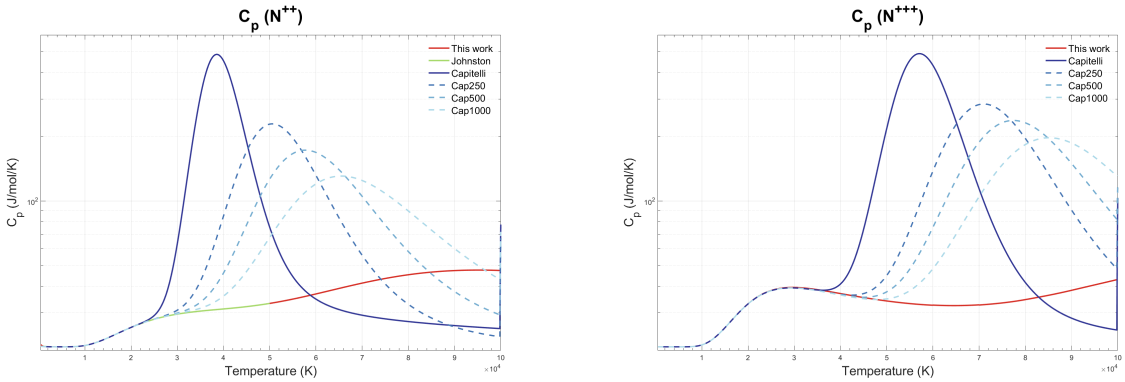

(a) Specific heat of N^{++} (b) Specific heat of N^{+++}

Figure 3.13: C_p vs temperature graphs for N^{++} and N^{+++}.

The impact of the update and extension of the thermodynamic database in the simulations will be addressed later in section 4.2.

Finally, the equilibrium composition for a mixture of the 15 species here considered, at 1 atm, is presented in figures 3.14, using the updated thermodynamic database. The figure using linear scale allows for the evaluation in further detail of the behaviour of the species with largest concentrations, while the logarithmic scale shows the behaviour of all species, with special focus on low temperatures. Dissociation of N_2 is occurring between temperatures of 2 000 K and 10 000 K, while dissociation of O_2 starts at 3 000 K and is concluded after 5 000 K. Ionization of N and O into N^+ and O^+ occurs at around 10 000 K and 12 000 K , followed by second ionization at 14 000 K and 18 000 K and third ionization at 17 000 K and 20 000 K, reaching a plateau of constant concentrations at around 35 000 K and 28 000 K, respectively. In reality higher ionization processes will take place, however our thermal database is capped at third ionization of atoms, so this is not represented. As such, figures 3.14 only represent temperatures up to 50 000 K, as for higher temperatures the equilibrium composition should consider

further ionizations. Appendix B.5 also presents the equilibrium composition for the three gas mixtures (with 11, 13 and 15 species).

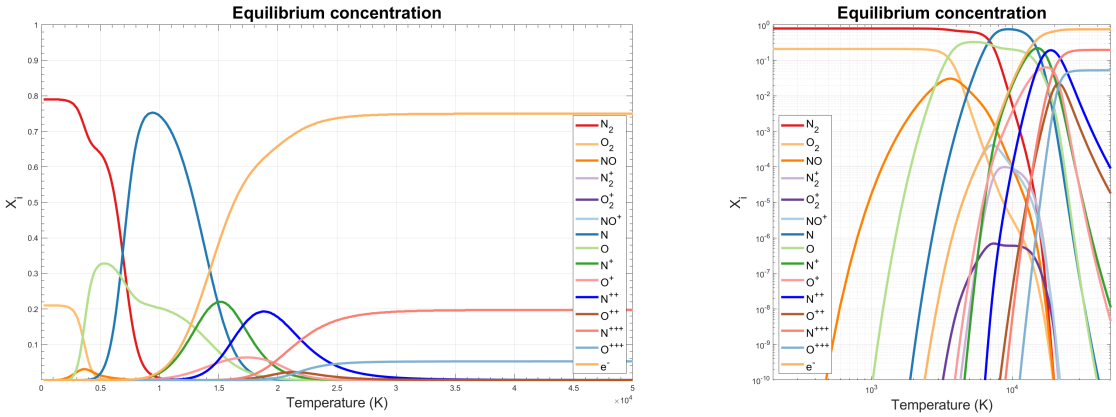

(a) Linear axis.

(b) Logarithmic axis.

Figure 3.14: Equilibrium composition of Earth atmosphere mixture with x_{N_2} = 0.79 and x_{O_2} = 0.21, considering the following species: N_2, O_2, NO, N_2^+, O_2^+, NO^+, N, O, N^+, O^+, N^{++}, O^{++}, N^{+++}, O^{+++}, e^-.

3.4 Chemical Kinetics Modelling

Let's first consider only the 11 species that are usually included in hypersonic simulations in Earth's atmosphere: N_2, O_2, NO, N_2^+, O_2^+, NO^+, N, O, N^+, O^+ and e^-.

Different kinetic schemes may be found in the literature [38, 80, 81]. The reactions used in this work involving these species are presented in B.20, corresponding to the ones used by Johnston and Panesi [38] which include dissociation reactions, neutral exchange, associative ionization, charge exchange reactions and electron-impact ionizations reactions.

For simulations with relatively low temperatures, the predominant endothermic reactions that occur are dissociation and single ionization. When the temperatures reach around 20 000 K, there is already a concentration of electrons in the mixture close to 50%, with N^+ and O^+ molar concentrations of almost 50% as well and only very small concentrations of N and O, as seen in appendix B.5. Further increasing the flowfield's velocity would mean that more energy would be transferred in the shock. Speaking from a simulations' point of view, where only simple ions are being included, the fact that the ionization is capped and practically no more ionization can happen - since the only atomic ions being considered are the result of N and O ionization - means that the extra energy would not be dissipated, yielding an unrealistically high temperature.

In reality, further ionizations will occur, with the simple ions being further ionized into N^{++} and O^{++}, with these reactions using a portion of that extra energy. Therefore, double and even triple ionizations are no longer negligible and need to be accounted for in the simulations, therefore N^{++}, O^{++}, N^{+++} and O^{+++} species also have to be included. Their thermodynamic properties were already presented in the previous section and their transport properties will be discussed in the next one.

The kinetic dataset of Johnston and Panesi [38] is mostly sufficient for moderate hyperbolic entry

flows up to about 14-15 km/s. Nevertheless, since we are striving to reach higher flow velocities, some further analysis needs to be brought in the particular case of atomic ionization processes, which will soon enough be dominant as we reach higher entry velocities and almost immediately dissociate any kind of molecular species, including ions. For single ionization reactions, we have kept the values from Park et al. [82] which are also included in Johnston and Panesi [38] kinetic dataset. For double ionization rates, we consider the ones proposed by Johnston and Brandis [3], which propose a simplified treatment of N^+ and O^+ ionization rates, adding the contribution of excited electronic states using a Drawin ionization model [83] for N^+, and a recombination rate for O^{++} assumed as equal to the one for N^{++}.

For N^{++} and O^{++} ionization, no data is available in the literature, and we consider the well-known ionization cross-sections from Bell et al. [84] (which are also very close to the ones proposed by Voronov [85]) to achieve a first reasonable estimate of the corresponding ionization rates (through the simple integration of a Maxwellian distribution function to these rates). Note that this approach neglects the contribution from higher-lying electronic levels of N^{++} and O^{++} for ionization processes, hence slightly underestimating the ionization rates. A more accurate treatment would entail the calculation of the corresponding quasi-steady rates, with an estimation of the ionization cross-sections for higher-lying levels from the Drawin model, in an approach similar to the one proposed by Park [86] [80] and Lopez et al. [87].

We also note that the Park single ionization rates have an artificial peak around 40 000K, indicating that they are likely being extrapolated beyond their validity range. Although this work still retains these former rates (Park for single ionization and Johnston for double ionization), future developments could consider an ionization dataset entirely based on the Bell ground-state cross-sections, and possibly a treatment of the excited states contribution towards the total dissociation rate. This is left for future developments. Nevertheless, these ionization rates are presented in figure 3.15.

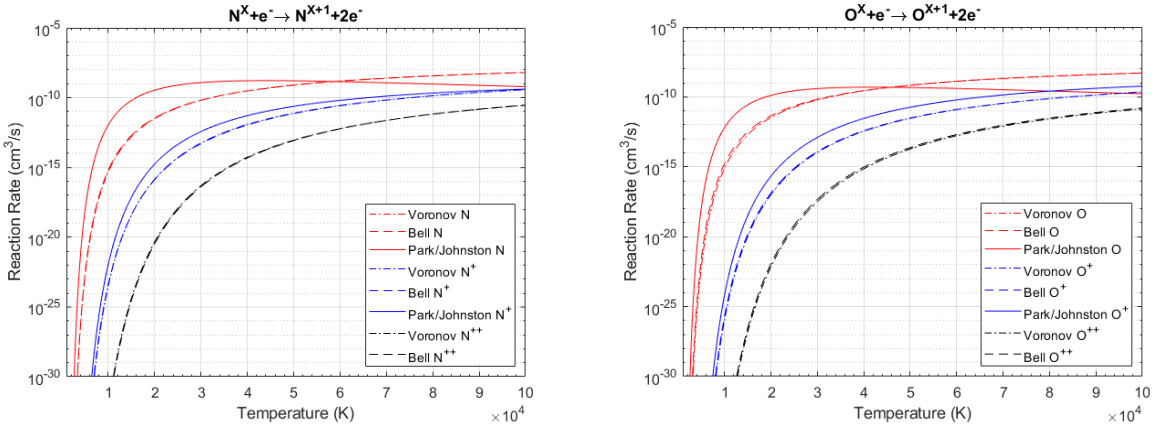

(a) N, N^+, N^{++} ionization rates

(b) O, O^+, O^{++} ionization rates

Figure 3.15: Ionization rates.

The chemical reactions, considered in this work, involving these double and triple ions are presented in table 3.3, with the constants to calculate the forward rates (with units of $m^3 mol^{-1} s^{-1}$) through the

Arrhenius equation 2.32.

Table 3.3: Chemical kinetics for double and triple ionized species.

	Reaction	A	n	$\theta_R(K)$
R1	$N^+ + e^- \rightleftharpoons N^{++} + e^- + e^-$	6.04×10^6	0.603	341 356
R2	$O^+ + e^- \rightleftharpoons O^{++} + e^- + e^-$	6.90×10^8	0.206	405 511
R3	$N^{++} + e^- \rightleftharpoons N^{+++} + e^- + e^-$	5.14×10^6	0.588	550 457
R4	$O^{++} + e^- \rightleftharpoons O^{+++} + e^- + e^-$	2.17×10^9	0.075	635 568

3.5 Transport Modelling

The transport model used in this work is the Gupta-Yos one, since the Wilke/Blottner/Eucken gives inaccurate results for the velocities of interest, considering the high temperatures reached and the non-negligible degrees of ionization. Loureiro [44] compared both models to the exact solution (calculated using a multicomponent Chapman-Enskog method) in regards to viscosity and thermal conductivity, and studied as well the impact of including the corrections of ambipolar diffusion to the mass diffusion terms - concluding for this last topic that it indeed represents an important correction. From there, one may quickly discard the Wilke model as it deviates significantly from the exact solution at temperatures higher than 8 000 K, due to the assumption of equal collision cross-section for all binary interactions. The Gupta-Yos model coincides with the exact solution for the same temperature interval, giving different values of viscosity and thermal conductivity for higher temperatures, however following very similar trends to the exact one. The difference between their values is smaller than the difference between the Wilke model and the exact one, with the Gupta model delivering reasonably good prediction for temperatures higher than 10 000 K. Nevertheless, it is important to note that for ionization degrees such as the ones encountered at temperatures above 18 000 K, specially with the possibility of double and triple ionization, the Gupta model may not be ideal and further corrections should be applied to enhance the model.

To implement the Gupta-Yos model, one needs to determine, for each collision pair, the two collision cross-sections: $\pi\overline{\Omega}_{sl}^{(1,1)}(T)$, called the diffusion collision cross-sections, and the so-called viscosity collision cross-sections, $\pi\overline{\Omega}_{sl}^{(2,2)}(T)$. This will be done by applying the widely used coefficients that define the collision cross-section curve fits determined by Gupta et al. [46] as input data. Loureiro [44] offers more detail on how these data and model are used in the SPARK code, as well as further considerations on its advantages and limitations.

Gupta et al. [46] does not provide information regarding the transport properties for N^{++}, O^{++}, N^{+++} and O^{+++}, therefore these species' transport properties will be assumed equal to the values for N^+ (for N^{++} and N^{+++}) and O^+ (for O^{++} and O^{+++}) [3], as their interactions with the gas species will be, on a first order-basis, of the same nature.

3.6 Computational Mesh

A 50×50 cell spherical mesh is considered for the simulations of this work. This represents a good compromise between computational effort and spatial accuracy, capturing the flow gradients.

Due to the axisymmetric nature of the problem, a 2D axisymmmetric simulation is considered and a symmetry condition is imposed in the lower boundary of the mesh, also corresponding to the stagnation line, where multiple analysis will be made. For the upper boundary supersonic outlet condition is imposed, while the left boundary has the upstream conditions there defined. Finally, in regard to the boundary condition at the wall of the meteoroid, it is common to define the wall as isothermal or adiabatic. An isothermal wall would mean a steep change of temperature in the boundary layer, as the temperature of meteoroid's wall (that depends on the material of the meteoroid but it is usually considered to be within the range of 2000 K and 5000 K [2]) would be much lower than the temperatures in the shock layer. Capturing these large gradients would require refinement near the wall.

However, since wall heat fluxes are not the subject of this study, one will not focus on the behaviour near the wall. Instead, a adiabatic wall boundary condition is applied, so refinement near the wall is not necessary - allowing for faster convergence of simulations and more time to perform various simulations. This can be done, as typically the wall is far enough from the shock wave that it does not influence it. This is evidenced by a plateau of quasi-steady-state properties.

To fully capture the shock properties, the mesh has to be refined in the shock layer, where the gradients are extremely pronounced. This was performed in an external MATLAB routine developed by Coelho [19] and adapted for these cases. It receives as input the original unrefined mesh created in SPARK, the temperature or pressure field determined for the original mesh and a chosen clustering factor. Then the routine searches for a sudden and significant jump in pressure, for example, for each row of cells, identifying the region defined by them as the shock region and clustering the cells around it. Figure 3.16 presents an example of an original mesh used to obtain the pressure field and the corresponding mesh after refinement in the shock wave.

[2] or assumed in Planck radiative equilibrium

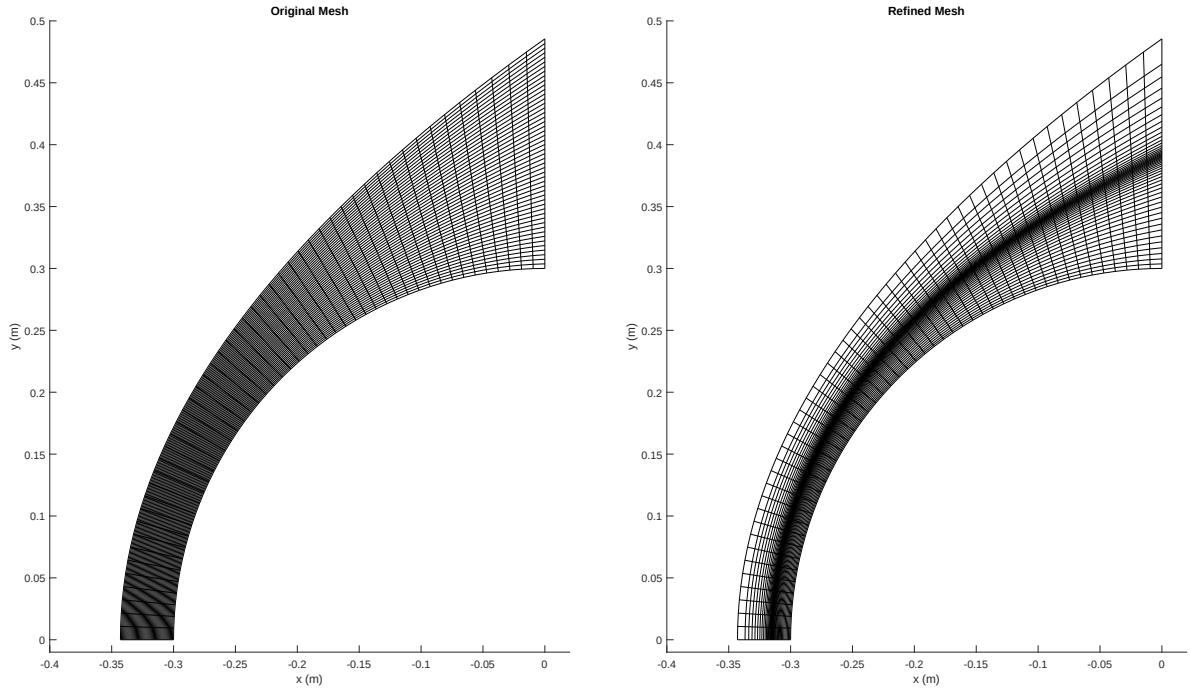

(a) Original mesh.

(b) Refined mesh.

Figure 3.16: Original mesh and refined mesh for a simulation of ram pressure 0.1 MPa, velocity 16 km/s, using the updated thermodynamic database and 13 species.

The final mesh is refined in the shock layer, where smaller cells are required to capture the large gradients. One may observe that closer to the upstream wall the final mesh is coarser, as the flowfield properties there will remain unperturbed and there is no need for smaller cells in that region.

3.7 Simulation Strategy

Some brief considerations should be made regarding the simulation strategy adopted as well as difficulties encountered.

Section 4 will present results and comparisons of the simulations performed using the old and updated thermodynamic databases and using the chemistry models that include 11, 13 and 15 species. The thermodynamic polynomial model was considered for all the presented simulations, although, during the development of this work, simulations using analytical models were attempted, but convergence could not be reached for higher velocities. For all simulation cases, the Gupta-Yos transport model was considered (sometimes from a restart with Wilke to save time) and a single-temperature study performed.

In regards to the numerical solver, implicit time discretization was the strategy with better results in convergence. Although more computationally expensive, this was preferable to explicit time discretization, that required a extremely low CFL to prevent the simulation from crashing and resulted in unrealistic convergence times. No problems worth to mention were encountered using implicit time discretization

(even with refined meshes), with the CFL used to stabilize the numerical scheme typically between 0.001 and 0.1.

Regardless, the higher velocities we are trying to simulate represent a difficulty, with the solver not being able to handle starting conditions that extreme and the residuals increasing to infinity, when the simulation is initialized from zero. A strategy that makes use of the SPARK ability to use previous results of simulations as restart files was then employed. Starting from 8 km/s simulations and gradually increasing velocity (and changing the upstream conditions accordingly) at each simulation, not only allowed for the analysis of more simulations, but also facilitated the convergence of each one of them, by using the previous one. This allows for the detached shock to be stabilized for lower velocities and then subsequent changes in location and properties to be gradually obtained for higher velocities. This restart strategy also proved to be useful for simulations using the refined mesh at the shock, by using the result of the original mesh simulation with those free stream conditions as a restart file to more easily reach convergence.

Chapter 4

Results

Following the deployment of the enhancements described in chapter 3, we may now evaluate the obtained simulation results. This section presents comparisons between results using the different models as well as considerations on their fidelity towards physical reality.

4.1 Simulations Performed

To compare the results using the previous and the updated thermodynamic databases as well as using a mixture composed of 11, 13 or 15 species (with simple, double and triple ionization for the atoms, respectively), various simulations were performed.

Table 4.1 describes the upstream conditions of the most relevant simulations performed, as well as the number of species considered and the corresponding thermodynamic databases (either the Gordon and McBride (GM) database or the updated database of this work). All simulations considered a polynomial thermodynamic model, a single-temperature model and a Gupta-Yos transport model and simulated a meteoroid of radius 0.3 m, unless stated otherwise. The results presented in the following subsections were obtained using a refined mesh in the shock wave region, after a first simulation performed using an unrefined mesh.

An aerothermodynamic analysis for the different simulations is carried out, with special focus on temperature and chemical species concentrations, mainly by evaluating the stagnation line.

Table 4.1: Main simulations performed.

							Thermodynamic Model			
							GM database	Updated database		
		V_∞	h	ρ_∞	T_∞	p_∞	Kinetic Models	Kinetic Models		
		(km/s)	(km)	(g/m^3)	(K)	(Pa)	11	11	13	15
Upstream conditions	constant ram pressure (0.1 MPa)	8	45.0	1.56	260.5	116.9	•	•	•	•
		10	48.4	1.00	260.2	75.2	•	•	•	•
		12	51.4	0.69	256.3	51.3	•	•	•	•
		14	53.9	0.51	251.5	36.9		•	•	•
		16	56.0	0.39	246.8	27.7		•	•	•
		18	57.8	0.31	242.8	21.5		•	•	•
		20	59.4	0.25	239.3	17.3		•	•	•
		22	60.9	0.21	236.2	14.0		•	•	•
		24	62.2	0.17	233.7	11.7		•	•	•
		25	62.8	0.16	232.5	10.7			•	•

4.2 Thermodynamic Database Influence

In this section the influence of the enhancement made on the thermodynamic properties database will be studied. The database used at first was the Gordon and McBride database [56] (NASA9 database) and does not include double and triple ions, so, although the updated one has information regarding those species, to directly compare results between databases, we will only make use of 11 air species: N_2, O_2, NO, N_2^+, O_2^+, NO^+, N, O, N^+, O^+, e^-.

For starters, we evaluated the result of a simulation with 12 km/s, for which it's not expected to surpass the 20 000 K mark of temperature in the shock and the thermodynamic properties calculated using the Gordon and McBride database versus using the updated database developed in this work will not differ significantly as seen in section 3.3.6. Consequently, this will not impact the overall behaviour of the temperature and chemical species mole fractions in the stagnation line, as observed in figure 4.1. We observe a small difference in the peak temperature reached in the stagnation line of less than 1000 K, with the one using the old database reaching the highest temperature of 18 180 K, approximately. The difference is due to small differences in the refinement process for each simulation. Nevertheless, the results are very similar, which confirms the validity of the new updated database for temperatures lower than 20 000 K and is in conformity with what was expected.

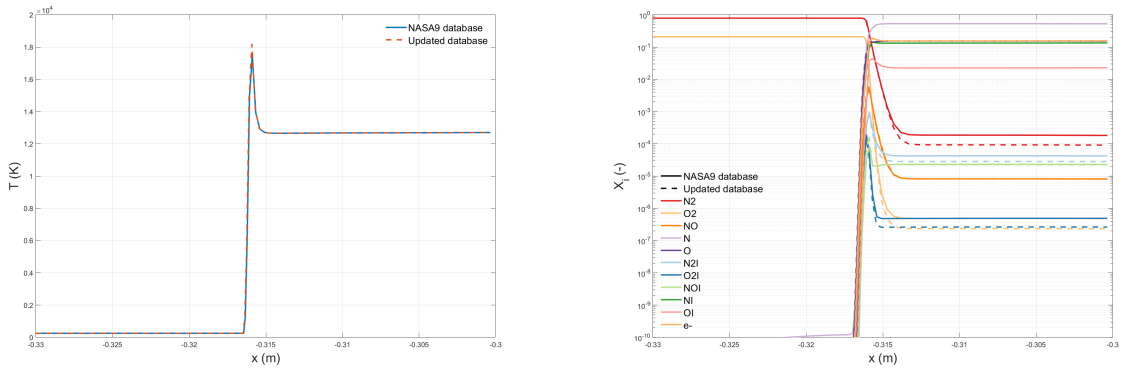

(a) Stagnation line temperatures for simulations using the Gordon and McBride (NASA9) database vs the updated database.

(b) Chemical species mole fractions at stagnation line for simulations using the Gordon and McBride (NASA9) database vs the updated database.

Figure 4.1: Comparison of simulations using Gordon and McBride (NASA9) vs updated database at stagnation line, for simulations of 12 km/s.

Let's take the opportunity to also evaluate the usual behaviours in chemical species mole fractions for these velocities: one may observe that, as it was defined, upstream of the shock wave, N_2 is at 79% and O_2 is at 21%, decreasing rapidly in the shock. Those molecules will mainly dissociate into N and O atoms, but also ionize into N_2^+, O_2^+, before these dissociate as well. Additionally, recombination creates very low concentrations of NO and NO^+, followed by dissociation. In the temperature graph presented here, the temperature remains constant from approximately x=-0.313 m up until the adiabatic wall at x=-0.3 m (considering a meteoroid radius of 0.3m whose center is x=0). This is due to equilibration of fast source and sink terms for the chemistry, reaching a quasi-steady-state[1]. In this plateau one may also evaluate the ionization degree for the 12 km/s velocity and observe that the free electron concentration is 15% approximately. Before the shock, although not pictured here since the maximum concentration is still lower than 1×10^{-10}, the concentrations of some species may increase slightly as a result of mass diffusion that is not limited by the shock layer.

The rapid dissociation at the shock will impact the temperature and is the main cause of the decrease in temperature right after the shock wave, using part of the energy that, upstream of the shock, is in the form of kinetic energy. This temperature decrease at the stagnation line is seen in figure 4.1 (a), for both simulations.

The main advantage of the extension of the thermodynamic database performed in this work is found at the point where graph comparisons between databases stop being possible - when simulations using the Gordon and McBride database stop converging and the conditions cannot be accurately simulated. This is because the enhancement performed in the thermodynamic models allows for the convergence of simulations with associated temperatures of 20 000 K or higher, something which otherwise could not be done while using the Gordon and McBride database. This was confirmed during the simulation process, when the convergence of simulations with velocities of 14 km/s or higher could not be reached

[1] This is different from chemical equilibrium, which is only reached after slower chemical processes equilibrate at longer time scales

with the Gordon and McBride database. On the other hand, simulations with those velocities converged, with no issues, when using the updated and extended database, presenting itself as, in fact, a crucial enhancement to simulate higher velocity bodies entering the Earth's atmosphere.

It is expected that, if the results using the Gordon and McBride database could be obtained for temperatures higher than 20 000 K, those results and the ones using the new database would differ significantly, as the thermodynamic properties determined by each of these fits distance themselves for those temperatures (as seen in section 3.3.6).

Figure 4.2 (a) shows the temperatures in the stagnation line for a simulation of 16 km/s, for which the maximum temperature is approximately 23 680 K, higher than 20 000 K, while quasi-steady-state is reached for a temperature of 15 550 K. As for the simulation of 12 km/s, the maximum temperature at the shock is 17 480 K and quasi-steady-state is reached at 12 670 K, approximately.

As expected, the temperatures reached for the 16 km/s are higher. Moreover, the shock is closer to the wall, which also is in concordance with the theory that, in general, higher velocities will translate to lower detachment shock distances [4].

For the 16 km/s simulation, since the velocity is higher, the energy associated to the shock will be higher than for 12 km/s and a part of it will be transferred to gas internal energy through chemical reactions, so naturally it translates in higher degrees of dissociation and ionization (with the concentration of electrons increasing from 15% to 38% approximately), which is observed in figure 4.2 (b). These behaviours correspond to what is expected, which also points to correct implementation of the model.

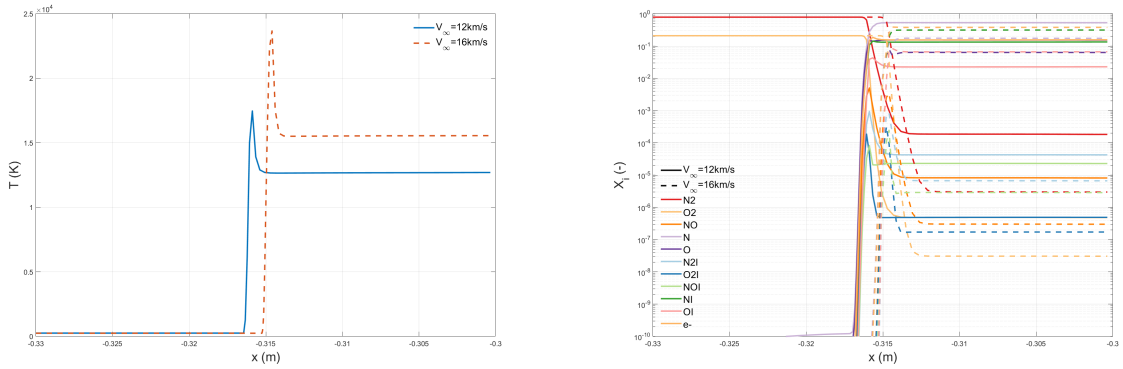

(a) Temperatures at the stagnation line for simulations of 12 km/s vs 16 km/s, using the updated database.

(b) Chemical species mole fractions at the stagnation line for simulations of 12 km/s vs 16 km/s, using the updated database.

Figure 4.2: Comparison of simulations of 12 km/s vs 16 km/s at stagnation line, both using the updated thermodynamic database.

Moreover, a study regarding the impact of updating all species instead of only the atomic ones was performed. The difference in the stagnation line plots is small, as only a few cells in the shock have molecular species at high temperatures before they dissociate rapidly. Nevertheless, the effect of updating the molecules as well is felt in regards to the stability of the numerical model, with the simulations with all species updated converging faster than the simulations with only atomic species updated. Therefore, the update of diatomic species not only contributes to a more complete and useful

database for any applications, but it also is advantageous for high temperature hypersonic entry flow simulations, contributing to their convergence and more accurate results in the cells of the shock where high temperatures and molecular species coexist.

One can then conclude that the use of updated thermodynamic database, although it does not represent a relevant change for temperatures lower than 20 000 K, is essential for simulations that reach higher temperatures. Additionally, for up to 20 000 K, it has the same computational cost as the model that uses the Gordon and McBride database and may be used without disadvantages, therefore the updated thermodynamic properties determined in this work will be considered for all the simulations presented next.

4.3 Transport Model Influence

Although this is not the focus of this work, a quick remark should be made here regarding the transport model used. Loureiro [44] studied this impact and concluded that, concerning the temperature and concentration fractions in the stagnation line, the impact of transport models Wilke vs Gupta-Yos was negligible for low ionization levels such as encountered in this work for simulations with 8 km/s, for example. This was observed by comparing the simulations using each transport model and an upstream velocity of 8 km/s, in figure 4.3 (a).

Nevertheless, even for low velocities, from an accuracy standpoint, it is preferable to use the Gupta model, that makes use of fewer approximations, being closer to the exact solution.

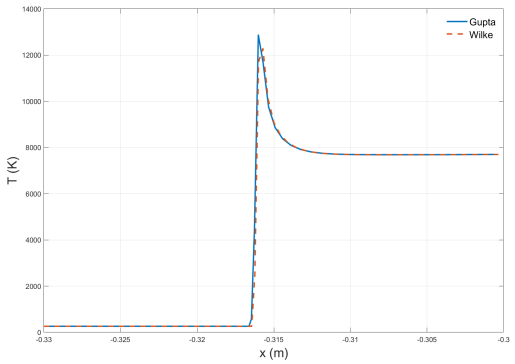

(a) Stagnation line temperatures for simulations of 8 km/s using Gupta vs Wilke transport models.

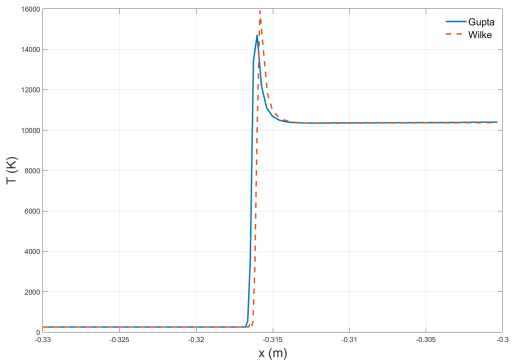

(b) Stagnation line temperatures for simulations of 10 km/s using Gupta vs Wilke transport models.

Figure 4.3: Comparison of stagnation line temperatures for simulations using Gupta-Yos and Wilke transport models. All simulations use the updated thermodynamic database.

For a velocity of 10 km/s the difference in the stagnation line plots resultant from the different transport models is already noticeable in figure 4.3 (b). At this velocity, temperatures of 14 000 K are exceeded, the molar concentration of electrons is at 3% and the transport properties calculated from each model have larger differences, with the Gupta transport model being closer to the exact ones and being the one that should be preferred [44].

For velocities of 12 km/s or higher, the use of Wilke transport model makes it impossible to reach

convergence in due time (with the simulation crashing for CFL's higher than 0.0001), so although in theory this is would be a more cost-effective model, this is only true for lower temperatures; using the Wilke model beyond the conditions where it is valid results in unfeasible convergence times.

These observations made during the simulations process and analysis confirm that the Gupta-Yos model is preferable to the Wilke one for the velocities studied here. Nevertheless it is not forgotten that the Gupta-Yos model is not ideal for the higher ionization degrees and a transport model that calculates transport properties with fewer approximations should be employed for better results at those conditions. This will not be further addressed in this work, as the Gupta-Yos seems to at least be numerically stable for these flight regimes.

4.4 Kinetic Chemistry Model Influence

Now that the use of the updated thermodynamic database allows for higher velocity simulations, one may study the need for inclusion of further ionizations and its impact.

In this section several results are compared. The fact that the maximum concentration of NO, N_2^+, O_2^+ and NO^+ will remain under approximately 1×10^{-2} for all the conditions here considered and their concentrations in quasi-steady-state will remain below 1×10^{-4}, besides the fact that their behaviour tendencies remain similar to those presented in the graphs section 4.2, allow for the omission of these species molar fractions in the graphs. This facilitates the interpretation of the results and the focus on the concentrations that change significantly and will impact the temperature.

For velocities up to 18 km/s, and for a meteoroid of 0.3 m radius, with constant ram pressure of 0.1 MPa and considering a gas mixture that allows for only first ionization, it is possible to observe that the maximum molar concentration of electrons is 46%, a value obtained for the simulation of 18 km/s. This means that first ionization is yet not capped and the inclusion of double and triple ionization would not have a relevant impact in the results. This may be observed in figure 4.4, with the plots using 11 species (N_2, O_2, NO, N_2^+, O_2^+, NO^+, N, O, N^+, O^+, e^-), 13 (the 11 previously mentioned plus N^{++} and O^{++}) and 15 species (includes N^{+++} and O^{+++}) presenting almost coincident results. The maximum temperature at the shock for these conditions is 26 750 K, the temperature reached at the plateau is 17 620 K and we have the following molar fractions at the wall for the newly added species N^{++}, O^{++}, N^{+++}, O^{+++}: 6×10^{-4}, 1.5×10^{-5}, 5×10^{-13}, 2×10^{-15}. The concentration plots for these two last species are not presented in figure 4.4 (b) as the concentrations are too low.

This behaviour is also verified in figure 4.5 where for velocities of 14 km/s and 16 km/s, the plots using the new thermodynamic database with 11 species and 13 species are compared (the 15 species case is not presented in the figure to facilitate interpretation, but it does coincide with the other two, as it does for 18 km/s). The maximum temperatures reached in the shock layer for these velocities are 19 170 K and 23 680 K, respectively, while the temperatures where quasi-steady-state is reached are 14 130 K and 15 550 K. This shows that the temperatures in the shock layer increase with velocity, as the energy involved is greater. This energy is not transformed into thermal energy in its entirety, as previously stated, and, in fact, the higher the energy, not only are the post-shock temperatures higher

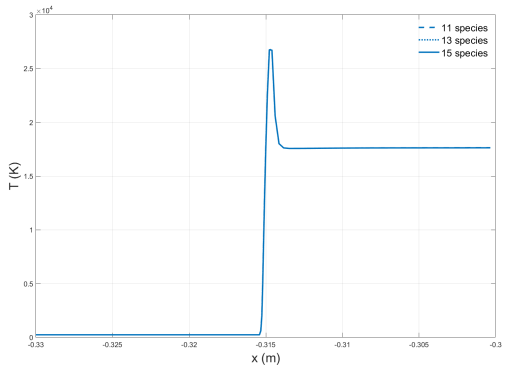

(a) Stagnation line temperatures for simulations of 18 km/s, using the updated database, with 11 vs 13 vs 15 species.

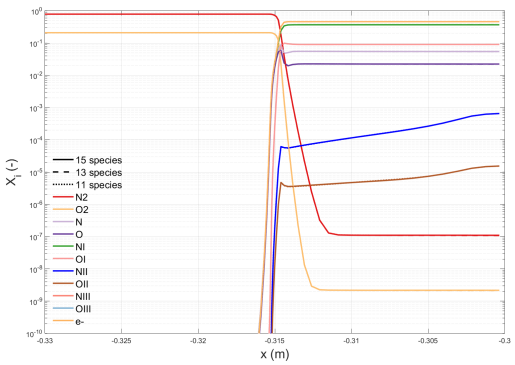

(b) Chemical species mole fractions at the stagnation line for simulations of 18 km/s, using the updated database, with 11 vs 13 vs 15 species.

Figure 4.4: Comparison of stagnation line results of simulations of 18 km/s, using the updated thermodynamic database, with 11 vs 13 vs 15 species.

but also the dissociation and ionization degrees in the shock layer. Ionization degrees may be evaluated through the concentration of electrons that are 28% and 38% for 14 km/s and 16 km/s, respectively. Naturally, the concentrations of N^+ and O^+ also increase.

Comparing the plots using 11 and 13 species, one concludes that, for these range of velocities, the inclusion of double ionization is not essential, with both plots being coincident. The energies involved are not sufficient for full first ionization, therefore the double ions concentrations remain low (maximum of 5×10^{-5} for N^{++} for 16 km/s) and their impact on the resulting temperatures is negligible.

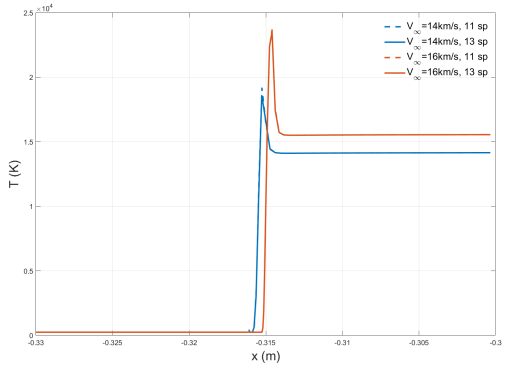

(a) Stagnation line temperatures of simulations 14 km/s and 16 km/s, with 11 vs 13 species.

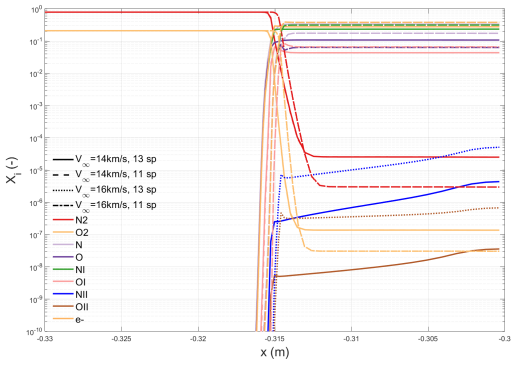

(b) Chemical species mole fractions at the stagnation line of simulations 14 km/s and 16 km/s, with 11 vs 13 species.

Figure 4.5: Comparison of stagnation line results of 14 km/s and 16 km/s, using the updated thermodynamic database, with 11 vs 13 species.

However, as velocity increases, so do the energies involved and more and more ionization occurs. For a velocity of 20 km/s or higher, one may observe that, with 11 species in the mixture, ionization is capped: the concentration of electrons is approximately 50% and the concentrations of remaining N and O are negligible, hence no extra energy may be transferred to the gas internal energy through further ionizations. This cap will lead to unrealistically high temperatures in the shock layer for higher velocity

flows, as the extra energy of the shock wave will be transferred to translational temperatures higher than those encountered in simulations that consider the possibility of ionizing once again the N^+ and O^+.

In reality, the second ionization will occur and the corresponding temperatures reached for each velocity case are lower. When 13 species are considered (N_2, O_2, NO, N_2^+, O_2^+, NO^+, N, O, N^+, O^+, N^{++}, O^{++} and e^-), then the endothermic reactions of ionizing N^+ and O^+ into N^{++} and O^{++} represent another energy loss term that will decrease the temperatures in the shock layer compared to those of the 11 species simulations. Double ionization then needs to be accounted for.

In figures 4.6, 4.7 and 4.8, one may observe the difference in the results for a gas mixture considering 11 species versus a gas mixture with 13 species that includes N^{++} and O^{++} and a gas mixture with 15 species that additionally includes N^{+++} and O^{+++}.

For 20 km/s, the electron molar concentration is 49.9% when only first ionizations are permitted, which leads to a maximum temperature of 32 620 K and a temperature of 24 510 K when quasi-steady-state is reached. Double ionization increases the electron concentration to 51% at the wall and decreases the maximum temperature to 31 920 K. It is noteworthy that, contrarily to what was verified until this point, at 20 km/s, for a ram pressure of 0.1 MPa and considering double ionization, quasi-steady-state is not reached after the shock and there is no plateau of constant properties, with the temperature decreasing to 22 470 K at the wall, as the molar concentration of N^{++} increases up to 3%.

Additionally, the shock distance is smaller for the case of 13 species: since the conditions upstream of the shock are the same for both simulations, the pressure after the shock should be the same. So, since the temperatures are lower for the 13 species case, then density needs to be greater and the shock moves closer to the wall.

Similar trends are found for the 22 km/s simulations. Here, the inclusion of the double ionization decreases the maximum temperature from 40 840 K with 11 species to 39 470 K with 13, as the concentration of electrons changes from the capped value of 49.9% to 57%. For this case, the difference after the shock is more pronounced, with the temperature after the shock decreasing to 24 640 K at the wall, while it was approximately 36 290 K when ionization was capped. This presents an important result, as one may observe that, in fact, the exclusion of relevant processes such as double ionization at this velocity, will significantly over-predict the temperatures in the shock layer, whilst the consideration of said processes will add important energy loss terms that approximate the results to what is expected to happen in reality.

For 22 km/s the maximum concentration of N^{++} is 14% at the wall. The concentration of N^+ decreases as said species ionizes into N^{++} and its concentration increases. O^+ and O^{++} present similar behaviour. Once again, the inclusion of further ionization and the decreased temperatures result in a smaller shock standoff distance.

For the simulation of 24 km/s the concentration of electrons is 62% for the 13 species case, whilst the concentration in the 11 species case remains at 49.9%, as one already knows. The inclusion of N^{++} and O^{++} - whose concentrations at the wall are 21% and 3%, respectively - decrease the post-shock maximum temperature from 48 810 K to 46 690 K, decrease the adiabatic wall temperature from 43 450 K to 26 620 K and bring the shock closer to the wall as a result of higher density to keep equal pressure

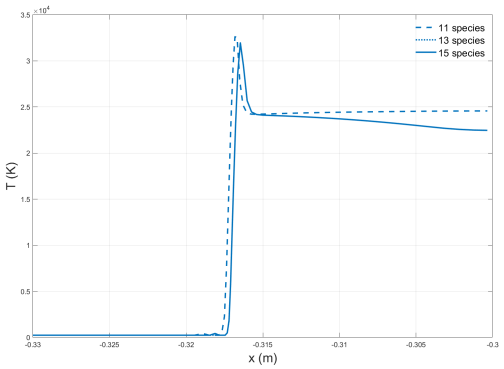

(a) Stagnation line temperatures for simulations of 20 km/s, with 11 vs 13 vs 15 species.

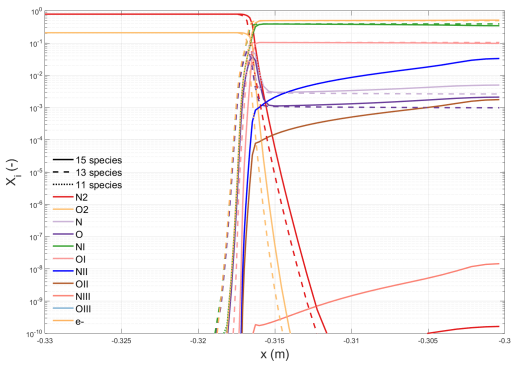

(b) Chemical species mole fractions at the stagnation line for simulations of 20 km/s, with 11 vs 13 vs 15 species.

Figure 4.6: Comparison of stagnation line results of simulations using 11 vs 13 vs 15 species, for a velocity of 20 km/s and using the updated thermodynamic database.

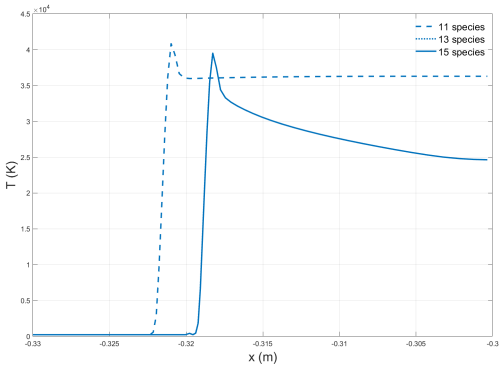

(a) Stagnation line temperatures for simulations of 22 km/s, with 11 vs 13 vs 15 species.

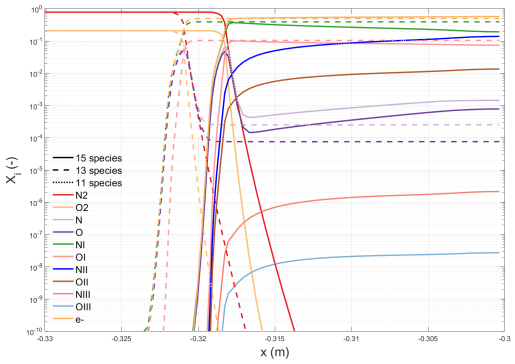

(b) Chemical species mole fractions at the stagnation line for simulations of 22 km/s, with 11 vs 13 vs 15 species.

Figure 4.7: Comparison of stagnation line results of simulations using 11 vs 13 vs 15 species, for a velocity of 22 km/s and using the updated thermodynamic database.

in both cases.

Although double ionization is not capped at 24 km/s, simulations with 15 species (with the newly added N^{+++} and O^{+++}) are also included in the figures 4.6, 4.7 and 4.8, so comparisons may be drawn between the three gas mixtures. The inclusion of third ionization does not impact the temperature at the stagnation line for any of these conditions, with the plot of the 15 species gas mixture coinciding with 13 species one - an expected result as this was also the case for inclusion of second ionization before simple ionization was capped. Therefore, the resultant temperatures and concentrations for the 15 species simulations are the same as the previously reported for 13 species gas mixture; nevertheless, this inclusion of further ionizations increases simulation fidelity. For the 24 km/s the molar fraction of N^{+++} and O^{+++} are at approximately 2×10^{-5} and 6×10^{-7}, respectively, concentrations that might be neglected with practically no consequences to the results.

Simulations using a refined mesh, the new thermodynamic database and 15 species were performed until 25 km/s, where the maximum temperature is 49 200 K, then decreasing until 27 950 K at the wall, with a maximum molar concentration of electrons of 64%. For 25 km/s, the molar fraction of N^{+++} and

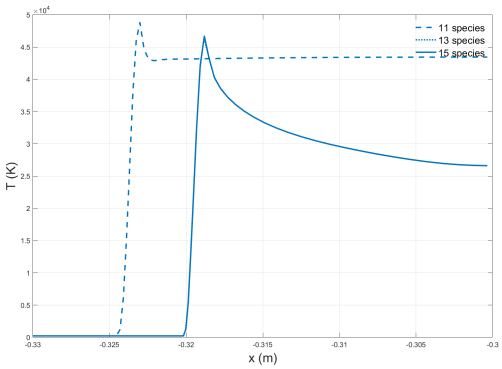

(a) Stagnation line temperatures for simulations of 24 km/s, with 11 vs 13 vs 15 species.

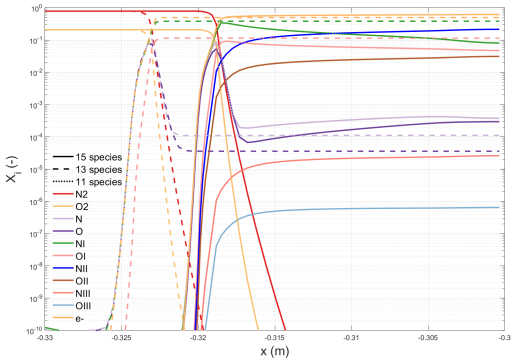

(b) Chemical species mole fractions at the stagnation line for simulations of 24 km/s, with 11 vs 13 vs 15 species.

Figure 4.8: Comparison of stagnation line results of simulations using 11 vs 13 vs 15 species, for a velocity of 24 km/s and using the updated thermodynamic database.

O^{+++} is approximately 7×10^{-5} and 2×10^{-6}. The stagnation line results are presented in figure 4.9 and figure 4.10 represents the 2D plot of the temperature field. For this velocity, convergence could not be reached in due time for a simulation with 11 species, due to the steep gradients in properties.

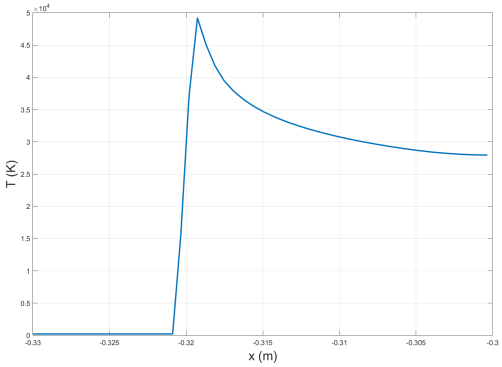

(a) Stagnation line temperatures for simulations of 25 km/s, with 15 species.

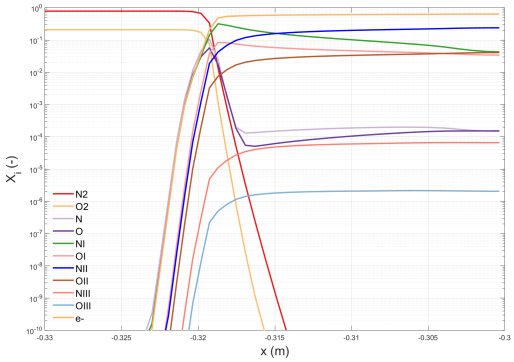

(b) Chemical species mole fractions at the stagnation line for simulations of 25 km/s, with 15 species.

Figure 4.9: Stagnation line results of simulation with 15 species, for a velocity of 25 km/s and using the updated thermodynamic database.

For higher velocities, the presence of N^{+++} and O^{+++} would impact the results as the ionization of N^{++} and O^{++} would represent an important energy loss term for those conditions. This is expected to be more evident for conditions of capped double ionization - when the electron concentration would reach approximately 66% and, with a gas mixture of only 13 species, no further ionizations are available so extra energy involved on the shock would translate into nonphysical higher temperatures. The possibility of third ionization would solve the problem and represent reality with higher fidelity, as one expects these reactions to use a part of the extra energy and, therefore, the temperatures in the shock layer to be lower. Unfortunately, due to restrictions in time, it was not possible to reach convergence for these extreme conditions, a problem arising from the large encountered gradients.

From the analysis here performed, one concludes that for temperatures lower than 18 km/s, the

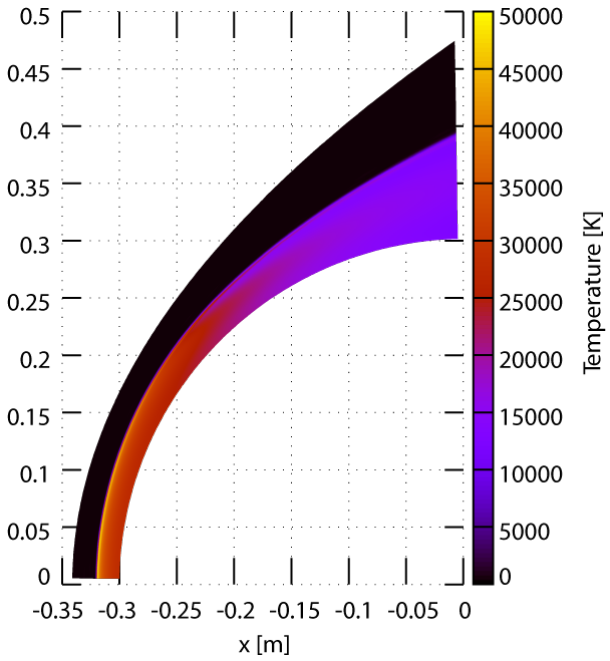

Figure 4.10: 2D temperature field of simulation with 15 species, for a velocity of 25 km/s and using the updated thermodynamic database.

chemical model used (with 11, 13 ou 15 species) does not impact the results. For higher velocities, the inclusion of double ionization is necessary to model the flowfield, with the results presenting important differences and lower temperatures. For velocities up to 25 km/s the inclusion of triple ionization does not impact the temperatures nor concentrations significantly. However, for higher temperatures reached, it is expected to make a difference and for third ionization to be a relevant energy loss term that needs to be accounted for. The availability of data for such processes acts here as a safeguard in case higher velocity simulations are attempted, ensuring that ionization processes are not capped for neighbouring higher velocities.

Convergence times for these simulations do not present large differences due to the model used, specially considering the possibility of restarting simulations using other's results. Hence, although not being crucial for the ranges here simulated, the use of 15 species is recommended, since it increases the simulations' fidelity. Either way, whether or not the triple ionization is included, the addition of N^{++} and O^{++} in the gas mixture is necessary for the more accurate representation of flowfields at the ranges of velocities studied here, with the 11 species mixture overestimating the temperatures at the shock layer significantly.

Therefore, the inclusion of N^{++}, O^{++}, N^{+++} and O^{+++} represents, indeed, an important enhancement.

Chapter 5

Conclusions

5.1 Achievements

The major achievement of this work is the simulation of entry velocity flows in Earth's atmosphere never previously reached using the SPARK CFD code. Without the enhancements performed and implemented in this work, accurate and coherent aerothermodynamic simulations using this code were limited to velocities below 14 km/s (for a ram pressure of 0.1 MPa), a boundary determined by the limit of the thermodynamic properties fitted by the models used - 20 000 K. The update and extension of the thermodynamic database for all the species considered in this work allowed for simulations with higher temperatures, an essential step for simulating higher velocity entry flows.

During the determination and update of thermodynamic properties for larger ranges of temperature, other important achievements were accomplished. We compiled and updated a thorough spectroscopic database for the molecules and respective ions considered in this thesis. This database entails information carefully curated from more than 30 references, so it is our hope that this will represent a valuable and helpful source for studies in any area that rely on spectroscopy, and that its usefulness may prevail in time. Following this, the reconstruction of the potential energy curves is also an important deliverable of this work. Future studies may use these curves and the resultant quantum energy levels to achieve results or as a comparison, with our potential curves being analysed in this work and the phenomena behind them explained, as well as the difficulties encountered (such as undisclosed validity ranges and avoided crossing phenomena) and the methods use to deal with them. With the energy levels determined and compared to other works, the results were deemed satisfactory and were used for partition function calculations.

Furthermore, the thermodynamic database that fits the thermodynamic properties here determined also represents an useful resource for studies to come. Comparison with literature confirmed the accurate determination of the properties through the calculation of energy levels and also allowed us to conclude that the use of these energy levels plus some other Rydberg levels for the atomic species will lead to even better results.

With the thermodynamic properties determined for higher temperatures, velocities higher than 14

km/s are now possible to simulate. For higher velocities the problem of capped ionization for a mixture including only simple ionization arises. Capped ionization conditions encountered at 20 km/s would lead to inaccurately high temperatures in the shock layer when only simple ionization was being accounted for. To solve this problem, N^{++}, O^{++}, N^{+++} and O^{+++} were included in the gas mixture, with their formation in kinetic chemistry reactions being a result of electron impact ionization. The inclusion of double ionization decreased the temperatures found in the shock layer and allowed for simulations up to 25 km/s for a ram pressure of 0.1 MPa, which represents an important extension for velocities one could simulate with SPARK. For these ranges, double ionization was still not capped and the inclusion of triple ionization does not impact the flowfield significantly. While it was not possible in this work to reach convergence in a timely manner for higher velocities, the fact that triple ionization is already included in the models will facilitate the work of others to come that wish to continue simulating higher and higher velocities.

Although this work does not deal with radiation, which would be an essential energy loss term for the temperature regimes encountered here, the dissociation and ionization reactions here simulated already provide important results. Dissociation is an already well studied energy loss term, with the temperature after the shock wave decreasing even for lower velocities such as 8 km/s. The inclusion of ionization is another endothermic reaction whose impact is felt on the flowfield properties. For 24 km/s, when double ionization was included we observed a reduction of maximum temperature at the shock from 48 810 K to 46 690 K (4.3%) and a decrease of temperature at the wall from 43 450 K to 26 620 K (39%), and verified that for velocities lower than 18 km/s, the inclusion of these ions did not impact the flowfield significantly.

These observations support the statement that increasing velocity will activate increasingly important energy loss terms, and the exclusion of these phenomena in the simulations will over-predict the temperatures reached in the shock layer.

Although we are still far away from confirming the hypothesis of a temperature ceiling for high-temperature hypersonic flows, specially since this work did not include the effects of radiation, this thesis puts us a step closer to answering the question posed of what happens in the limiting regimes, by including more energy losses than before and by allowing simulating velocities higher than 14 km/s.

With the enhancements performed in this work, more models are available and tested in the SPARK CFD code, hence more extreme hypersonic high temperature conditions of meteoroids (and other bodies) entering the Earth's atmosphere may be simulated, furthering our understanding of hypersonic high-temperature flows and paving the way for these velocities to be considered for future Space missions.

5.2 Future Work

With hypersonic high-temperature aerothermodynamics and meteoroid science being such polyvalent areas, there will always be room for improvement and further analysis. In here we mention some of the work that we deem as more important for the near future.

Considering the high levels of ionization encountered for the studied velocity range, the transport

properties determined using the Gupta model may distance themselves from the exact ones. Developing a model that is more accurate for higher ionization degrees while not increasing the computational costs too much would be an important improvement.

Further studies regarding the rates of electron-impact ionization reactions added in this work could also be performed, since the determined triple ionization rates developed here only consider the ground state of ionizing species. Approaches like the one discussed by Park [86] should be implemented (see for example Lopez et al. [87]).

Future works could also include multi-temperature models adequate for these conditions. Regarding the thermodynamic properties, fine-structure may be added to the set of levels considered for atomic species, adding more precision to the models. Comparison with values from literature indicates that the addition of some theoretical Rydberg levels may also lead to more accurate results, therefore this study should be furthered and the inclusion of ionization potential lowering will represent an important feature.

For the velocity range studied here , we are in a radiation dominated regime, and as such the inclusion of radiation phenomena is the most important improvement that must be performed, although this might be computationally expensive. This could be done firstly in a loosely-coupled approach, by adding a radiative source term in the SPARK CFD code, and by updating that term once every few iterations, using the radiative field resultant from the converged flow and analyzed with the SPARK Line-by-line code. As radiation effects increase, the impact of coupling becomes more important and ideally the simulation would be done in a completely coupled way, with each iteration involving CFD and radiative computations. The expected impact of coupled radiation is a decrease in shock layer temperatures [3], which would result in decreased shock standoff distance and consequently a decreased radiative heat flux, as the energy is radiating out of the shock layer and decreasing the total enthalpy. This resultant decrease in temperature is expected to be more and more important for higher velocity conditions and simulating this energy loss term is necessary to answer the question of what happens in the limiting regimes and if there will be a ceiling of temperature as hypothesized.

Finally, more simulations using the models here developed should be performed, studying different conditions and, of course, further increasing the simulated velocities.

Bibliography

[1] A. Moorhead, B. Cooke, R. Blaauw, D. Moser, and S. Ehlert. A Meteoroid Handbook for Aerospace Engineers and Managers. Technical report, 2019.

[2] E. A. Silber, M. Boslough, W. K. Hocking, M. Gritsevich, and R. W. Whitaker. Physics of Meteor Generated Shock Waves in the Earth's Atmosphere – A Review. *Advances in Space Research*, 62(3):489–532, 2018. ISSN 0273-1177. doi: https://doi.org/10.1016/j.asr.2018.05.010.

[3] C. Johnston and A. Brandis. Aerothermodynamic Characteristics of 16-22 km/s Earth Entry. 06 2015. doi: 10.2514/6.2015-3110.

[4] J. D. Anderson Jr. *Hypersonic and High-Temperature Gas Dynamics, Second Edition*. 2006. doi: 10.2514/4.861956.

[5] C. Johnston and E. Stern. A Model for Thermal Radiation from the Tunguska Airburst. *Icarus*, 327, 02 2019. doi: 10.1016/j.icarus.2019.01.028.

[6] D. W. Hughes. The History of Meteors and Meteor Showers. *Vistas in Astronomy*, 26:325–345, 1982.

[7] G. A. Bird. Approach to Translational Equilibrium in a Rigid Sphere Gas. *Physics of Fluids*, 6(10):1518–1519, Oct. 1963. doi: 10.1063/1.1710976.

[8] I. D. Boyd. Computation of Atmospheric Entry Flow about a Leonid Meteoroid. *Earth, Moon, and Planets*, 82-83:93–108, 1998.

[9] F. Bariselli, A. Frezzotti, A. Hubin, and T. E. Magin. Aerothermodynamic Modelling of Meteor Entry Flows. *Monthly Notices of the Royal Astronomical Society*, 492(2):2308–2325, 12 2019. ISSN 0035-8711. doi: 10.1093/mnras/stz3559.

[10] P. Register, D. Mathias, and L. Wheeler. Asteroid Fragmentation Approaches for Modeling Atmospheric Energy Deposition. *Icarus*, 284, 11 2016. doi: 10.1016/j.icarus.2016.11.020.

[11] Z. Ceplecha and D. Revelle. Fragmentation Model of Meteoroid Motion, Mass Loss, and Radiation in the Atmosphere. *Meteoritics Planetary Science*, 40:35 – 54, 01 2005. doi: 10.1111/j.1945-5100.2005.tb00363.x.

[12] O. Popova. *Meteoroid Ablation Models*, volume 95, pages 303–319. 08 2006. ISBN 1-4020-4374-0. doi: 10.1007/1-4020-5075-5_32.

[13] M. Lino da Silva. *Simulation des propriétés radiatives du plasma entourant un véhicule traversant une atmosphére planétaire á vitesse hypersonique: application á la planéte Mars*. PhD thesis, Université d'Orléans, France, 2004.

[14] M. Lino da Silva, V. Guerra, J. Loureiro, and P. Sá. Vibrational distributions in N_2 with an improved calculation

of energy levels using the RKR method. *Chemical Physics*, 348:187–194, 06 2008. doi: 10.1016/j.chemphys.2008.02.048.

[15] M. Lino da Silva, J. Loureiro, and V. Guerra. Rotational nonequilibrium in state-resolved models for shock-heated flows. *Chemical Physics*, 398:96–103, 2012. ISSN 0301-0104. doi: https://doi.org/10.1016/j.chemphys.2011.08.014. Chemical Physics of Low-Temperature Plasmas (in honour of Prof Mario Capitelli).

[16] J.-k. Wang and Z.-s. Wu. Improved Calculation of Vibrational Energy Levels in F_2 Molecule using the RKR Method. *Chinese Journal of Chemical Physics*, 23(2):155–159, 2010. doi: 10.1088/1674-0068/23/02/155-159.

[17] C. O. Johnston, E. C. Stern, and L. F. Wheeler. Radiative heating of large meteoroids during atmospheric entry. *Icarus*, 309:25–44, 2018. ISSN 0019-1035. doi: https://doi.org/10.1016/j.icarus.2018.02.026.

[18] L. Fernandes. Computational Fluid Radiative Dynamics of The Galileo Jupiter Entry at 47.5 km/s. Master's thesis, Instituto Superior Técnico, May 2019.

[19] J. Coelho. Aerothermodynamic Analysis of Aerocapture and Ballistic Entry Flows in Neptune's Atmosphere. Master's thesis, Instituto Superior Técnico, December 2020.

[20] *SPARK Line-by-Line v.3.1, User Manual*.

[21] M. Born and R. Oppenheimer. Zur Quantentheorie der Molekeln. *Annalen der Physik*, 389(20):457–484, 1927. doi: https://doi.org/10.1002/andp.19273892002.

[22] B. Lopez, M. L. D. Silva, V. Guerra, and J. Loureiro. *Coupled Hydrodynamic/State-Specific High-Temperature Modeling of Nitrogen Vibrational Excitation and Dissociation*. . doi: 10.2514/6.2013-3149.

[23] C. Garbacz Gomes. State-to-state models in hypersonic flows. Master's thesis, Instituto Superior Técnico, September 2018.

[24] R. Y. R. J. Kramida, A. and N. A. Team. NIST Atomic Spectra Database (version 5.9), [Online]. Available: https://physics.nist.gov/asd [Wed Apr 20 2022]. National Institute of Standards and Technology, Gaithersburg, MD, 2021.

[25] J. L. Dunham. The Energy Levels of a Rotating Vibrator. *Phys. Rev.*, 41:721–731, Sep 1932. doi: 10.1103/PhysRev.41.721.

[26] G. Herzberg. *Molecular spectra and molecular structure. Vol.1: Spectra of diatomic molecules*. 1950.

[27] A. M. Teale and D. J. Tozer. Ground and excited-state diatomic bond lengths, vibrational levels, and potential-energy curves from conventional and localized Hartree–Fock based density-functional theory. *The Journal of Chemical Physics*, 122(3):034101, 2005. doi: 10.1063/1.1824892.

[28] R. Rydberg. Graphische Darstellung einiger bandenspektroskopischer Ergebnisse. *Zeitschrift für Physik*, 73:376–385, 05 1932. doi: https://doi.org/10.1007/BF01341146.

[29] O. Klein. Zur Berechnung von Potentialkurven für zweiatomige Moleküle mit Hilfe von Spektraltermen. *Zeitschrift für Physik*, 76:226–235, 1932.

[30] A. L. G. Rees. The calculation of potential-energy curves from band-spectroscopic data. *Proceedings of the Physical Society*, 59(6):998–1008, nov 1947. doi: 10.1088/0959-5309/59/6/310.

[31] A. Ghatak and S. Lokanathan. *Quantum Mechanics: Theory and Applications*, pages 423–477. 01 2004.

[32] R. J. Le Roy. RKR1: A computer program implementing the first-order RKR method for determining diatomic

molecule potential energy functions. *Journal of Quantitative Spectroscopy and Radiative Transfer*, 186:158–166, 2017. ISSN 0022-4073. doi: https://doi.org/10.1016/j.jqsrt.2016.03.030. Satellite Remote Sensing and Spectroscopy: Joint ACE-Odin Meeting, October 2015.

[33] F. Gilmore. Potential energy curves for N_2, NO, O_2 and corresponding ions. *Journal of Quantitative Spectroscopy and Radiative Transfer*, 5(2):369–389, Apr. 1965. doi: 10.1016/0022-4073(65)90072-5.

[34] H. M. Hulburt and J. O. Hirschfelder. Potential Energy Functions for Diatomic Molecules. *The Journal of Chemical Physics*, 9(1):61–69, 1941. doi: 10.1063/1.1750827.

[35] G. G. Balint-Kurti, R. N. Dixon, and C. C. Marston. Grid methods for solving the Schrödinger equation and time dependent quantum dynamics of molecular photofragmentation and reactive scattering processes. *International Reviews in Physical Chemistry*, 11(2):317–344, 1992. doi: 10.1080/01442359209353274.

[36] R. J. Le Roy. *Equilibrium Structures of Molecules*, chapter 6 - Determining equilibrium structures and potential energy functions for diatomic molecules, pages 159–203. CRC Press, 2011.

[37] R. Le Roy, Y. Huang, and C. Jary. An accurate analytic potential function for ground-state N_2 from a direct-potential-fit analysis of spectroscopic data. *The Journal of chemical physics*, 125:164310, 11 2006. doi: 10.1063/1.2354502.

[38] C. O. Johnston and M. Panesi. Impact of state-specific flowfield modeling on atomic nitrogen radiation. *Phys. Rev. Fluids*, 3:013402, Jan 2018. doi: 10.1103/PhysRevFluids.3.013402.

[39] D. Potter. *Modelling of radiating shock layers for atmospheric entry at Earth and Mars*. PhD thesis, University of Queensland, 2011.

[40] C. R. Wilke. A Viscosity Equation for Gas Mixtures. *The Journal of Chemical Physics*, 18(4):517–519, 1950. doi: 10.1063/1.1747673.

[41] G. E. Palmer and M. J. Wright. Comparison of Methods to Compute High-Temperature Gas Viscosity. *Journal of Thermophysics and Heat Transfer*, 17(2):232–239, 2003. doi: 10.2514/2.6756.

[42] F. G. Blottner, M. M. Johnson, and M. A. Ellis. Chemically Reacting Viscous Flow Program for Multi-Component Gas Mixtures. 1971.

[43] G. Palmer and M. Wright. *A Comparison of Methods to Compute High-Temperature Gas Thermal Conductivity*. doi: 10.2514/6.2003-3913.

[44] D. D. Loureiro. High-Temperature Modeling of Transport Properties in Hypersonic Flows. Master's thesis, Instituto Superior Técnico, November 2015.

[45] L. C. Scalabrin. *Numerical simulation of weakly ionized hypersonic flow over reentry capsules*. PhD thesis, University of Michigan, 2007.

[46] R. Gupta, J. Yos, R. Thompson, and K.-P. Lee. A review of reaction rates and thermodynamic and transport properties for an 11-species air model for chemical and thermal nonequilibrium calculations to 30 000 K. September 1990.

[47] F. F. Chen. *Introduction to plasma physics and controlled fusion*. Second edition, 12 1984. URL `https://www.osti.gov/biblio/140016`.

[48] J.-H. Lee. *Basic governing equations for the flight regimes of aeroassisted orbital transfer vehicles*. doi: 10.2514/6.1984-1729.

[49] B. Lopez and M. Lino da Silva. *SPARK: A Software Package for Aerodynamics, Radiation and Kinetics*. doi: 10.2514/6.2016-4025.

[50] J. M. Picone, A. E. Hedin, D. P. Drob, and A. C. Aikin. NRLMSISE-00 empirical model of the atmosphere: Statistical comparisons and scientific issues. *Journal of Geophysical Research (Space Physics)*, 107(A12): 1468, Dec. 2002. doi: 10.1029/2002JA009430.

[51] O. Popova, J. Borovicka, W. K. Hartmann, P. Spurný, E. GNOS, I. Nemtchinov, and J. M. Trigo-Rodríguez. Very low strengths of interplanetary meteoroids and small asteroids. *Meteoritics & Planetary Science*, 46(10): 1525–1550, 2011. doi: https://doi.org/10.1111/j.1945-5100.2011.01247.x.

[52] J. Borovička, P. Spurný, P. Brown, P. Wiegert, P. Kalenda, D. Clark, and L. Shrbený. The trajectory, structure and origin of the Chelyabinsk asteroidal impactor. *Nature*, 503, 11 2013. doi: 10.1038/nature12671.

[53] O. Popova, P. Jenniskens, V. Emel, A. Kartashova, E. Biryukov, S. Khaibrakhmanov, V. Shuvalov, Y. Rybnov, A. Dudorov, V. Grokhovsky, D. Badyukov, Q.-Z. Yin, P. Gural, J. Albers, M. Granvik, L. Evers, J. Kuiper, V. Kharlamov, A. Solovyov, and T. Mikouchi. Chelyabinsk Airburst, Damage Assessment, Meteorite Recovery, and Characterization. *Science*, 342:1069, 11 2013. doi: 10.1126/science.1242642.

[54] C. Chyba, P. Thomas, and K. Zahnle. The 1908 Tunguska explosion: Atmospheric disruption of a stony asteroid. *Nature*, 361:40–44, Jan. 1993. doi: 10.1038/361040a0.

[55] S. D. Gordon and B. J. McBride. Thermodynamic Data to 20 000 K For Monatomic Gases. 1999.

[56] B. McBride, M. Zehe, and S. Gordon. NASA Glenn coefficients for calculating thermodynamic properties of individual species. 10 2002.

[57] K. P. Huber and G. Herzberg. *Constants of diatomic molecules*, pages 8–689. Springer US, Boston, MA, 1979. ISBN 978-1-4757-0961-2. doi: 10.1007/978-1-4757-0961-2_2.

[58] P. H. K. Lofthus, Alf. The spectrum of molecular nitrogen. *Journal of Physical and Chemical Reference Data*, 6:113–307, 1977.

[59] P. H. Krupenie. The Spectrum of Molecular Oxygen. *Journal of Physical and Chemical Reference Data*, 1(2): 423–534, 1972. doi: 10.1063/1.3253101.

[60] K. K. Irikura. Experimental Vibrational Zero-Point Energies: Diatomic Molecules. *Journal of Physical and Chemical Reference Data*, 36(2):389–397, 2007. doi: 10.1063/1.2436891.

[61] J. Y. Roncin, F. Launay, and M. Larzilliere. Evidence for Predissociation of N_2 into $\mathrm{N}(^2D) + \mathrm{N}(^2D)$ from New High-Resolution Vacuum-Ultraviolet Emission Bands. *Phys. Rev. Lett.*, 53:159–162, Jul 1984. doi: 10.1103/PhysRevLett.53.159.

[62] X. Tang, Y. Hou, C. Y. Ng, and B. Ruscic. Pulsed field-ionization photoelectron-photoion coincidence study of the process N_2+h $\nu \rightarrow \mathrm{N}^+$ + N + e^-: Bond dissociation energies of N_2 and N_2^+. *The Journal of Chemical Physics*, 123.

[63] R. P. Saxon and B. Liu. Ab initio configuration interaction study of the valence states of o_2. *The Journal of Chemical Physics*, 67(12):5432–5441, 1977. doi: 10.1063/1.434764.

[64] H. Liu, J. Sun, Z. Zhu, and Z. Shulin. Accurate calculations on the 22 electronic states and 54 spin-orbit states of the O_2 molecule: Potential energy curves, spectroscopic parameters and spin-orbit coupling. pages 216–229, january 2014.

[65] S. Chauveau. Constitution de bases de données spectroscopiques relatives à un plasma d'air : application au calcul de transferts radiatifs. 2001.

[66] A.-C. Cheung, K. Yoshino, W. Parkinson, and D. Freeman. Molecular spectroscopic constants of O_2 (B_u^3): The upper state of the Schumann-Runge bands. *Journal of Molecular Spectroscopy*, 119(1):1–10, 1986. ISSN 0022-2852. doi: https://doi.org/10.1016/0022-2852(86)90196-7.

[67] R. S. Friedman. Oscillator strengths of the Schumann-Runge bands of isotopic oxygen molecules. , 43: 225–238, Mar. 1990. doi: 10.1016/0022-4073(90)90055-B.

[68] C. O. Laux. *Optical Diagnostics and Radiative Emission of Air Plasmas*. PhD thesis, STANFORD UNIVERSITY., Jan. 1993.

[69] M. Born and V. Fock. Beweis des Adiabatensatzes. *Zeitschrift fur Physik*, 51(3-4):165–180, Mar. 1928. doi: 10.1007/BF01343193.

[70] H. Lefebvre-Brion and R. W. Field. Perturbations in the spectra of diatomic molecules. 1 1986. URL `https://www.osti.gov/biblio/6969056`.

[71] C. by Alan D. McNaught and A. Wilkinson. *Compendium of chemical terminology : IUPAC recommendations*. Second edition. Oxford [Oxfordshire] ; Malden, MA : Blackwell Science, 1997, 1997.

[72] J. N. Harvey. Understanding the kinetics of spin-forbidden chemical reactions. *Phys. Chem. Chem. Phys.*, 9: 331–343, 2007. doi: 10.1039/B614390.

[73] S. M. Blinder. Non-Crossing Rule for Energy Curves in Diatomic Molecules. http://demonstrations.wolfram.com/NonCrossingRuleForEnergyCurvesInDiatomicMolecules/, 2021. (accessed: 10.05.2022).

[74] J. R. Oppenheimer. Three Notes on the Quantum Theory of Aperiodic Effects. *Phys. Rev.*, 31:66–81, Jan 1928.

[75] C. A. Moyer. A unified theory of quasibound states. *AIP Advances*, 4(2):027109, 2014. doi: 10.1063/1.4865998.

[76] M. Lino da Silva, J. Loureiro, and V. Guerra. A multiquantum dataset for vibrational excitation and dissociation in high-temperature O2–O2 collisions. *Chemical Physics Letters*, 531:28–33, 2012. ISSN 0009-2614. doi: https://doi.org/10.1016/j.cplett.2012.01.074.

[77] M. Capitelli, G. Colonna, D. Giordano, L. Marraffa, A. Casavola, P. Minelli, D. Pagano, L. Pietanza, F. Taccogna, and B. Warmbein. Tables of internal partition functions and thermodynamic properties of high-temperature Mars-Atmosphere species from 50 K to 50 000 K. *ESA Scientific Technical Review*, 246, 09 2005.

[78] M. Capitelli, G. Colonna, D. Giordano, L. Marraffa, A. Casavola, P. Minelli, D. Pagano, L. Pietanza, and F. Taccogna. High-Temperature Thermodynamic Properties of Mars-Atmosphere Components. *Journal of Spacecraft and Rockets*, 42:980, 11 2005. doi: 10.2514/1.12503.

[79] C. Johnston, B. Hollis, and K. Sutton. Spectrum modeling for air shock-layer radiation at lunar-return conditions. *Journal of Spacecraft and Rockets - J SPACECRAFT ROCKET*, 45:865–878, 09 2008. doi: 10.2514/1.33004.

[80] C. H. Park. Nonequilibrium Hypersonic Aerothermodynamics. 1989.

[81] C. Park, J. T. Howe, R. L. Jaffe, and G. V. Candler. Review of chemical-kinetic problems of future NASA missions. II - Mars entries. *Journal of Thermophysics and Heat Transfer*, 8(1):9–23, 1994. doi: 10.2514/3.496.

[82] C. Park, R. L. Jaffe, and H. Partridge. Chemical-Kinetic Parameters of Hyperbolic Earth Entry. *Journal of Thermophysics and Heat Transfer*, 15(1):76–90, 2001. doi: 10.2514/2.6582.

[83] C. Johnston. Nonequilibrium shock-layer radiative heating for Earth and Titan entry. 01 2006.

[84] K. L. Bell, H. B. Gilbody, J. G. Hughes, A. E. Kingston, and F. J. Smith. Recommended data on the electron impact ionization of light atoms and ions. *Journal of Physical and Chemical Reference Data*, 12(4):891–916, 1983. doi: 10.1063/1.555700. URL https://doi.org/10.1063/1.555700.

[85] G. Voronov. A practical fit formula for ionization rate coefficients of atoms and ions by electron impact: Z = 1–28. *Atomic Data and Nuclear Data Tables*, 65(1):1–35, 1997. ISSN 0092-640X. doi: https://doi.org/10.1006/adnd.1997.0732. URL https://www.sciencedirect.com/science/article/pii/S0092640X97907324.

[86] C. Park. Collisional ionization and recombination rates of atomic nitrogen. *AIAA Journal*, 7(8):1653–1654, 1969. doi: 10.2514/3.5467. URL https://doi.org/10.2514/3.5467.

[87] B. E. Lopez, C. O. Johnston, and M. Panesi. *Improved Non-Boltzmann Modeling for Nitrogen Atoms*. . doi: 10.2514/6.2016-4431. URL https://arc.aiaa.org/doi/abs/10.2514/6.2016-4431.

[88] S. Gasiorowicz. *Quantum Physics*. Wiley India Pvt. Limited, 2007. ISBN 9788126511174. URL https://books.google.pt/books?id=qFtQiVmjWUEC.

[89] H. Liu, J. Sun, and Z. Zhu. Accurate theoretical spectroscopic investigations of the 20 $\Lambda-\Sigma$ and 58 Ω states of O_2^+ cation including the spin–orbit coupling effect. *Molecular Physics*, 113, 01 2015. doi: 10.1080/00268976.2014.948516.

[90] T. Tanaka, H. Yoshii, Y. Morioka, T. Hayaishi, K. Ito, and R. I. Hall. High-resolution threshold photoelectron spectra of molecular oxygen in the 18–24 eV region. *The Journal of Chemical Physics*, 108(15):6240–6248, 1998. doi: 10.1063/1.476031.

[91] M. Evans, S. Stimson, C. Y. Ng, C.-W. Hsu, and G. K. Jarvis. Rotationally resolved pulsed field ionization photoelectron study of O_2^+ ($B^2\Sigma_g$,$^2\Sigma_u$; v=0–7) at 20.2–21.3 eV. *The Journal of Chemical Physics*, 110(1):315–327, 1999. doi: 10.1063/1.477915.

[92] C. V. V. Prasad, D. Lacombe, K. Walker, W. Kong, P. Bernath, and J. Hepburn. Fourier transform emission spectroscopy of the second negative $(A^2\Pi_u - X^2\Pi_g) system of the O_2^+$ ion. *Molecular Physics*, 91(6):1059–1074, 1997. doi: 10.1080/002689797170806.

[93] Y. Song, M. Evans, C. Y. Ng, C.-W. Hsu, and G. K. Jarvis. Rotationally resolved pulsed field ionization photoelectron bands for O_2^+ ($a^4\Pi_u$, v=0–18) in the energy range of 16.0–18.0 eV. *The Journal of Chemical Physics*, 112(3):1306–1315, 2000. doi: 10.1063/1.480682.

[94] H. Shi and A. L. L. East. Improved results for the excited states of nitric oxide, including the BC avoided crossing. *The Journal of Chemical Physics*, 125(10):104311, 2006. doi: 10.1063/1.2336214.

[95] K. Dressler and E. Miescher. On highly excited electronic states of the NO molecule reached by multiphoton spectroscopy. *The Journal of Chemical Physics*, 75(9):4310–4316, 1981. doi: 10.1063/1.442637.

[96] C. Jungen. Vacuum-ultraviolet emission and absorption spectrum of the NO molecule: the 2Δ states and their interactions. *Canadian Journal of Physics*, 44(12):3197–3216, 1966. doi: 10.1139/p66-261.

[97] M. R. Taherian, P. C. Cosby, and T. G. Slanger. Detection and characterization of the NO($L'^2\Phi_i$) state at 6.6 eV. *The Journal of Chemical Physics*, 83(8):3878–3887, 1985. doi: 10.1063/1.449099.

[98] R. Gallusser and K. Dressler. Multistate vibronic coupling between the excited 2 states of the NO molecule. *The Journal of Chemical Physics*, 76(9):4311–4327, 1982. doi: 10.1063/1.443565.

[99] R. JAFFE. *The calculation of high-temperature equilibrium and nonequilibrium specific heat data for* $\mathrm{N_2}$, $\mathrm{O_2}$ *and* NO. doi: 10.2514/6.1987-1633.

[100] C. Amiot. The infrared emission spectrum of NO: Analysis of the v = 3 sequence up to v = 22. *Journal of Molecular Spectroscopy*, 94(1):150–172, 1982. ISSN 0022-2852. doi: https://doi.org/10.1016/0022-2852(82)90301-0.

[101] D. L. Albritton, A. L. Schmeltekopf, and R. N. Zare. Potential energy curves for $\mathrm{NO^+}$. *The Journal of Chemical Physics*, 71(8):3271–3279, 1979. doi: 10.1063/1.438757.

[102] D. Spelsberg and W. Meyer. Dipole-allowed excited states of $\mathrm{N_2}$: Potential energy curves, vibrational analysis, and absorption intensities. *The Journal of Chemical Physics*, 115(14):6438–6449, 2001. doi: 10.1063/1.1400139.

[103] D. Stahel, M. Leoni, and K. Dressler. Nonadiabatic representations of the $^1\Sigma_u^+$ and $^1\Pi_u$ states of the $\mathrm{N_2}$ molecule. *The Journal of Chemical Physics*, 79(6):2541–2558, 1983. doi: 10.1063/1.446166.

[104] R. R. Laher and F. R. Gilmore. Improved Fits for the Vibrational and Rotational Constants of Many States of Nitrogen and Oxygen. *Journal of Physical and Chemical Reference Data*, 20(4):685–712, 1991. doi: 10.1063/1.555892.

[105] R. Bachmann, C. Ottinger, and A. F. Vilesov. A new band system of nitrogen: Observation of the $\mathrm{N_2}$(G $^3\Delta_g$ $\rightarrow$ W $^3\Delta_u$) transition. *The Journal of Chemical Physics*, 99(5):3262–3267, 1993. doi: 10.1063/1.465134.

[106] L. R. Ventura and C. E. Fellows. The $\mathrm{N_2}$ second positive (C$^3\Pi$ $\rightarrow$B$^3\Pi$) system reviewed: Improved data and analysis. *Journal of Quantitative Spectroscopy & Radiative Transfer*, 239:106645, 2019.

[107] S. Gruet, A. Morvan, O. Pirali, T. Chamaillé, E. Bouisset, and M. Vervloet. Fourier transform far-infrared spectroscopy of HN2+on the AILES beamline of synchrotron SOLEIL1. *Canadian Journal of Physics*, 91: 937–940, 11 2013. doi: 10.1139/cjp-2012-0530.

[108] K. P. Huber and M. Vervloet. High-resolution Fourier transform spectroscopy of supersonic jets. The C"$^5\Pi_{ui}$ $\rightarrow$ A'$^5\Sigma_g^+$ Herman infrared bands of $^{14}N_2$. *Journal of Molecular Spectroscopy*, 153:17–25, 1992.

[109] C. Ottinger and A. F. Vilesov. Laser spectroscopy of perturbed levels in $\mathrm{N_2}$(B$^3\Pi_g$,v=10) and the first experimental determination of the $\mathrm{N_2}$(A'$^5\Sigma_g^+$) term energy. *The Journal of Chemical Physics*, 100(7):4862–4869, 1994. doi: 10.1063/1.467206.

[110] M. Hochlaf, H. Ndome, and D. Hammoutène. Quintet electronic states of $\mathrm{n_2}$. *The Journal of Chemical Physics*, 132(10):104310, 2010. doi: 10.1063/1.3359000.

[111] Z. Qin, J. Zhao, and L. Liu. Radiative transition probabilities between low-lying electronic states of $\mathrm{N_2}$. *Molecular Physics*, 117(18):2418–2433, 2019. doi: 10.1080/00268976.2018.1562579.

[112] H. Werner, J. Kalcher, and E. Reinsch. Accurate ab initio calculations of radiative transition probabilities between the A$^3\Sigma_u^+$, B$^3\Pi_g$, W$^3\Delta_u$, B$^3\Sigma_u^-$, and C$^3\Pi_u$ states of $\mathrm{N_2}$. *The Journal of Chemical Physics*, 81(5): 2420–2431, 1984. doi: 10.1063/1.447917.

[113] W. Jiang and A. K. Wilson. Multireference composite approaches for the accurate study of ground and excited electronic states: C_2, N_2, and O_2. *The Journal of Chemical Physics*, 134(3):034101, 2011. doi: 10.1063/1.3514031.

[114] Z. Qin, J. Zhao, and L. H. Liu. Radiative transition probabilities between low-lying electronic states of n_2. *Molecular Physics*, 117:1–16, 01 2019. doi: 10.1080/00268976.2018.1562579.

[115] F. Roux and F. Michaud. Investigation of the rovibrational levels of the $B^3\Pi_g$ state of $^{14}N_2$ molecule above the dissociation limit N(^{4}S)+N(^{4}S) by Fourier transform spectrometry. *Canadian Journal of Physics*, 68(11): 1257–1261, 1990. doi: 10.1139/p90-181.

[116] S. Edwards, J. Roncin, F. Launay, and F. Rostas. The Electronic Ground State of Molecular Nitrogen. *Journal of Molecular Spectroscopy*, 162(1):257–267, 1993. ISSN 0022-2852. doi: https://doi.org/10.1006/jmsp.1993.1282.

[117] L. Klynning and P. Pagès. The Band Spectrum of N_2^+. *Physica Scripta*, 25:543, 12 2006. doi: 10.1088/0031-8949/25/4/009.

[118] C. E. Moore and J. W. Gallagher. Tables of spectra of hydrogen, carbon, nitrogen, and oxygen atoms and ions. 1993.

[119] A. Bourdon and P. Vervisch. Study of a low-pressure nitrogen plasma boundary layer over a metallic plate. *Physics of Plasmas*, 4(11):4144–4157, 1997. doi: 10.1063/1.872535.

[120] K. Fujita, T. Yamada, and N. Ishii. Impact of Ablation Gas Kinetics on Hyperbolic Entry Radiative Heating. 2006.

[121] C. Johnston and A. Brandis. Modeling of nonequilibrium CO Fourth-Positive and CN Violet emission in CO_2–N_2 gases. *Journal of Quantitative Spectroscopy and Radiative Transfer*, 149:303–317, 2014. ISSN 0022-4073. doi: https://doi.org/10.1016/j.jqsrt.2014.08.025.

[122] D. Bose and G. V. Candler. Thermal rate constants of the O_2+N$\rightarrow$NO+O reaction based on the A^{2}' and A^{4}' potential-energy surfaces. *The Journal of Chemical Physics*, 107(16):6136–6145, 1997. doi: 10.1063/1.475132.

[123] P. Teulet, J. J. Gonzalez, A. Mercado-Cabrera, Y. Cressault, and A. Gleizes. One-dimensional hydro-kinetic modelling of the decaying arc in AIR–PA66–copper mixtures: I. Chemical kinetics, thermodynamics, transport and radiative properties. *Journal of Physics D: Applied Physics*, 42(17):175201, aug 2009. doi: 10.1088/0022-3727/42/17/175201.

Appendix A

Thermodynamic properties of quantum systems

A.1 Partition Functions, Thermodynamic Properties and Modal Contributions

Recovering the definition of internal energy and partition function, those are, respectively:

$$e = RT^2(\frac{\partial \ln Q}{\partial T})_V \tag{A.1}$$

$$Q = \sum_j g_j \exp(\frac{-\varepsilon_j}{k_B T}) \tag{A.2}$$

Within the Born-Oppenheimer approximation of the separability of internal energy modes, the total partition function may be decomposed into:

$$\begin{aligned} Q &= \sum_i \sum_j \sum_n \sum_l g_i g_j g_n g_l \exp[-\frac{1}{k_B T}(\varepsilon_{i_{tr}} + \varepsilon_{j_{rot}} + \varepsilon_{n_{vib}} + \varepsilon_{l_{exc}})] \\ &= [\sum_i g_i \exp(-\frac{\varepsilon_{i_{tr}}}{k_B T})][\sum_j g_j \exp(-\frac{\varepsilon_{j_{rot}}}{k_B T})][\sum_n g_n \exp(-\frac{\varepsilon_{n_{vib}}}{k_B T})][\sum_l g_l \exp(-\frac{\varepsilon_{l_{exc}}}{k_B T})] \\ &= Q_{tr} Q_{rot} Q_{vib} Q_{exc} \end{aligned} \tag{A.3}$$

This separation of energy modes, that translates to the factorization of the total partition function in its modal contributions, allows for the use of separate temperatures for each modal partition function when thermal non-equilibrium is considered. Each modal contribution depends on the energy levels of said mode, and those result from solving the appropriate Schrodinger equation.

For a single species-gas, the internal energies of each mode , that results from equation A.1, are:

$$e_{tr,s} = \frac{3}{2} R_s T \tag{A.4}$$

$$e_{rot,s} = R_s T \tag{A.5}$$

$$e_{vib,s} = \frac{\frac{h\nu_s}{k_B T}}{\exp(\frac{h\nu_s}{k_B T}) - 1} R_s T \tag{A.6}$$

$$e_{exc,s} = R_s T^2 \frac{\partial}{\partial T} \{\ln [\sum_l g_{l,s} \exp(-\frac{\varepsilon_{l_{exc,s}}}{k_B T})]\} \tag{A.7}$$

where h is the Planck's constant and ν_s the fundamental vibration frequency of the molecule. The calculation of the electronic excitation contribution relies on a sum over all achievable energy levels before ionization, as it cannot be described with a simple explicit expression.

Using the thermodynamic relation between internal energy and enthalpy, one obtains the enthalpy of the mixture as:

$$h = \sum_s c_s h_s \quad \text{, with} \quad h_s = e_s + \frac{p_s}{\rho_s} = e_s + R_s T \tag{A.8}$$

Once again, this property for a given species can be calculated as the sum of the contributions of the thermal modes:

$$h_s = h_{tr,s} + h_{rot,s} + h_{vib,s} + h_{exc,s} + (\Delta h_f)_s^o \tag{A.9}$$

with $(\Delta h_f)_s^o$ being the formation enthalpy of that species and each contribution being:

$$h_{tr,s} = e_{tr,s} + R_s T \quad , \quad h_{rot,s} = e_{rot,s} \quad , \quad h_{vib,s} = e_{vib,s} \quad , \quad h_{exc,s} = e_{exc,s} \tag{A.10}$$

It is noteworthy that only the translation component retains the term $R_s T$, since it is this motion that is responsible for the existence of a pressure force.

Specific heats are defined as:

$$C_v = (\frac{\partial e}{\partial T})_v \quad \text{, with} \quad C_p = (\frac{\partial h}{\partial T})_p \tag{A.11}$$

These equations explain why the Mach number is a concept that loses meaning in hypersonic chemically reacting flows. If one replaces the mixture's internal energy and enthalpy in terms of its components:

$$C_v = \sum_s [e_s \frac{\partial c_S}{\partial T} + c_s \frac{\partial e_S}{\partial T}] = C_v^r + C_v^f \tag{A.12}$$

$$C_p = \sum_s [h_s \frac{\partial c_S}{\partial T} + c_s \frac{\partial h_S}{\partial T}] = C_p^r + C_p^f \tag{A.13}$$

so, the specific heats can be separated in frozen and reactive components. When in chemically frozen flows, the reactive terms are negligible - this happens for most regime flights with $Ma < 5$. However, when in chemically reacting flows, which is the case studied throughout this work, the reactive term varies with the mixture's composition, so the specific heat ratio $\gamma = \frac{C_p}{C_v}$ changes significantly. Since γ is necessary to calculate speed of sound (even though there is no explicit closed-form expression for it in chemically reacting flow), the speed of sound will also change significantly with the mixture composition in chemically reacting flows, and this composition changes with temperature, so the concept of Mach number as a comparison of a velocity to the speed of sound loses usefulness in this ever-changing flight regimes.

A.2 Schrödinger Equation

The Schrödinger equation [88] is a linear partial differential equation that describes the time evolution of a quantum system and may be written as:

$$H\psi = i\hbar \frac{\partial \psi}{\partial t} \tag{A.14}$$

where ψ is a wavefunction and H is the hamiltonian operator. H is a quantum mechanical operator that, classically, corresponds to the total energy of a system ($\frac{p^2}{2m} + V$). In quantum mechanics, the hamiltonian is composed of two operators that act on the wavefunction - the kinetic energy operator and the potential energy operator:

$$H = -\frac{\hbar^2}{2m}\nabla^2 + V \tag{A.15}$$

where $V(\vec{r}, t)$ is the potential curve and the wavefunction $\psi(\vec{r}, t)$ depends on its spatial coordinates and time. Equation A.14 can then be written as

$$-\frac{\hbar^2}{2m}\nabla^2\psi(\vec{r}, t) + V(\vec{r}, t)\psi(\vec{r}, t) = i\hbar\frac{\partial \psi(\vec{r}, t)}{\partial t} \tag{A.16}$$

If the potential is independent of time, then through separation of variables one gets:

$$-\frac{\hbar^2}{2m}\nabla^2\psi(\vec{r}) + V(\vec{r})\psi(\vec{r}) = C\psi(\vec{r}) \tag{A.17}$$

One can observe that the left-side of the equation is the hamiltonian acting on $\psi(\vec{r})$, which means that the constant C represents the eigenvalues of the hamiltonian operator - the quantized energies of the system, E.

The Schrödinger equation can be written in its stationary form as:

$$\nabla^2\psi(\vec{r}) + \frac{2m}{\hbar^2}\left(E - V\right)\psi(\vec{r}) = 0 \tag{A.18}$$

or in its matrix form:

$$H\psi(\vec{r}) = E\psi(\vec{r}) \tag{A.19}$$

For a problem with a central potential, as the one being solved here, one may consider spherical coordinates and solve the radial part of the equation, obtained once again by applying separation of variables, $\psi(\vec{r}) = \psi(r, \theta, \Phi) = R(r)Y_l^m(\theta, \Phi)$, and then making a change of variables from R(r) to $u(r) = rR(r)$ - the reduced radial wavefunction. The radial Schrödinger equation is then:

$$\frac{d}{dr^2}u(r) + \left(-\frac{l(l+1)}{r^2} + \frac{2\mu}{\hbar^2}\left(E - V(r)\right)\right)u(r) = 0 \tag{A.20}$$

with $\hbar^2 l(l+1)$ being the eigenvalues of the angular momentum and μ the reduced mass. The angular part of the equation may be solved separately using spherical harmonics.

Solving the radial Schrödinger equation for each $V_J(r)$ will yield the systems' rovibrational energies as eigenvalues and the corresponding wavefunctions as eigenstates.

Appendix B

Data

B.1 Updated Spectroscopic Database

Table B.1: Updated spectroscopic database and other relevant data for reconstruction O_2^+ potential curves. The values tagged with (*) were estimated in this work.

State	T(e) (cm^{-1})		ω_e	$-\omega_e x_e$	$\omega_e y_e$	$\omega_e z_e$	$\omega_e a_e$	B_e	α_e	γ_e	δ_e	v_{max}^{valid}	Dis. Prod.	Extrap.	Ref.
		Y_{00}	Y_{10}	Y_{20}	Y_{30}	Y_{40}	Y_{50}	Y_{01}	Y_{11}	Y_{21}	Y_{31}				
O_2^+															
$c^4\Sigma_u^-$	100914		1545					1.561				1*	-	-	[57, 89]
$B^2\Sigma_g^-$	66660.7		1152.91	-20.97				1.255	-0.0241			5*	$O(^3P)+O^+(^2D)$	HH	[57, 89–91]
$b^4\Sigma_g^-$	49952		1196.8	-17.09				1.2872	-0.02206			3*	$O(^1D)+O^+(^4S)$	HH	[57, 59, 89]
$A^2\Pi_u$	40572.79		898.65	-13.574				1.0619	-0.019598			8*	$O(^3P)+O^+(^4S)$	HH	[57, 59, 89, 92]
$a^4\Pi_u$	32906.2		1035.93	-10.20				1.1067	-0.0167			6*	$O(^3P)+O^+(^4S)$	HH	[57, 89, 93]
$X^2\Pi_g$	0		1905.89	-16.489				1.6898	-0.019363			10*	$O(^3P)+O^+(^4S)$	HH	[57, 89, 92]

Table B.2: Updated spectroscopic database and other relevant data for reconstruction NO potential curves. The values tagged with (*) were estimated in this work.

State	T(e) (cm^{-1})		ω_e	$-\omega_e x_e$	$\omega_e y_e$	$\omega_e z_e$	$\omega_e a_e$	B_e	α_e	γ_e	δ_e	v_{max}^{valid}	Dis. Prod.	Extrap.	Ref.
		Y_{00}	Y_{10}	Y_{20}	Y_{30}	Y_{40}	Y_{50}	Y_{01}	Y_{11}	Y_{21}	Y_{31}				
NO															
$L^2\Pi$	61563		974.6					1.154				1*	$N(2P)+O(3P)$	ER	[94, 95]
$G^2\Sigma^-$	62913		1085.54	-11.08				1.25230	-0.02040			5*	$N(2D)+O(3P)$	ER	[57, 80]
$H'^2\Pi$	62485.4		2371.3	-16.17				2.015	-0.02100			2*	-	-	[57]
$H^2\Sigma^+$	62473.4		2339.4					2.0030	-0.01800			2*	-	-	[57, 80]
$F^2\Delta$	61800		2394.0	-20.00				1.98200	-0.02300			4*	-	-	[57, 80]
$E^2\Sigma^+$	60629	-0.141	2375.3	-16.43				1.9863	-0.0182			4	-	-	[57, 65]
$B'^2\Delta_i$	60364	-0.049	1217.4	-15.61				1.332	-0.021			6	$N(2D)+O(3P)$	ER	[57, 65, 96]
$L'^2\Phi$	53675.5		1000.0					1.117				1*	-	-	[94, 97]
$D^2\Sigma^+$	53085	-0.908	2323.9	-22.885	0.75	-0.22		2.0026	-0.02175			5	-	-	[57, 65]
$C^2\Pi_r$	52186	4.834	2381.3	-15.702				2.0155	-0.03244			9	-	-	[65, 80, 98, 99]
$b^4\Sigma^-$	47950		1206.0	-15.00				1.3358				5*	$N(^2D)+O(^1D)$	ER	[80, 99]
$B^2\Pi_r$	45932	0.334	1042.4	-7.7726	0.11596	-3.95770e-03		1.1244	-0.013433	2.99100e-05	-3.17700e-06	37	-	-	[57, 65, 98]
$A^2\Sigma^+$	43965.7	0.174	2374.31	-16.106	-0.0465			1.9965	-0.01915			8	-	-	[57, 65]
$a^4\Pi_i$	38807		1019.0	-12.80				1.12750				5*	$N(^4S)+O(^3P)$	ER	[80, 99]
$X^2\Pi_r$	0	0.1	1904.13455	-14.088358	0.0100467	-1.53310e-04	-9.76900e-06	1.70488847	-0.01754158	-1.48860e-05	0	22	$N(^4S)+O(^3P)$	HH	[65, 68, 100]

Table B.3: Updated spectroscopic database and other relevant data for reconstruction NO^+ potential curves.

State	T(e) (cm^{-1})	Y_{00}	ω_e	$-\omega_e x_e$	$\omega_e y_e$	$\omega_e z_e$	$\omega_e a_e$	B_e	α_e	γ_e	δ_e	v_{max}^{valid}	Dis. Prod.	Extrap.	Ref.
		Y_{00}	Y_{10}	Y_{20}	Y_{30}	Y_{40}	Y_{50}	Y_{01}	Y_{11}	Y_{21}	Y_{31}				
NO^+															
$A^1\Pi$	73471.83		1601.927	-20.2075	-0.269			1.584057	-0.022194	-0.00046		4	$N^+(^3P)+O(^3P)$	HH	[101]
$W^1\Delta$	71647		1217.74	-11.587				1.333	-0.0171			9	$N^+(^3P)+O(^3P)$	HH	[101]
$A'^1\Sigma^-$	69543.3		1279.88	-13.206				1.363	-0.0184			11	$N^+(^3P)+O(^3P)$	HH	[101]
$b'^3\Sigma^-$	67776.52		1283.228	-10.7689				1.38685	-0.024681			9	$N^+(^3P)+O(^3P)$	HH	[101]
$w^3\Delta$	61914.3		1316.89	-10.834				1.381	-0.0156			9	$N^+(^3P)+O(^3P)$	HH	[101]
$b^3\Pi$	59177		1710	-14.18				1.634	-0.0184			1	-	-	[101]
$a^3\Sigma^+$	52145.6		1303.07	-15.158				1.375	-0.0202			9	$N(^4S)+O^+(^4S)$	HH	[101]
$X^1\Sigma^+$	0		2376.721	-16.2553	-0.016			1.997195	-0.01879			34	$N(^4S)+O^+(^4S)$	HH	[101]

Table B.4: Updated spectroscopic database and other relevant data for reconstruction N_2 potential curves. The values tagged with (*) were estimated in this work.

State	T(e) (cm^{-1})	Y_{00}	ω_e	$-\omega_e x_e$	$\omega_e y_e$	$\omega_e z_e$	$\omega_e a_e$	B_e	α_e	γ_e	δ_e	v_{max}^{valid}	Dis. Prod.	Extrap.	Ref.
		Y_{00}	Y_{10}	Y_{20}	Y_{30}	Y_{40}	Y_{50}	Y_{01}	Y_{11}	Y_{21}	Y_{31}				
N_2															
$e'^1\Sigma$	115926.7		2216.2	-17.5				1.932	-0.0203			4	-	-	[102]
$y^1\Pi_g$	114305.3		1906.43	-37.51				1.739	-0.017			2	-	-	[57]
$x^1\Sigma_g^-$	113438	-0.261	1910	-20.7				1.75	-0.0225			2	-	-	[57]
$o3^1\Pi_u$	105878	4.236	1966.5	-10.88				1.7305	-2.75e-02			4	-	-	[58, 65, 103]
$H^3\Phi_u$	105720		924.21	-12.29	-0.173			1.0873	-0.0191			3	$N(^2D)+N(^2D)$	ER	[57, 58]
$b'^1\Sigma_u^+$	105215.381	0.289	759.31	-3.4044	0.017668	-1.7768e-3		1.1591	-0.01044	3.902e-4	-1.734e-5	28	$N(^2D)+N(^2P)$	ER	[58, 65, 103]
$c'4^1\Sigma_u^+$	104419	0.727	2166.7	-13.345	-0.2939			1.9285	-1.96e-2			8	-	-	[58, 65, 103]
$c_3^1\Pi_u$	104222	3.898	2198.4	-25.6				1.976	-3.80e-2			4	-	-	[58, 65, 103]
$D^3\Sigma_u^+$	103647.3		2206.67	-16.139	-1.668e-2	-2.152e-3	3.195e-5	1.9701	-1.821e-2	-1.087e-4	-1.44e-6	0	-	-	[104]
$b^1\Pi_u$	101660.029	6.531	641.76	21.67	-1.413	0.02286		1.387	-0.01424	-5.2132e-4		19	$N(^2D)+N(^2D)$	ER	[65, 68, 103]
$E^3\Sigma_g^+$	95858		2185					1.9273				2*	-	-	[57]
$C'^3\Pi$	98351		791	-33.5				1.0496				1*	-	-	[57]
$G^3\Delta_g$	89505		742.49	-11.85				0.928	-0.0161			5*	$N(^2D)+N(^4S)$	ER	[57, 58, 105]
$C^3\Pi$	89136.99	-1.785	2047.9540	-29.0044	2.25663	-0.55631		1.8268	-2.30e-2	1.90e-3	-6e-4	4*	-	-	[57, 106]
$C''^5\Pi_u$	88739.3		915.541	-12.567				1.08469	-0.0187			3	$N(^2D)+N(^4S)$	HH	[57, 107, 108]
$A'^5\Sigma$	75990.03	0.035286	742.1374	-12.994105	-1.0725			0.93054	-0.01713			4*	$N(^4S)+N(^4S)$	HH	[57, 109, 110]
$w^1\Delta_u$	72097.4	0.0105	1559.26	-11.63				1.498	-0.0166			11	$N(^2D)+N(^2D)$	ER	[57, 58]
$a^1\Pi_g$	69283.1	0.012	1694.2	-13.949	7.935e-3			1.6169	-1.793e-2	-2.93e-5		15	$N(^2D)+N(^2D)$	ER	[57, 58]
$a'^1\Sigma_u^-$	68152.66	0.0167	1530.254	-12.0747	0.04129	-0.00029		1.4799	-0.01657	2.41e-5		9	$N(^2D)+N(^2D)$	ER	[57, 58]
$B'^3\Sigma$	66272.47		1516.88	-12.181	0.04186	-0.000732		1.4733	-0.01666	9e-6		19	$N(^2P)+N(^4S)$	ER	[57, 58]
$W^3\Delta$	59805.575		1506.53	-12.575				1.47021	1.6997e-2			9	$N(^2D)+N(^4S)$	ER	[58, 111–114]
$B^3\Pi_g$	59619.35	-0.083	1734.025	-14.412	-3.30e-3	-7.90e-4	4.20e-5	1.63772	-1.793e-2	-1e4	5e-6	21	$N(^2D)+N(^4S)$	ER	[57, 65, 68, 115]
$A^3\Sigma$	50203.63	-0.189	1460.941	-13.980	2.40e-2	-2.56e-3		1.4539	-1.75e-2	-1.40e-4		16	$N(^4S)+N(^4S)$	HH	[57, 65, 68, 115]
$X^1\Sigma$	0		2358.55858	-14.3174587	-3.30799e-3	-1.94581e-4		1.998236	-1.73099e-2	-3.01203e-5	-6.927e-8	15	$N(^4S)+N(^4S)$	DPF [1]	[37, 57, 65, 116]

Table B.5: Updated spectroscopic database and other relevant data for reconstruction N_2^+ potential curves.

State	T(e) (cm^{-1})	Y_{00}	ω_e	$-\omega_e x_e$	$\omega_e y_e$	$\omega_e z_e$	$\omega_e a_e$	B_e	α_e	γ_e	δ_e	v_{max}^{valid}	Dis. Prod.	Extrap.	Ref.
		Y_{00}	Y_{10}	Y_{20}	Y_{30}	Y_{40}	Y_{50}	Y_{01}	Y_{11}	Y_{21}	Y_{31}				
N_2^+															
$C^2\Sigma_u^+$	64608	-1.803	2069.4	-8.3	-0.63	0.013		1.51	0.001	-0.0015	6.00e-05	6	$N(^2D)+N^+(^3P)$	HH	[57, 58, 65, 117, 118]
$D^2\Pi_g$	52814.06	0.167	911.7	-12.6	0.0555			1.113	-0.02			5	$N(^4S)+N^+(^3P)$	HH	[58]
$B^2\Sigma_u^+$	25461.26	-1.427	2421.14	-24.07	-0.3	-6.67e-02		2.08507	-0.0212	-5.00e-04	-8.80e-05	28	$N(^4S)+N^+(^3P)$	ER	[57, 58, 65, 117, 118]
$A^2\Pi_u$	9167.34	0.017	1903.7	-15.111	0.0112	-2.70e-04		1.7445	-0.0187	-6.00e-05	-1.10e-06	27	$N(^4S)+N^+(^3P)$	HH	[57, 58, 65, 117, 118]
$X^2\Sigma_g^+$	0	-0.12	2207.22	-16.226	4e-3	-6.1e-3	3.9e-4	1.93171	-1.8816e-2	-6.77e-5	-2.32e-6	21	$N(^4S)+N^+(^3P)$	HH	[57, 65, 117]

[1] The spectroscopic constants here reported are from [65] and are used for the RKR calculation. The subsequent extrapolation is performed by direct-potential-fit, fitting a Morse/long-range potential to the reconstructed RKR potential, by comparing observed transition energies to eigenvalue differences calculated from the radial Schrodinger equation. The fitting potential was determined, explained and recommended by Le Roy et al. [37], that reports the defining parameters that were then used in this work. Both potential curves (with spectroscopic data by [65] and with DPF by [37]) were plotted and presented very similar values, so both are legit reconstructions and it was opted for the DPF one.

Table B.6: Corresponding dissociation products and dissociation energies for O_2 molecule.

Dissociation Product	$O(^3P) + O(^3P)$	$O(^3P) + O(^1D)$
Dissociation Energy (cm^{-1})	42047	57915

Table B.7: Corresponding dissociation products and dissociation energies for O_2^+ molecule.

Dissociation Product	$O(^3P) + O^+(^4S)$	$O(^1D) + O^+(^4S)$	$O(3P) + O^+$(2D)
Dissociation Energy (cm^{-1})	54689	70557	83114

Table B.8: Corresponding dissociation products and dissociation energies for NO molecule.

Dissociation Product	$N(^4S) + O(^3P)$	$N(^2D) + O(^3P)$	$N(^2P) + O(^3P)$
Dissociation Energy (cm^{-1})	53344	72569	82184

Table B.9: Corresponding dissociation products and dissociation energies for NO^+ molecule.

Dissociation Product	$N(^4S) + O^+(^4S)$	$N^+(^3P) + O(^3P)$
Dissociation Energy (cm^{-1})	88700	96089

Table B.10: Corresponding dissociation products and dissociation energies for N_2 molecule.

Dissociation Product	$N(^4S) + N(^4S)$	$N(^2D) + N(^4S)$	$N(^2P) + N(^4S)$	$N(^2D) + N(^2D)$	$N(^2D) + N(^2P)$
Dissociation Energy (cm^{-1})	79886.68	99118	108730	118339	129402

Table B.11: Corresponding dissociation products and dissociation energies for N_2^+ molecule.

Dissociation Product	$N(^4S) + N^+(^3P)$	$N(^2D) + N^+(^3P)$
Dissociation Energy (cm^{-1})	71368	90594

B.2 Potential Curves

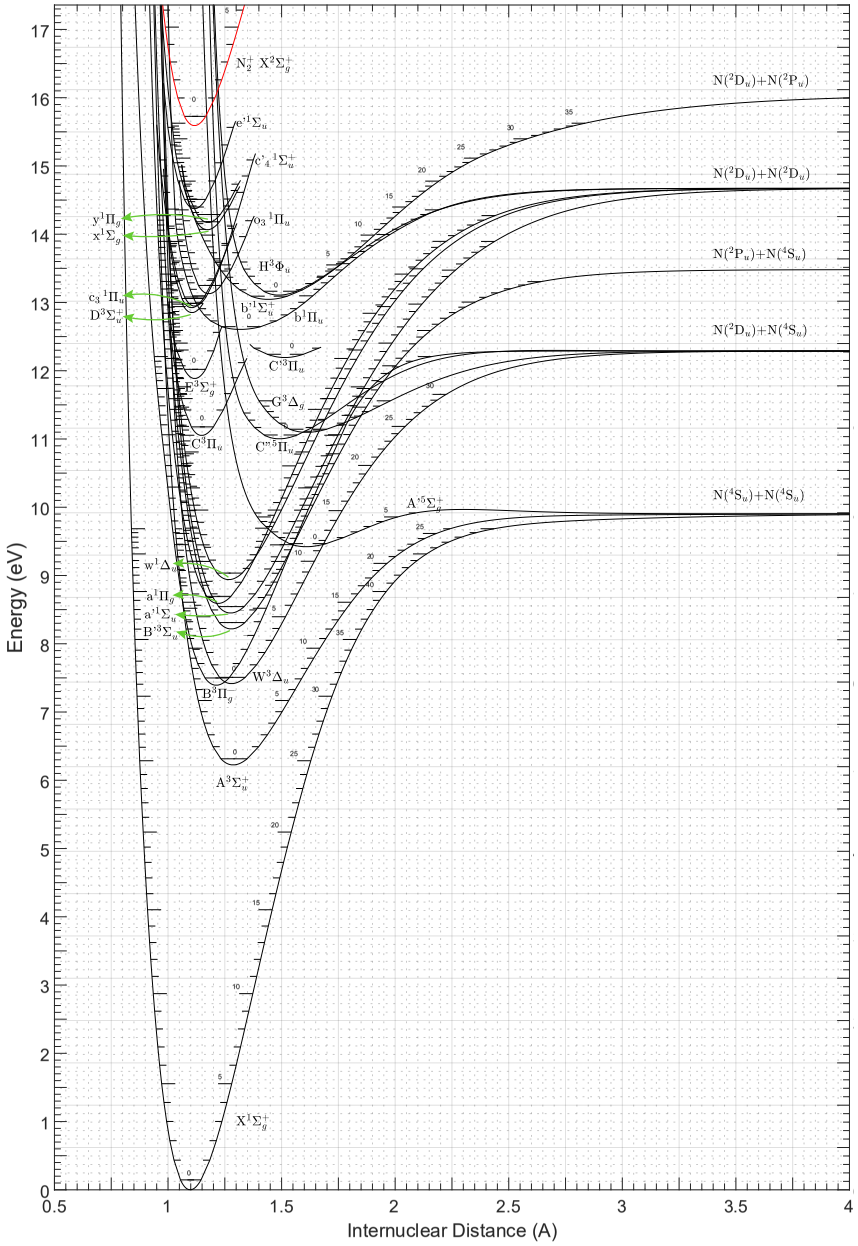

Figure B.1: Potential curves for N_2 states.

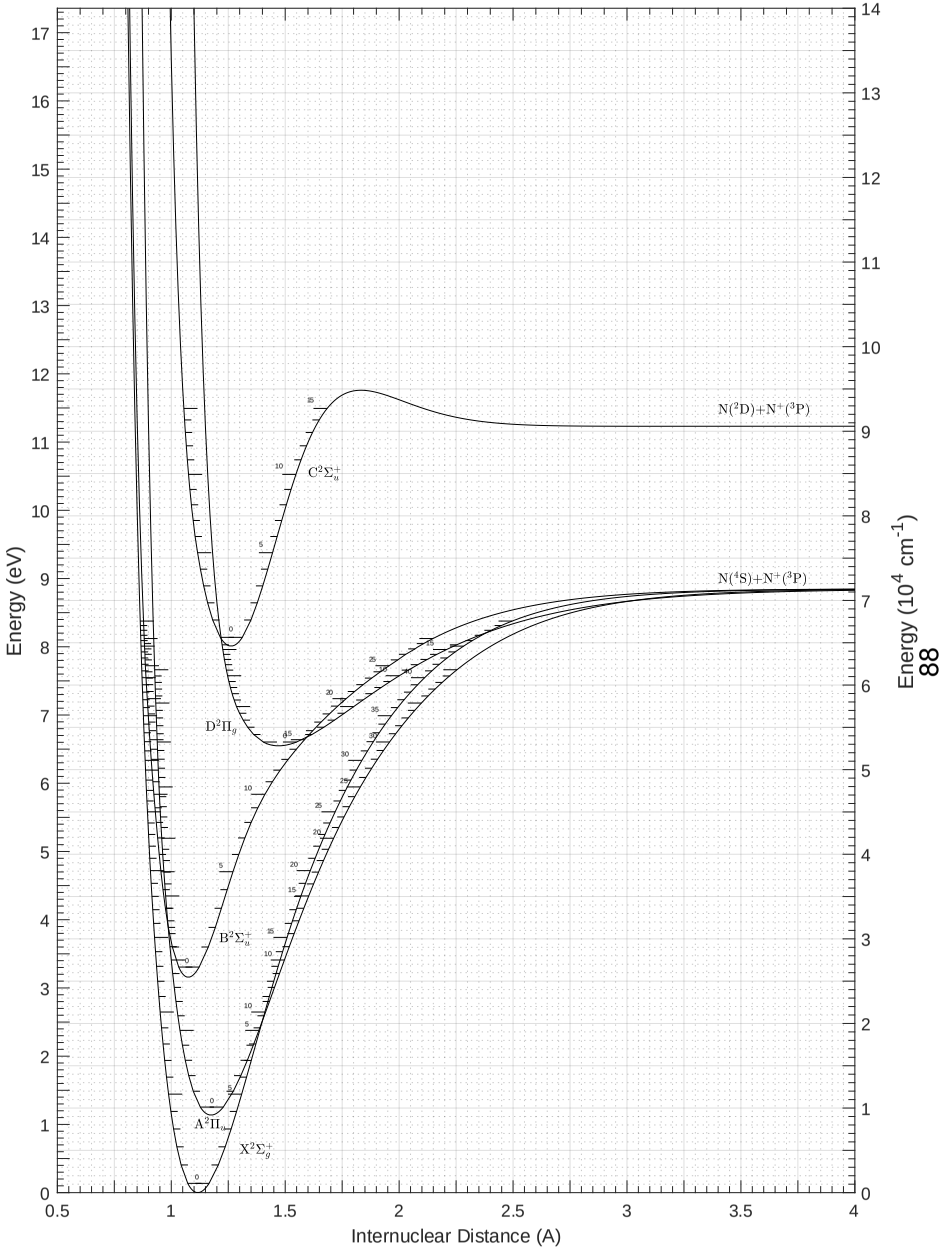

Figure B.2: Potential curves for N_2^+ states.

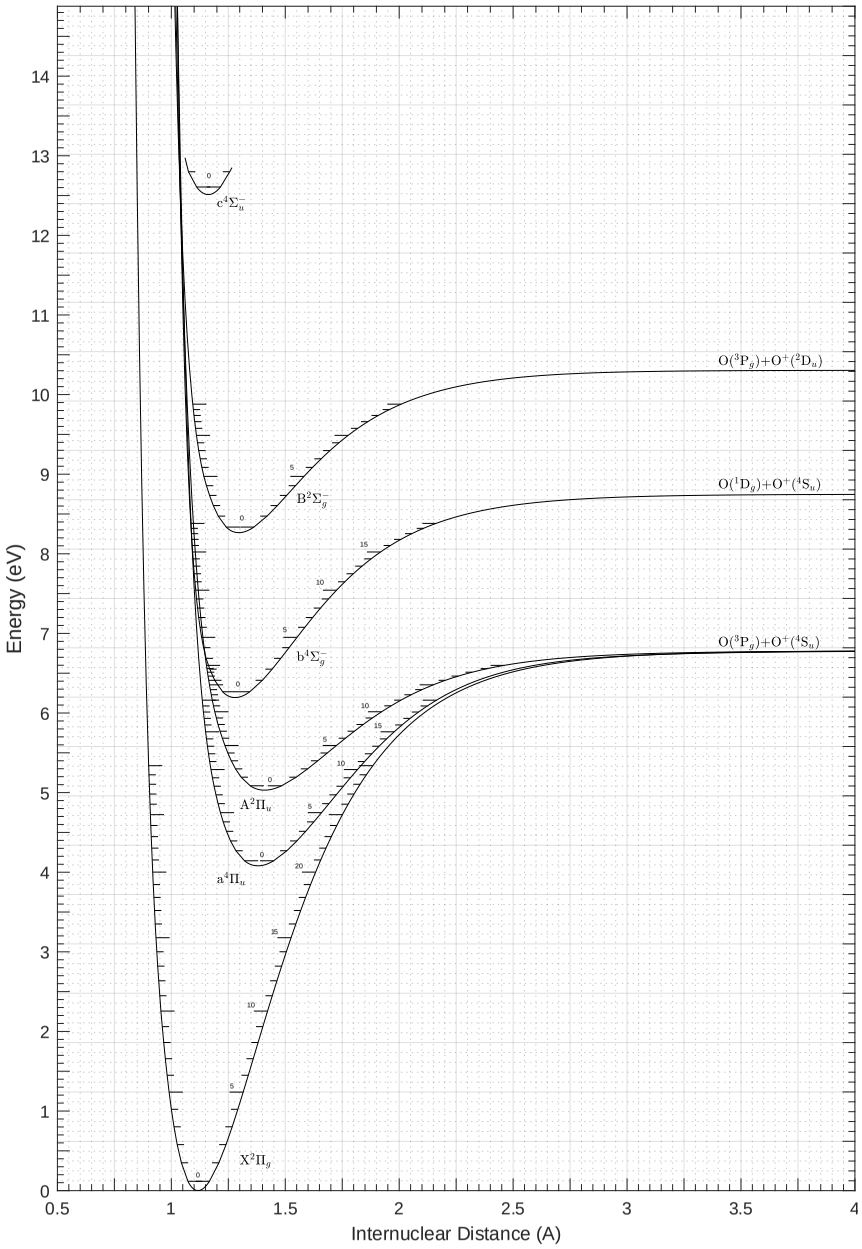

Figure B.3: Potential curves for O_2^+ states.

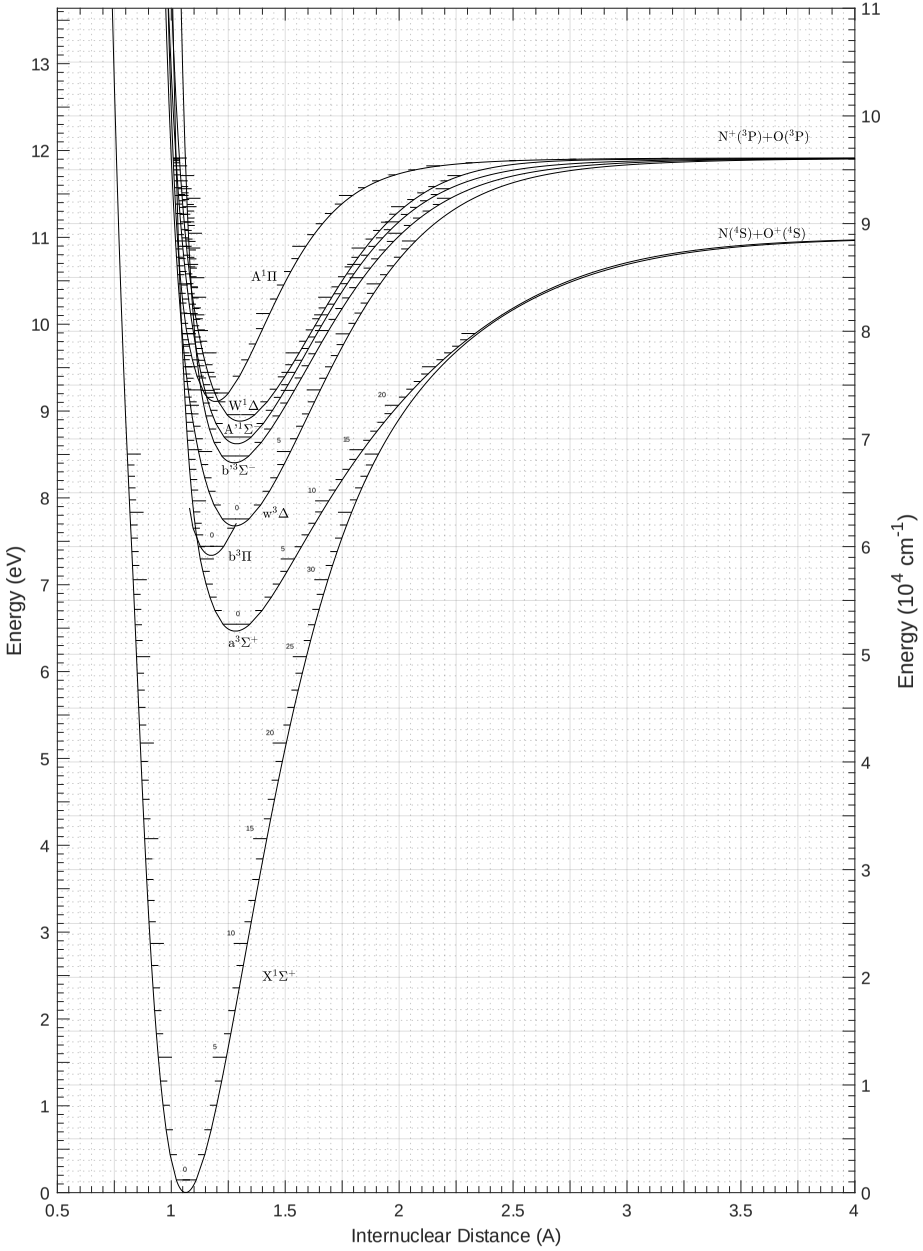

Figure B.4: Potential curves for NO^+ states.

B.3 Rovibrational Levels

Table B.12: Maximum vibrational and rotational quantum numbers found for each state of the O_2^+ molecule and number of rovibracional levels of each.

O_2^+	$X^2\Pi_g$	$a^4\Pi_u$	$A^2\Pi_u$	$b^4\Sigma_g^-$	$B^2\Sigma_g^-$	$c^4\Sigma_u^-$
v_{max}	55	38	29	32	27	1
J_{max}	196	151	122	134	120	39
No of rovibrational levels	7620	4015	2569	3121	2400	80

Table B.13: Maximum vibrational and rotational quantum numbers found for the first states of the N_2 molecule and number of rovibracional levels of each.

N_2	$X^1\Sigma$	$A^3\Sigma$	$B^3\Pi_g$	$W^3\Delta$	$B'^3\Sigma$	$a'^1\Sigma^u$	$a^1\Pi_g$	$w^1\Delta_u$
v_{max}	61	34	32	43	46	58	51	50
J_{max}	217	151	165	177	183	204	189	192
No of rovibrational levels	9008	3690	4183	5678	6284	8618	7034	7065

Table B.14: Maximum vibrational and rotational quantum numbers found for other states of the N_2 molecule and number of rovibracional levels of each.

N_2	$D^3\Sigma_u^+$	$b^1\Pi_u$	$E^3\Sigma_g^+$	$C'^3\Pi$	$G^3\Delta_g$	$C^3\Pi$	$C''^5\Pi_u$	$A'^5\Sigma$
v_{max}	0	28	2	1	20	4	15	7
J_{max}	33	121	70	40	107	70	102	66
No of rovibrational levels	34	2618	213	82	1684	355	1322	455

Table B.15: Maximum vibrational and rotational quantum numbers found for more states of the N_2 molecule and number of rovibracional levels of each.

N_2	$c_3^1\Pi_u$	$c'4^1\Sigma_u^+$	$b'^1\Sigma_u^+$	$H^3\Phi_u$	$o3^1\Pi_u$	$x^1\Sigma_g^-$	$y^1\Pi_g$	$e'^1\Sigma$
v_{max}	4	8	54	21	4	2	2	4
J_{max}	88	119	162	113	92	54	52	93
No of rovibrational levels	445	1071	6059	1861	465	165	159	470

Table B.16: Maximum vibrational and rotational quantum numbers found for each state of the N_2^+ molecule and number of rovibracional levels of each.

N_2^+	$X^2\Sigma_g^+$	$A^2\Pi_u$	$B^2\Sigma_u^+$	$D^2\Pi_g$	$C^2\Sigma_u^+$
v_{max}	64	64	48	39	17
J_{max}	208	206	155	140	135
No of rovibrational levels	9449	9531	5403	3999	2084

Table B.17: Maximum vibrational and rotational quantum numbers found for the first states of the NO molecule and number of rovibracional levels of each.

NO	$X^2\Pi_r$	$a^4\Pi_i$	$A^2\Sigma^+$	$B^2\Pi_r$	$b^4\Sigma^-$	$C^2\Pi_r$	$D^2\Sigma^+$	$L'^2\Phi$
v_{max}	49	19	8	12	26	2	5	1
J_{max}	190	119	124	167	133	103	101	137
No of rovibrational levels	6501	1829	1117	2184	2664	312	612	276

Table B.18: Maximum vibrational and rotational quantum numbers found for other states of the NO molecule and number of rovibracional levels of each.

NO	$B'^2\Delta_i$	$E^2\Sigma^+$	$F^2\Delta$	$H^2\Sigma^+$	$H'^2\Pi$	$G^2\Sigma^-$	$L^2\Pi$
v_{max}	13	4	4	2	2	10	27
J_{max}	99	79	75	72	72	91	142
No of rovibrational levels	1075	400	380	219	219	846	3013

Table B.19: Maximum vibrational and rotational quantum numbers found for each state of the NO^+ molecule and number of rovibracional levels of each.

NO^+	$X^1\Sigma^+$	$a^3\Sigma^+$	$b^3\Pi$	$w^3\Delta$	$b'^3\Sigma^-$	$A'^1\Sigma^-$	$W^1\Delta$	$A^1\Pi$
v_{max}	83	58	1	46	39	37	33	25
J_{max}	230	181	160	171	154	149	145	125
No of rovibrational levels	13040	7706	322	5538	4298	3868	3437	2216

B.4 Updated Thermodynamic Database

The following database presents the curve-fit coefficients for air species' thermodynamic properties computed in this work. The coefficients follow the convention used by Gordon and McBride [55] and equations 3.2, 3.3, 3.4, for temperatures up to 100 000 K.

```
e-               Ref-Species. JANAF 1985 3/82.
 4 g12/98 E   1.00    0.00    0.00    0.00    0.00 0.000548579903          0.000
    298.150   1000.0007 -2.0 -1.0  0.0  1.0  2.0  3.0  4.0  0.0         6197.428
 0.000000000D+00 0.000000000D+00 2.500000000D+00 0.000000000D+00 0.000000000D+00
 0.000000000D+00 0.000000000D+00               -7.453750000D+02-1.172081224D+01
   1000.000   6000.0007 -2.0 -1.0  0.0  1.0  2.0  3.0  4.0  0.0         6197.428
 0.000000000D+00 0.000000000D+00 2.500000000D+00 0.000000000D+00 0.000000000D+00
 0.000000000D+00 0.000000000D+00               -7.453750000D+02-1.172081224D+01
   6000.000  20000.0007 -2.0 -1.0  0.0  1.0  2.0  3.0  4.0  0.0         6197.428
 0.000000000D+00 0.000000000D+00 2.500000000D+00 0.000000000D+00 0.000000000D+00
 0.000000000D+00 0.000000000D+00               -7.453750000D+02-1.172081224D+01
 20000.000  100000.0007 -2.0 -1.0  0.0  1.0  2.0  3.0  4.0  0.0         6197.428
 0.000000000D+00 0.000000000D+00 2.500000000D+00 0.000000000D+00 0.000000000D+00
 0.000000000D+00 0.000000000D+00               -7.453750000D+02-1.172081224D+01
N                RossDaG  (28/08/2021) (28/08/2021)
 9 g 5/97 N   1.00    0.00    0.00    0.00    0.00 0   14.0067000     472679.964
     50.000    200.0007 -2.0 -1.0  0.0  1.0  2.0  3.0  4.0  0.0         6197.392
 -0.10001905D+04  0.53476178D+02  0.14434470D+01  0.99370035D-02 -0.49890970D-04
  0.13384371D-06 -0.15528576D-09                 0.55918755D+05  0.87496279D+01
    200.000   1000.0007 -2.0 -1.0  0.0  1.0  2.0  3.0  4.0  0.0         6197.392
 -0.19636376D+05  0.34365615D+03  0.15948269D+00  0.78719163D-02 -0.13740566D-04
  0.11819395D-07 -0.39327601D-11                 0.54528925D+05  0.16725292D+02
   1000.000  10000.0007 -2.0 -1.0  0.0  1.0  2.0  3.0  4.0  0.0         6197.392
  0.18564143D+07 -0.48673220D+04  0.72228912D+01 -0.21147169D-02  0.43998684D-06
 -0.36858266D-10  0.10927144D-14                 0.87781488D+05 -0.30474980D+02
  10000.000  20000.0007 -2.0 -1.0  0.0  1.0  2.0  3.0  4.0  0.0         6197.392
 -0.52088974D+10  0.25099911D+07 -0.50813048D+03  0.56181619D-01 -0.34693793D-05
  0.11275438D-09 -0.14737184D-14                -0.20376860D+08  0.45105872D+04
  20000.000  40000.0007 -2.0 -1.0  0.0  1.0  2.0  3.0  4.0  0.0         6197.392
  0.97963504D+11 -0.15361185D+08  0.78955479D+03 -0.91650686D-02 -0.40912091D-06
  0.13012068D-10 -0.10677201D-15                 0.14383852D+09 -0.81994323D+04
  40000.000  60000.0007 -2.0 -1.0  0.0  1.0  2.0  3.0  4.0  0.0         6197.392
  0.13324598D+13 -0.16100759D+09  0.81296517D+04 -0.21823151D+00  0.32831925D-05
 -0.26228217D-10  0.86914498D-16                 0.15340897D+10 -0.83113165D+05
  60000.000  75000.0007 -2.0 -1.0  0.0  1.0  2.0  3.0  4.0  0.0         6197.392
  0.90397237D+13 -0.84069869D+09  0.32517179D+05 -0.66911564D+00  0.77266286D-05
 -0.47469988D-10  0.12122397D-15                 0.82324733D+10 -0.34121180D+06
  75000.000  85000.0007 -2.0 -1.0  0.0  1.0  2.0  3.0  4.0  0.0         6197.392
 -0.39467958D-06 -0.13230580D-06  0.16915621D-06 -0.24231899D-07  0.31082943D-08
 -0.55230251D-13  0.27047141D-18                 0.26462413D+06  0.35025384D+02
  85000.000 100000.0007 -2.0 -1.0  0.0  1.0  2.0  3.0  4.0  0.0         6197.392
 -0.70857394D-07 -0.50841269D-07  0.12338865D-06 -0.80219204D-07  0.21413637D-08
 -0.32455696D-13  0.13645995D-18                 0.28447682D+06  0.35609910D+02
N+               RossDaG  (28/08/2021) (28/08/2021)
 7 g 6/97 N   1.00E- -1.00    0.00    0.00    0.00 0   14.0061514    1882127.587
     50.000   1000.0007 -2.0 -1.0  0.0  1.0  2.0  3.0  4.0  0.0         7116.487
 -0.24126565D+04  0.14109585D+03  0.15392118D+01  0.31368827D-02 -0.52185045D-05
  0.42370454D-08 -0.13274081D-11                 0.22499595D+06  0.10157846D+02
   1000.000   6000.0007 -2.0 -1.0  0.0  1.0  2.0  3.0  4.0  0.0         7116.487
  0.38609506D+06 -0.11141921D+04  0.37488770D+01 -0.67046657D-03  0.17400905D-06
 -0.19201027D-10  0.78917535D-15                 0.23275061D+06 -0.39692222D+01
   6000.000  20000.0007 -2.0 -1.0  0.0  1.0  2.0  3.0  4.0  0.0         7116.487
 -0.31192181D+07  0.99615676D+03  0.19692352D+01  0.18156450D-03 -0.16007393D-07
  0.65446433D-12 -0.95083142D-17                 0.21763878D+06  0.89531250D+01
  20000.000  50000.0007 -2.0 -1.0  0.0  1.0  2.0  3.0  4.0  0.0         7116.487
  0.94879043D+10 -0.19352836D+07  0.16105179D+03 -0.65410122D-02  0.14046191D-06
 -0.14013447D-11  0.49551812D-17                 0.17686701D+08 -0.15434078D+04
  50000.000  60000.0007 -2.0 -1.0  0.0  1.0  2.0  3.0  4.0  0.0         7116.487
  0.73638051D+14 -0.80612724D+10  0.36740443D+06 -0.89238829D+01  0.12184066D-03
 -0.88658571D-09  0.26860101D-14                 0.77619701D+11 -0.37950610D+07
  60000.000  90000.0007 -2.0 -1.0  0.0  1.0  2.0  3.0  4.0  0.0         7116.487
 -0.62857461D+11  0.17818897D+07  0.25090056D-06 -0.50024494D-06 -0.36625582D-08
  0.42268139D-13 -0.12990812D-18                -0.20034184D+08  0.59949571D+02
  90000.000 100000.0007 -2.0 -1.0  0.0  1.0  2.0  3.0  4.0  0.0         7116.487
 -0.14385109D-07  0.11324864D-06  0.13556014D-08  0.15543993D-07  0.55262492D-08
 -0.90194348D-13  0.39025515D-18                 0.31469940D+06  0.30426205D+02
N++              RossDaG  (28/08/2021) (28/08/2021)
 9 g 5/97 N   1.00E   2.00    0.00    0.00    0.00 0   14.0067000    3334049.815
     50.000    300.0007 -2.0 -1.0  0.0  1.0  2.0  3.0  4.0  0.0         7163.250
  0.74690137D+04 -0.49694178D+03  0.13346448D+02 -0.87112307D-01  0.34715011D-03
 -0.69068658D-06  0.54812727D-09                 0.40178236D+06 -0.43362755D+02
    300.000   4000.0007 -2.0 -1.0  0.0  1.0  2.0  3.0  4.0  0.0         7163.250
  0.12741804D+05  0.21795950D+02  0.24439249D+01  0.62406153D-04 -0.33591311D-07
  0.84809562D-11 -0.79942199D-15                 0.40018145D+06  0.49458381D+01
   4000.000  20000.0007 -2.0 -1.0  0.0  1.0  2.0  3.0  4.0  0.0         7163.250
  0.12177418D+08 -0.94961891D+04  0.53141526D+01 -0.38977127D-03  0.24443559D-07
 -0.52169630D-12  0.25227418D-17                 0.47347562D+06 -0.19374160D+02
  20000.000  40000.0007 -2.0 -1.0  0.0  1.0  2.0  3.0  4.0  0.0         7163.250
  0.11980333D+10 -0.19886212D+06  0.13923906D+02 -0.28414483D-03  0.62936466D-08
 -0.10957435D-12  0.92503330D-18                 0.22477687D+07 -0.11214435D+03
  40000.000  50000.0007 -2.0 -1.0  0.0  1.0  2.0  3.0  4.0  0.0         7163.250
 -0.56128669D+12  0.74960114D+08 -0.41686929D+04  0.12385908D+00 -0.20677351D-05
  0.18400087D-10 -0.68100714D-16                -0.70644306D+09  0.42255514D+05
  50000.000  60000.0007 -2.0 -1.0  0.0  1.0  2.0  3.0  4.0  0.0         7163.250
 -0.95710955D+12  0.10566277D+09 -0.48552676D+04  0.11919549D+00 -0.16463089D-05
  0.12147405D-10 -0.37372761D-16                -0.10161074D+10  0.50137901D+05
  60000.000  80000.0007 -2.0 -1.0  0.0  1.0  2.0  3.0  4.0  0.0         7163.250
  0.56173292D+12 -0.50528438D+08  0.19041937D+04 -0.38211687D-01  0.43152905D-06
 -0.25769291D-11  0.63382702D-17                 0.49670778D+09 -0.19999753D+05
  80000.000  90000.0007 -2.0 -1.0  0.0  1.0  2.0  3.0  4.0  0.0         7163.250
  0.23663465D-06  0.85853365D-07 -0.72254516D-07 -0.17677273D-07  0.24804933D-08
 -0.25380412D-13  0.62475091D-19                 0.49856189D+06  0.30720525D+02
  90000.000 100000.0007 -2.0 -1.0  0.0  1.0  2.0  3.0  4.0  0.0         7163.250
 -0.10459050D-06  0.25211180D-07  0.68982506D-07 -0.32171399D-07  0.26459716D-08
 -0.29052340D-13  0.82868132D-19                 0.49455438D+06  0.30609423D+02
N+++             RossDaG  (28/08/2021) (28/08/2021)
11 g 5/97 N   1.00E   3.00    0.00    0.00    0.00 0   14.0067000    5054773.126
     50.000   1000.0007 -2.0 -1.0  0.0  1.0  2.0  3.0  4.0  0.0         6197.392
 -0.31285004D+02  0.10020345D+01  0.24921348D+01  0.26266014D-04 -0.45223065D-07
  0.40712556D-10 -0.14870384D-13                 0.60719982D+06  0.28361030D+01
   1000.000  10000.0007 -2.0 -1.0  0.0  1.0  2.0  3.0  4.0  0.0         6197.392
  0.30676888D+05 -0.84525558D+02  0.25883620D+01 -0.44757027D-04  0.11656242D-07
 -0.14970199D-11  0.75093531D-16                 0.60774922D+06  0.21541321D+01
  10000.000  20000.0007 -2.0 -1.0  0.0  1.0  2.0  3.0  4.0  0.0         6197.392
  0.69585568D+09 -0.35074281D+06  0.74380302D+02 -0.75472119D-02  0.41684383D-06
 -0.11049004D-10  0.11243493D-15                 0.34522879D+07 -0.63280496D+03
  20000.000  30000.0007 -2.0 -1.0  0.0  1.0  2.0  3.0  4.0  0.0         6197.392
 -0.64479391D+10  0.19785821D+07 -0.23795602D+03  0.14566371D-01 -0.45685767D-06
  0.72406505D-11 -0.46182087D-16                -0.16449533D+08  0.22579913D+04
```

```
  30000.000  40000.0007 -2.0 -1.0  0.0  1.0  2.0  3.0  4.0  0.0        6197.392
  0.15450268D+11 -0.28640839D+07  0.20540610D+03 -0.69749803D-02  0.12959562D-06
 -0.12489748D-11  0.49057974D-17                 0.26788748D+08 -0.20134665D+04
  40000.000  50000.0007 -2.0 -1.0  0.0  1.0  2.0  3.0  4.0  0.0        6197.392
  0.21232393D+12 -0.29297476D+08  0.16825288D+04 -0.50965555D-01  0.86641089D-06
 -0.78354251D-11  0.29482923D-16                 0.27591641D+09 -0.16970356D+05
  50000.000  60000.0007 -2.0 -1.0  0.0  1.0  2.0  3.0  4.0  0.0        6197.392
 -0.54346431D+13  0.60127376D+09 -0.27688104D+05  0.67970087D+00 -0.93772854D-05
  0.68937747D-10 -0.21095419D-15                -0.57825754D+10  0.28574351D+06
  60000.000  70000.0007 -2.0 -1.0  0.0  1.0  2.0  3.0  4.0  0.0        6197.392
  0.11672673D+15 -0.10870640D+11  0.42155829D+06 -0.87130241D+01  0.10123311D-03
 -0.62689273D-09  0.16165086D-14                 0.10642705D+12 -0.44224983D+07
  70000.000  80000.0007 -2.0 -1.0  0.0  1.0  2.0  3.0  4.0  0.0        6197.392
  0.30112678D+10 -0.31403509D-06  0.12298543D-06  0.25986218D-06  0.30756746D-08
 -0.55763220D-13  0.30601363D-18                 0.79902733D+06  0.30666696D+02
  80000.000  90000.0007 -2.0 -1.0  0.0  1.0  2.0  3.0  4.0  0.0        6197.392
  0.19498271D-06 -0.22706855D-06  0.52863872D-07  0.61382814D-07  0.29555344D-08
 -0.47152883D-13  0.22903208D-18                 0.74480631D+06  0.30150562D+02
  90000.000 100000.0007 -2.0 -1.0  0.0  1.0  2.0  3.0  4.0  0.0        6197.392
  0.12172525D-07 -0.14291585D-07  0.21871509D-07  0.14356004D-07  0.17851462D-08
 -0.21126838D-13  0.84410691D-19                 0.77303089D+06  0.30942691D+02
0                RossDaG  (28/08/2021) (28/08/2021)
11 g 5/97 0   1.00    0.00    0.00    0.00    0.00 0   15.9994000     249174.965
     50.000    200.0007 -2.0 -1.0  0.0  1.0  2.0  3.0  4.0  0.0        6725.365
  0.19463595D+04 -0.10607565D+03  0.39927169D+01  0.46461730D-02 -0.12409209D-03
  0.59423125D-06 -0.93512099D-09                 0.29539299D+05 -0.30317277D+01
    200.000   2000.0007 -2.0 -1.0  0.0  1.0  2.0  3.0  4.0  0.0        6725.365
 -0.34820118D+04  0.10083444D+03  0.22697530D+01  0.26599963D-03 -0.15473355D-06
  0.40610640D-10 -0.32494804D-14                 0.28695407D+05  0.66715268D+01
   2000.000  10000.0007 -2.0 -1.0  0.0  1.0  2.0  3.0  4.0  0.0        6725.365
 -0.17867468D+07  0.25227929D+04  0.13122821D+01  0.17887909D-03  0.10282349D-07
 -0.28292826D-11  0.12581432D-15                 0.11196003D+05  0.14883788D+02
  10000.000  20000.0007 -2.0 -1.0  0.0  1.0  2.0  3.0  4.0  0.0        6725.365
 -0.12527986D+10  0.70088463D+06 -0.16034201D+03  0.20039986D-01 -0.13565496D-05
  0.47200861D-10 -0.63716462D-15                -0.55767730D+07  0.14223172D+04
  20000.000  30000.0007 -2.0 -1.0  0.0  1.0  2.0  3.0  4.0  0.0        6725.365
 -0.23852792D+12  0.59155030D+08 -0.59599823D+04  0.31074988D+00 -0.87912853D-05
  0.12836914D-09 -0.75922144D-15                -0.52183226D+09  0.56946278D+05
  30000.000  40000.0007 -2.0 -1.0  0.0  1.0  2.0  3.0  4.0  0.0        6725.365
  0.29131767D+12 -0.54660795D+08  0.40697114D+04 -0.15440636D+00  0.32000138D-05
 -0.34669773D-10  0.15438182D-15                 0.49823429D+09 -0.40107912D+05
  40000.000  60000.0007 -2.0 -1.0  0.0  1.0  2.0  3.0  4.0  0.0        6725.365
 -0.22067671D+12  0.26258738D+08 -0.12432096D+04  0.31151685D-01 -0.43700051D-06
  0.32708725D-11 -0.10216298D-16                -0.25129131D+09  0.12837393D+05
  60000.000  70000.0007 -2.0 -1.0  0.0  1.0  2.0  3.0  4.0  0.0        6725.365
  0.82541836D+14 -0.76959392D+10  0.29881613D+06 -0.61840220D+01  0.71942742D-04
 -0.44608676D-09  0.11517416D-14                 0.75336099D+11 -0.31344380D+07
  70000.000  80000.0007 -2.0 -1.0  0.0  1.0  2.0  3.0  4.0  0.0        6725.365
  0.39713952D+10 -0.99358060D-06  0.36103552D-06  0.37580569D-06  0.20828456D-08
 -0.36930075D-13  0.18682744D-18                 0.31949091D+06  0.36219872D+02
  80000.000  90000.0007 -2.0 -1.0  0.0  1.0  2.0  3.0  4.0  0.0        6725.365
 -0.36237043D-07  0.14144880D-06 -0.31956216D-07  0.59501229D-09  0.27065756D-08
 -0.45075600D-13  0.20707162D-18                 0.23474220D+06  0.35126561D+02
  90000.000 100000.0007 -2.0 -1.0  0.0  1.0  2.0  3.0  4.0  0.0        6725.365
 -0.14922400D-07  0.40266115D-07 -0.37614100D-08  0.93199892D-08  0.19668251D-08
 -0.28639931D-13  0.11576805D-18                 0.25270787D+06  0.35625505D+02
0+               RossDaG  (28/08/2021) (28/08/2021)
 9 g 8/97 0   1.00E- -1.00    0.00    0.00    0.00    0.00 0   15.9988514    1568787.192
     50.000    5000.0007 -2.0 -1.0  0.0  1.0  2.0  3.0  4.0  0.0        6197.392
  0.27033742D+02 -0.71545058D+00  0.25046806D+01 -0.90353873D-05  0.79757793D-08
 -0.33813688D-11  0.53071449D-15                 0.18793947D+06  0.43536514D+01
   5000.000  10000.0007 -2.0 -1.0  0.0  1.0  2.0  3.0  4.0  0.0        6197.392
 -0.10353379D+09  0.79011066D+05 -0.20802113D+02  0.32902172D-02 -0.23348094D-06
  0.97990898D-11 -0.20786468D-15                -0.42196972D+06  0.20268196D+03
  10000.000  20000.0007 -2.0 -1.0  0.0  1.0  2.0  3.0  4.0  0.0        6197.392
  0.29609702D+09 -0.79614083D+05  0.45228677D+01  0.10696885D-02 -0.97574360D-07
  0.32684375D-11 -0.39213938D-16                 0.90441303D+06 -0.27268880D+02
  20000.000  30000.0007 -2.0 -1.0  0.0  1.0  2.0  3.0  4.0  0.0        6197.392
 -0.73669514D+10  0.17860617D+07 -0.17745386D+03  0.99144100D-02 -0.30823677D-06
  0.50534697D-11 -0.33333908D-16                -0.15598244D+08  0.17188831D+04
  30000.000  50000.0007 -2.0 -1.0  0.0  1.0  2.0  3.0  4.0  0.0        6197.392
  0.59716490D+11 -0.95980802D+07  0.63391696D+03 -0.21356743D-01  0.38444565D-06
 -0.33825976D-11  0.11181732D-16                 0.88985160D+08 -0.62943654D+04
  50000.000  70000.0007 -2.0 -1.0  0.0  1.0  2.0  3.0  4.0  0.0        6197.392
 -0.10036003D+13  0.10851148D+09 -0.47854786D+04  0.10978865D+00 -0.13743177D-05
  0.89421521D-11 -0.23766136D-16                -0.10469537D+10  0.49674080D+05
  70000.000  80000.0007 -2.0 -1.0  0.0  1.0  2.0  3.0  4.0  0.0        6197.392
  0.70960901D+15 -0.57254812D+11  0.19237429D+07 -0.34453898D+02  0.34691707D-03
 -0.18620562D-08  0.41622996D-14                 0.56875056D+12 -0.20457501D+08
  80000.000  90000.0007 -2.0 -1.0  0.0  1.0  2.0  3.0  4.0  0.0        6197.392
 -0.48425128D-06  0.59521947D-06  0.95341275D-07 -0.15033185D-06  0.92517041D-08
 -0.16413419D-12  0.76568808D-18                 0.19018673D+06  0.27700308D+02
  90000.000 100000.0007 -2.0 -1.0  0.0  1.0  2.0  3.0  4.0  0.0        6197.392
 -0.62364170D-07  0.13408513D-06  0.33141709D-07 -0.42896459D-07  0.73048470D-08
 -0.12091049D-12  0.52562732D-18                 0.23736810D+06  0.29009648D+02
0++              RossDaG  (28/08/2021) (28/08/2021)
 8 g 5/97 0   1.00E   2.00    0.00    0.00    0.00 0   15.9994000    3643354.521
     50.000    200.0007 -2.0 -1.0  0.0  1.0  2.0  3.0  4.0  0.0        7881.441
 -0.73862580D+04  0.37104566D+03 -0.47654924D+01  0.10975509D+00 -0.79089560D-03
  0.26938849D-05 -0.35463393D-08                 0.43592028D+06  0.33210268D+02
    200.000   1000.0007 -2.0 -1.0  0.0  1.0  2.0  3.0  4.0  0.0        7881.441
 -0.19005518D+05  0.45151919D+03  0.72167470D+00  0.37410879D-02 -0.43935261D-05
  0.27119415D-08 -0.68469582D-12                 0.43521087D+06  0.15625600D+02
   1000.000   6000.0007 -2.0 -1.0  0.0  1.0  2.0  3.0  4.0  0.0        7881.441
  0.48913037D+05 -0.25122024D+02  0.24762335D+01  0.53960838D-04 -0.31752885D-07
  0.72354944D-11 -0.47222720D-15                 0.43774572D+06  0.52996083D+01
   6000.000  20000.0007 -2.0 -1.0  0.0  1.0  2.0  3.0  4.0  0.0        7881.441
  0.31896614D+08 -0.16508449D+05  0.54409928D+01 -0.21601790D-03  0.10693993D-07
 -0.29894849D-12  0.38745683D-17                 0.57216622D+06 -0.21553199D+02
  20000.000  40000.0007 -2.0 -1.0  0.0  1.0  2.0  3.0  4.0  0.0        7881.441
 -0.75164980D+10  0.16640904D+07 -0.14879886D+03  0.72763765D-02 -0.19408496D-06
  0.27404368D-11 -0.15940959D-16                -0.14425542D+08  0.14643492D+04
  40000.000  60000.0007 -2.0 -1.0  0.0  1.0  2.0  3.0  4.0  0.0        7881.441
  0.33972930D+13 -0.42447515D+09  0.21999683D+05 -0.60513109D+00  0.93205741D-05
 -0.76205994D-10  0.25843748D-15                 0.40322503D+10 -0.22443134D+06
  60000.000  80000.0007 -2.0 -1.0  0.0  1.0  2.0  3.0  4.0  0.0        7881.441
 -0.32700903D-04 -0.28058283D-04 -0.27379814D-04  0.61909104D-04  0.39004028D-09
 -0.90316264D-14  0.52362907D-19                 0.50352682D+06  0.29845386D+02
  80000.000 100000.0007 -2.0 -1.0  0.0  1.0  2.0  3.0  4.0  0.0        7881.441
```

```
  0.10961678D-06  0.18937136D-07  0.41084812D-07 -0.25823661D-06  0.16423870D-08
 -0.11199567D-13  0.51893518D-20                 0.54184164D+06  0.31664006D+02
O+++             RossDaG  (28/08/2021) (28/08/2021)
11 g 5/97 O   1.00E   3.00    0.00    0.00    0.00 0   15.9994000    5554565.633
     50.000    500.0007 -2.0 -1.0  0.0  1.0  2.0  3.0  4.0  0.0         7291.572
  0.98874818D+04 -0.31053332D+03  0.44014730D+01  0.10478462D-01 -0.73998095D-04
  0.14634744D-06 -0.96891235D-10                 0.66849543D+06 -0.83575674D+01
    500.000   6000.0007 -2.0 -1.0  0.0  1.0  2.0  3.0  4.0  0.0         7291.572
  0.52830234D+05  0.78311010D+02  0.24075102D+01  0.50413687D-04 -0.14004268D-07
  0.19125309D-11 -0.10150009D-15                 0.66706370D+06  0.54475234D+01
   6000.000  20000.0007 -2.0 -1.0  0.0  1.0  2.0  3.0  4.0  0.0         7291.572
  0.16859499D+08 -0.94332507D+04  0.44843813D+01 -0.18331735D-03  0.56189787D-08
  0.11619084D-12 -0.46666906D-17                 0.74337526D+06 -0.12824951D+02
  20000.000  20000.0007 -2.0 -1.0  0.0  1.0  2.0  3.0  4.0  0.0         7291.572
  0.14846176D+18 -0.19193337D+14 -0.53461149D+10  0.44761367D+05  0.16959011D+02
  0.96287208D-03 -0.59044881D-07                 0.24952390D+15  0.47678199D+11
  20000.000  30000.0007 -2.0 -1.0  0.0  1.0  2.0  3.0  4.0  0.0         7291.572
  0.67501681D+10 -0.16304162D+07  0.16706090D+03 -0.89354800D-02  0.27551038D-06
 -0.44892213D-11  0.30141763D-16                 0.15074557D+08 -0.15635782D+04
  30000.000  40000.0007 -2.0 -1.0  0.0  1.0  2.0  3.0  4.0  0.0         7291.572
 -0.18681574D+11  0.32813837D+07 -0.23804400D+03  0.93459543D-02 -0.20032154D-06
  0.22700218D-11 -0.10670780D-16                -0.29370090D+08  0.23753396D+04
  40000.000  60000.0007 -2.0 -1.0  0.0  1.0  2.0  3.0  4.0  0.0         7291.572
  0.69585280D+10 -0.83775759D+06  0.41466735D+02 -0.87781648D-03  0.11725150D-07
 -0.89310058D-13  0.31210664D-18                 0.86799152D+07 -0.39888274D+03
  60000.000  70000.0007 -2.0 -1.0  0.0  1.0  2.0  3.0  4.0  0.0         7291.572
 -0.36331294D+14  0.33902257D+10 -0.13172528D+06  0.27280029D+01 -0.31756823D-04
  0.19702699D-09 -0.50896368D-15                -0.33183876D+11  0.13816910D+07
  70000.000  85000.0007 -2.0 -1.0  0.0  1.0  2.0  3.0  4.0  0.0         7291.572
  0.52408449D+10 -0.53517729D-06  0.13690890D-06  0.39991175D-06  0.15672764D-08
 -0.21225535D-13  0.95162017D-19                 0.88580574D+06  0.32452628D+02
  85000.000  90000.0007 -2.0 -1.0  0.0  1.0  2.0  3.0  4.0  0.0         7291.572
 -0.22596219D-07 -0.12301390D-06  0.81334609D-07 -0.37987056D-07  0.28668335D-08
 -0.44534595D-13  0.20412489D-18                 0.76719255D+06  0.30782088D+02
  90000.000 100000.0007 -2.0 -1.0  0.0  1.0  2.0  3.0  4.0  0.0         7291.572
  0.83917826D-07 -0.21239844D-07  0.77326109D-07  0.53491234D-07  0.22447412D-08
 -0.30744203D-13  0.12757806D-18                 0.78219386D+06  0.31197823D+02
N2               RossDaG (07/12/2021) (07/12/2021)
 7 tpis78 N    2.00    0.00    0.00    0.00    0.00 0   28.0134000          0.223
    200.000   1000.0007 -2.0 -1.0  0.0  1.0  2.0  3.0  4.0  0.0         8670.327
  0.43354807D+05 -0.67295718D+03  0.75331982D+01 -0.11906758D-01  0.17769178D-04
 -0.11797527D-07  0.29637498D-11                 0.21277987D+04 -0.18350394D+02
   1000.000   6000.0007 -2.0 -1.0  0.0  1.0  2.0  3.0  4.0  0.0         8670.327
  0.81834006D+06 -0.28999839D+04  0.67904381D+01 -0.99968394D-03  0.25448531D-06
 -0.33103139D-10  0.17454035D-14                 0.17065288D+05 -0.20389825D+02
   6000.000  20000.0007 -2.0 -1.0  0.0  1.0  2.0  3.0  4.0  0.0         8670.327
  0.18894564D+10 -0.13263191D+07  0.37792368D+03 -0.53408184D-01  0.40307069D-05
 -0.14880537D-09  0.21104853D-14                 0.10326528D+08 -0.31887164D+04
  20000.000  40000.0007 -2.0 -1.0  0.0  1.0  2.0  3.0  4.0  0.0         8670.327
 -0.10524631D+12  0.20847817D+08 -0.16698250D+04  0.71217357D-01 -0.17027992D-05
  0.21665798D-10 -0.11449289D-15                -0.18870719D+09  0.16354523D+05
  40000.000  60000.0007 -2.0 -1.0  0.0  1.0  2.0  3.0  4.0  0.0         8670.327
  0.19091069D+12 -0.21082329D+08  0.97164174D+03 -0.23494032D-01  0.31556530D-06
 -0.22183721D-11  0.63462067D-17                 0.20287827D+09 -0.99858829D+04
  60000.000  80000.0007 -2.0 -1.0  0.0  1.0  2.0  3.0  4.0  0.0         8670.327
  0.27025949D+11 -0.68938550D+06 -0.40544737D-06  0.42307758D-06  0.68146620D-08
 -0.11513635D-12  0.54520196D-18                 0.81078704D+07  0.34783316D+02
  80000.000 100000.0007 -2.0 -1.0  0.0  1.0  2.0  3.0  4.0  0.0         8670.327
 -0.30351651D-07  0.89964455D-07  0.86762851D-07  0.29363988D-07  0.21566383D-08
 -0.33168721D-13  0.14190225D-18                 0.20822130D+06  0.46367047D+02
N2+              RossDaG (07/12/2021) (07/12/2021)
 7 tpis89 N    2.00E- -1.00    0.00    0.00    0.00 0   28.0128514    1509508.442
    200.000   1000.0007 -2.0 -1.0  0.0  1.0  2.0  3.0  4.0  0.0         8671.118
  0.17456475D+06 -0.25885754D+04  0.18452385D+02 -0.43111638D-01  0.65063687D-04
 -0.47677990D-07  0.13668899D-10                 0.19281383D+06 -0.78025209D+02
   1000.000   6000.0007 -2.0 -1.0  0.0  1.0  2.0  3.0  4.0  0.0         8671.118
 -0.25607591D+07  0.60528383D+04 -0.14751844D+01  0.20661191D-02 -0.63049059D-07
 -0.42636051D-10  0.40039976D-14                 0.14025748D+06  0.41826699D+02
   6000.000  20000.0007 -2.0 -1.0  0.0  1.0  2.0  3.0  4.0  0.0         8671.118
 -0.76994905D+09  0.45575617D+06 -0.10018306D+03  0.12162181D-01 -0.72276371D-06
  0.21008007D-10 -0.23990583D-15                -0.34558443D+07  0.91292086D+03
  20000.000  40000.0007 -2.0 -1.0  0.0  1.0  2.0  3.0  4.0  0.0         8671.118
 -0.43290627D+10  0.83485882D+06 -0.53405391D+02  0.20008630D-02 -0.40634645D-07
  0.44253307D-12 -0.20088648D-17                -0.74401741D+07  0.57629097D+03
  40000.000  60000.0007 -2.0 -1.0  0.0  1.0  2.0  3.0  4.0  0.0         8671.118
 -0.28892736D+12  0.36410678D+08 -0.18950394D+04  0.52497613D-01 -0.81336653D-06
  0.66915087D-11 -0.22837346D-16                -0.34535896D+09  0.19370207D+05
  60000.000  80000.0007 -2.0 -1.0  0.0  1.0  2.0  3.0  4.0  0.0         8671.118
  0.24530951D+11 -0.63068586D+06 -0.52493160D-06  0.34683505D-06  0.64217363D-08
 -0.10837826D-12  0.51285774D-18                 0.75662951D+07  0.35128042D+02
  80000.000 100000.0007 -2.0 -1.0  0.0  1.0  2.0  3.0  4.0  0.0         8671.118
 -0.62123363D-07  0.19723219D-06  0.79075003D-07  0.11684558D-07  0.20788059D-08
 -0.31718411D-13  0.13495440D-18                 0.34428415D+06  0.45805766D+02
NO               RossDaG (07/12/2021) (07/12/2021)
 7 tpis89 N    1.00O   1.00    0.00    0.00    0.00 0   30.0061000      90766.374
    200.000   1000.0007 -2.0 -1.0  0.0  1.0  2.0  3.0  4.0  0.0         8674.174
  0.11920109D+05 -0.23257507D+03  0.52985098D+01 -0.70471429D-02  0.13755432D-04
 -0.10803889D-07  0.30979532D-11                 0.10913618D+05 -0.39469889D+01
   1000.000   6000.0007 -2.0 -1.0  0.0  1.0  2.0  3.0  4.0  0.0         8674.174
  0.23617072D+06 -0.13544017D+04  0.55095707D+01 -0.40616650D-03  0.10936544D-06
 -0.15299293D-10  0.96863430D-15                 0.17826561D+05 -0.90545404D+01
   6000.000  20000.0007 -2.0 -1.0  0.0  1.0  2.0  3.0  4.0  0.0         8674.174
 -0.70049593D+09  0.45670455D+06 -0.11264991D+03  0.14828641D-01 -0.94940035D-06
  0.29679473D-10 -0.36438119D-15                -0.35853913D+07  0.10103287D+04
  20000.000  40000.0007 -2.0 -1.0  0.0  1.0  2.0  3.0  4.0  0.0         8674.174
  0.18879362D+10 -0.43634569D+06  0.53457675D+02 -0.27674694D-02  0.78433356D-07
 -0.11323503D-11  0.66010858D-17                 0.38395671D+07 -0.46245159D+03
  40000.000  60000.0007 -2.0 -1.0  0.0  1.0  2.0  3.0  4.0  0.0         8674.174
 -0.33975972D+12  0.42544175D+08 -0.22025680D+04  0.60691652D-01 -0.93568343D-06
  0.76613284D-11 -0.26028209D-16                -0.40400199D+09  0.22517789D+05
  60000.000  80000.0007 -2.0 -1.0  0.0  1.0  2.0  3.0  4.0  0.0         8674.174
  0.24617196D+11 -0.63350468D+06 -0.39022529D-06  0.39287645D-06  0.64514036D-08
 -0.10890783D-12  0.51541428D-18                 0.74200831D+07  0.34984790D+02
  80000.000 100000.0007 -2.0 -1.0  0.0  1.0  2.0  3.0  4.0  0.0         8674.174
 -0.26828579D-07  0.96398641D-07  0.77483878D-07  0.28934604D-07  0.20835201D-08
 -0.31796832D-13  0.13529514D-18                 0.16635345D+06  0.45718860D+02
NO+              RossDaG (07/12/2021) (07/12/2021)
 7 g 5/99 N    1.00O   1.00E- -1.00    0.00    0.00 0   30.0055514     990809.877
    200.000   1000.0007 -2.0 -1.0  0.0  1.0  2.0  3.0  4.0  0.0         8670.277
```

```
  0.13158927D+05 -0.23537327D+03  0.50716798D+01 -0.50053014D-02  0.75439993D-05
 -0.41873081D-08  0.72817653D-12                  0.11920387D+06 -0.45899312D+01
   1000.000   6000.0007 -2.0 -1.0  0.0  1.0  2.0  3.0  4.0  0.0        8670.277
  0.14103726D+07 -0.46013036D+04  0.86678627D+01 -0.20239744D-02  0.54627322D-06
 -0.74198942D-10  0.40001764D-14                  0.14712215D+06 -0.33771262D+02
   6000.000  20000.0007 -2.0 -1.0  0.0  1.0  2.0  3.0  4.0  0.0        8670.277
  0.12277208D+10 -0.92540536D+06  0.28115717D+03 -0.41587093D-01  0.32684602D-05
 -0.12450870D-09  0.18093945D-14                  0.72629660D+07 -0.23480198D+04
  20000.000  40000.0007 -2.0 -1.0  0.0  1.0  2.0  3.0  4.0  0.0        8670.277
 -0.10854538D+12  0.21828957D+08 -0.17780012D+04  0.76953408D-01 -0.18635678D-05
  0.23970285D-10 -0.12784084D-15                 -0.19711208D+09  0.17382472D+05
  40000.000  60000.0007 -2.0 -1.0  0.0  1.0  2.0  3.0  4.0  0.0        8670.277
  0.30351048D+12 -0.34824160D+08  0.16654679D+04 -0.42095981D-01  0.59492157D-06
 -0.44466787D-11  0.13722475D-16                  0.33386231D+09 -0.17083460D+05
  60000.000  80000.0007 -2.0 -1.0  0.0  1.0  2.0  3.0  4.0  0.0        8670.277
  0.24857763D+11 -0.63436968D+06 -0.35434755D-06  0.41079917D-06  0.63966192D-08
 -0.10791656D-12  0.51069126D-18                  0.75840828D+07  0.35288470D+02
  80000.000 100000.0007 -2.0 -1.0  0.0  1.0  2.0  3.0  4.0  0.0        8670.277
 -0.21166355D-07  0.61093108D-07  0.82478011D-07  0.31330090D-07  0.20864775D-08
 -0.31906922D-13  0.13600032D-18                  0.31549602D+06  0.45963409D+02
O2               RossDaG (07/12/2021) (07/12/2021)
 7 tpis89 O   2.00    0.00    0.00    0.00    0.00 0   31.9988000          3.184
   200.000   1000.0007 -2.0 -1.0  0.0  1.0  2.0  3.0  4.0  0.0        8683.288
  0.33652552D+05 -0.48617507D+03  0.64314802D+01 -0.10039573D-01  0.19662999D-04
 -0.16582161D-07  0.51740111D-11                  0.12685709D+04 -0.10476010D+02
   1000.000   6000.0007 -2.0 -1.0  0.0  1.0  2.0  3.0  4.0  0.0        8683.288
 -0.15634034D+07  0.38784759D+04  0.90472502D-01  0.22237788D-02 -0.49089661D-06
  0.58687049D-10 -0.28799857D-14                 -0.26675963D+05  0.30453113D+02
   6000.000  20000.0007 -2.0 -1.0  0.0  1.0  2.0  3.0  4.0  0.0        8683.288
  0.55493713D+09 -0.32314527D+06  0.75594926D+02 -0.71554352D-02  0.35952376D-06
 -0.91487469D-11  0.93654717D-16                  0.25829451D+07 -0.62828534D+03
  20000.000  40000.0007 -2.0 -1.0  0.0  1.0  2.0  3.0  4.0  0.0        8683.288
  0.20489371D+10 -0.37771852D+06  0.36886233D+02 -0.16487772D-02  0.43697214D-07
 -0.60751598D-12  0.34670238D-17                  0.34292279D+07 -0.31193240D+03
  40000.000  60000.0007 -2.0 -1.0  0.0  1.0  2.0  3.0  4.0  0.0        8683.288
 -0.28852677D+12  0.36164821D+08 -0.18761391D+04  0.51823369D-01 -0.80069499D-06
  0.65696745D-11 -0.22363787D-16                 -0.34337050D+09  0.19182503D+05
  60000.000  80000.0007 -2.0 -1.0  0.0  1.0  2.0  3.0  4.0  0.0        8683.288
  0.21598087D+11 -0.55775561D+06 -0.42653476D-06  0.33753799D-06  0.58882504D-08
 -0.99168141D-13  0.46879735D-18                  0.65189479D+07  0.35774529D+02
  80000.000 100000.0007 -2.0 -1.0  0.0  1.0  2.0  3.0  4.0  0.0        8683.288
 -0.39940254D-07  0.13516547D-06  0.72581716D-07  0.18840769D-07  0.19889407D-08
 -0.30074135D-13  0.12718859D-18                  0.13488869D+06  0.45268435D+02
O2+              RossDaG (07/12/2021) (07/12/2021)
 7 tpis89 O   2.00E- -1.00    0.00    0.00    0.00 0   31.9982514    1171191.591
   200.000   1000.0007 -2.0 -1.0  0.0  1.0  2.0  3.0  4.0  0.0        8674.267
  0.63313641D+05 -0.97769736D+03  0.94989065D+01 -0.18852874D-01  0.31282130D-04
 -0.23892628D-07  0.69612598D-11                  0.14441827D+06 -0.27134458D+02
   1000.000   6000.0007 -2.0 -1.0  0.0  1.0  2.0  3.0  4.0  0.0        8674.267
 -0.88513885D+06  0.18931529D+04  0.18856183D+01  0.15808495D-02 -0.45083865D-06
  0.61754426D-10 -0.29875162D-14                  0.12701702D+06  0.17041926D+02
   6000.000  20000.0007 -2.0 -1.0  0.0  1.0  2.0  3.0  4.0  0.0        8674.267
 -0.55309324D+09  0.45347036D+06 -0.13552951D+03  0.20614746D-01 -0.14938783D-05
  0.51891386D-10 -0.69751503D-15                 -0.33369065D+07  0.11846197D+04
  20000.000  40000.0007 -2.0 -1.0  0.0  1.0  2.0  3.0  4.0  0.0        8674.267
  0.24471514D+11 -0.50405639D+07  0.44237210D+03 -0.20247568D-01  0.51753098D-06
 -0.69655604D-11  0.38589465D-16                  0.45458268D+08 -0.42395706D+04
  40000.000  60000.0007 -2.0 -1.0  0.0  1.0  2.0  3.0  4.0  0.0        8674.267
 -0.50803948D+12  0.62783398D+08 -0.32135847D+04  0.87501942D-01 -0.13337749D-05
  0.10799840D-10 -0.36293174D-16                 -0.59686333D+09  0.32870451D+05
  60000.000  80000.0007 -2.0 -1.0  0.0  1.0  2.0  3.0  4.0  0.0        8674.267
  0.23266799D+11 -0.60098153D+06 -0.42682656D-06  0.35404895D-06  0.61948780D-08
 -0.10439104D-12  0.49344733D-18                  0.71716551D+07  0.35723772D+02
  80000.000 100000.0007 -2.0 -1.0  0.0  1.0  2.0  3.0  4.0  0.0        8674.267
 -0.38443113D-07  0.13437255D-06  0.72997114D-07  0.21466713D-07  0.20228230D-08
 -0.30692995D-13  0.13010475D-18                  0.29241690D+06  0.45938327D+02
```

B.5 Thermodynamic Properties Plots

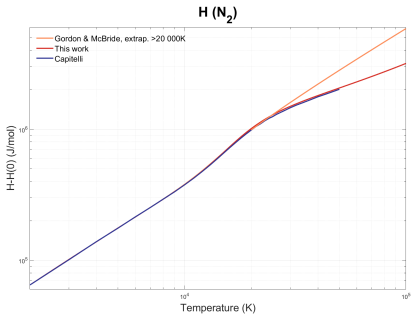

(a) Enthalpy of N_2

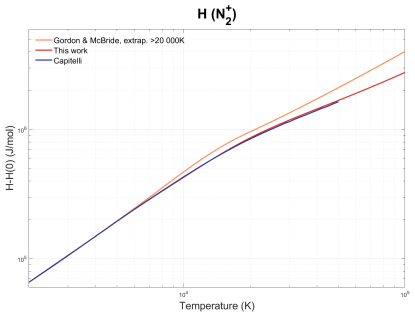

(b) Enthalpy of N_2^+

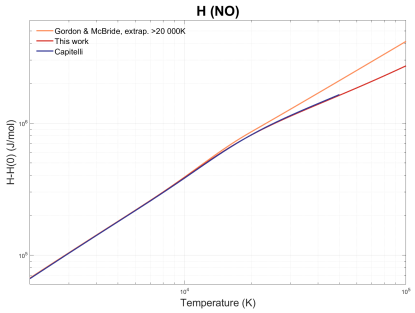

(c) Enthalpy of NO

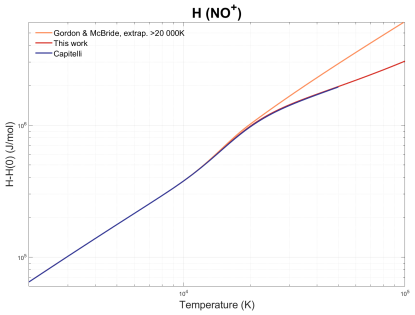

(d) Enthalpy of NO^+

Figure B.5: Enthalpy vs Temperature graphs for N_2, N_2^+, NO and NO^+.

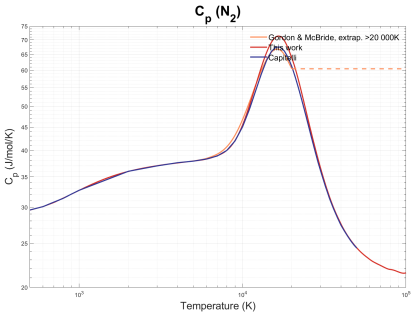

(a) Specific heat of N_2

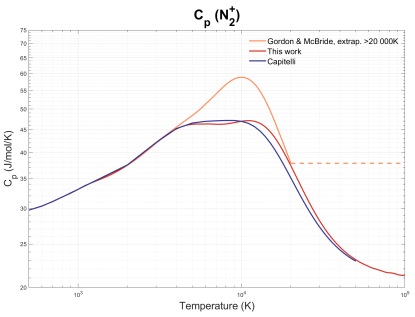

(b) Specific heat of N_2^+

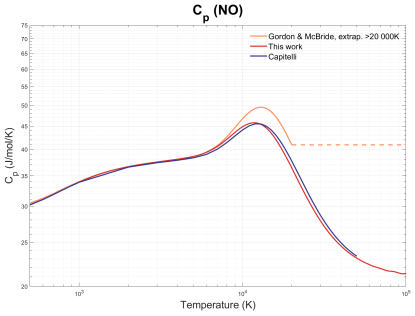

(c) Specific heat of NO

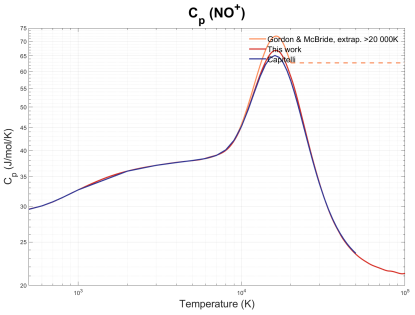

(d) Specific heat of NO^+

Figure B.6: C_p vs Temperature graphs for N_2, N_2^+, NO and NO^+.

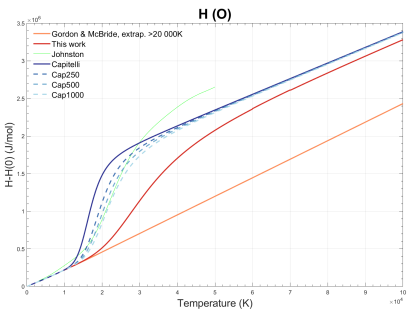

(a) Enthalpy of O

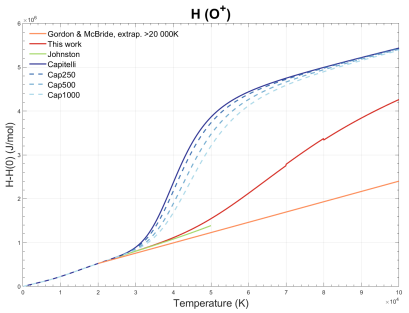

(b) Enthalpy of O^+

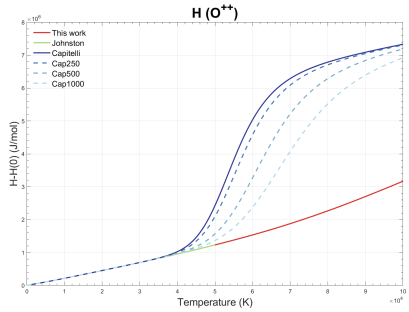

(c) Enthalpy of O^{++}

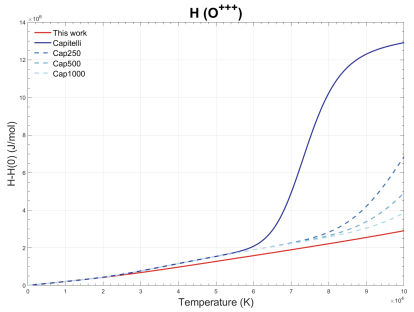

(d) Enthalpy of O^{+++}

Figure B.7: Enthalpy vs Temperature graphs for O, O^+, O^{++} and O^{+++}.

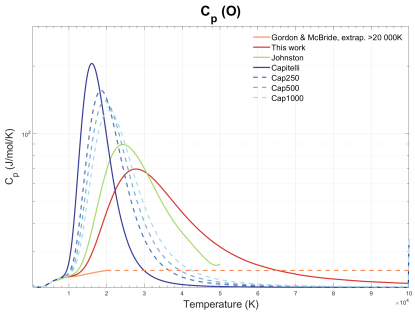

(a) Specific heat of O

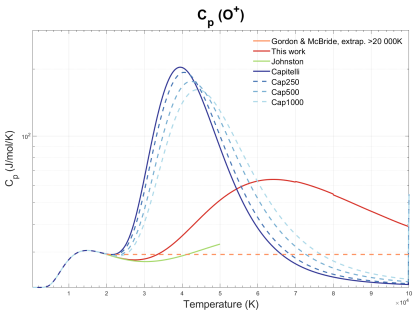

(b) Specific heat of O^+

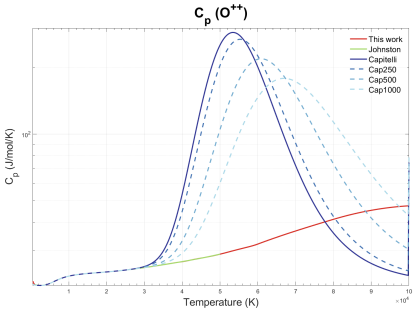

(c) Specific heat of O^{++}

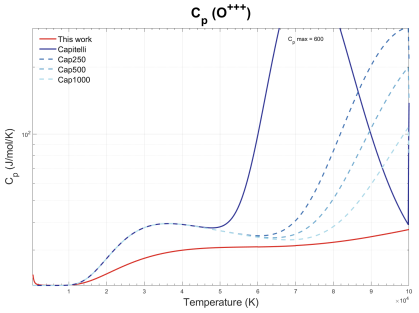

(d) Specific heat of O^{+++}

Figure B.8: C_p vs Temperature graphs for O, O^+, O^{++} and O^{+++}.

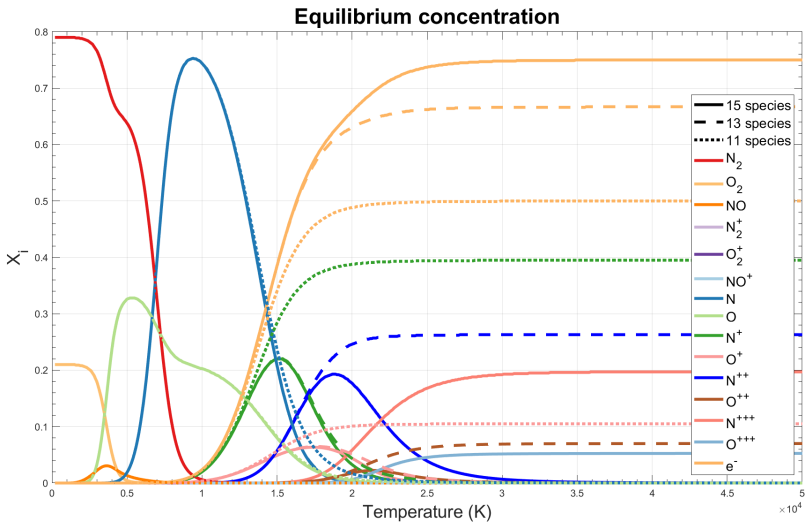

Figure B.9: Equilibrium composition of Earth atmosphere mixture with x_{N_2} = 0.79 and x_{O_2} = 0.21, considering 11, 13 and 15 species.

B.6 Chemical Kinetics

Table B.20: Chemical kinetics for neutral and ionized species.

Ref.	Reaction	A	n	$\theta_R(K)$	Third body, M
R1	$N_2 + M_1 \rightleftharpoons N + N + M_1$	3.01×10^{16}	-1.60	113 200	[80]
R2	$N_2 + e^- \rightleftharpoons N + N + e^-$	6.00×10^{-3}	2.60	113 200	[119]
R3	$N_2 + M \rightleftharpoons N + N + M$	7.00×10^{15}	-1.60	113 200	[80]
R4	$N_2 + O \rightleftharpoons NO + N$	6.00×10^{7}	0.10	38 000	[120]
R5	$NO + M_2 \rightleftharpoons N + O + M_2$	4.40×10^{10}	0.00	75 500	[121]
R6	$NO + M_3 \rightleftharpoons N + O + M_3$	2.00×10^{9}	0.00	75 500	[121]
R7	$O_2 + M_1 \rightleftharpoons O + O + M_1$	1.00×10^{16}	-1.50	59 360	[80]
R8	$O_2 + M \rightleftharpoons O + O + M$	2.00×10^{15}	-1.50	59 360	[80]
R9	$O_2 + N \rightleftharpoons NO + O$	2.49×10^{3}	1.18	4010	[122]
R10	$N + N \rightleftharpoons N_2^+ + e^-$	4.40×10^{1}	1.50	67 500	[82]
R11	$N + O \rightleftharpoons NO^+ + e^-$	5.30×10^{6}	0.0	31 900	[82]
R12	$N + e^- \rightleftharpoons N^+ + e^- + e^-$	3.12×10^{8}	0.358	170 376	[82]
R13	$N^+ + N_2 \rightleftharpoons N_2^+ + N$	1.00×10^{6}	0.50	12 200	[80]
R14	$O^+ + N_2 \rightleftharpoons N_2^+ + O$	9.10×10^{5}	0.36	22 800	[80]
R15	$NO + O^+ \rightleftharpoons N^+ + O_2$	1.40×10^{-1}	1.90	26 600	[80]
R16	$NO^+ + N \rightleftharpoons N_2^+ + O$	7.20×10^{7}	0.00	35 500	[80]
R17	$NO^+ + N \rightleftharpoons O^+ + N_2$	3.40×10^{7}	-1.08	12 800	[80]
R18	$NO^+ + O \rightleftharpoons N^+ + O_2$	1.00×10^{6}	0.50	77 200	[80]
R19	$NO^+ + O \rightleftharpoons O_2^+ + N$	7.20×10^{6}	0.29	48 600	[80]
R20	$NO^+ + O_2 \rightleftharpoons O_2^+ + NO$	2.40×10^{7}	0.41	32 600	[80]
R21	$O + O \rightleftharpoons O_2^+ + e^-$	7.10×10^{-4}	2.70	80 600	[81]
R22	$O + e^- \rightleftharpoons O^+ + e^- + e^-$	5.27×10^{8}	0.274	156 871	[81]
R23	$O_2^+ + N \rightleftharpoons N^+ + O_2$	8.70×10^{7}	0.14	28 600	[80]
R24	$O_2^+ + N_2 \rightleftharpoons N_2^+ + O_2$	9.90×10^{6}	0.00	40 700	[80]
R26	$O_2^+ + O \rightleftharpoons O^+ + O_2$	4.00×10^{6}	-0.09	18 000	[81]
R27	$O_2 + e^- \rightleftharpoons O_2^+ + e^- + e^-$	2.19×10^{4}	1.16	130 000	[123]

where:

- M = N_2, O_2, NO, N_2^+, O_2^+, NO^+, N^+, O^+;
- M_1 = N, O;
- M_2 = N, O, NO;
- M_3 = N_2, O_2, N_2^+, O_2^+, N^+, O^+, NO^+